Max-Planck-Institut für Metallforschung
Stuttgart

Behaviour of Glasses and Polymer-derived Amorphous Ceramics under Contact Stress

Zaklina Burghard

Dissertation
an der
Universität Stuttgart

Bericht Nr. 154
Juni 2004

Behaviour of glasses and polymer-derived amorphous ceramics under contact stress

Dissertation

Von der Fakultät Chemie der Universität Stuttgart
Zur Erlangung der Würde eines
Doktors der Naturwissenschaften (Dr. rer. nat)
Genehmigte Abhandlung

Vorgelegt von
Zaklina Burghard
Aus Belgrad

Hauptberichter: Prof. Dr. rer. nat. Fritz Aldinger
Mitberichter: Prof. Dr. rer. nat. Dr. hc. mult. Günter Petzow

Tag der mündlichen Prüfung: 4. Mai 2004

Institut für Nichtmetallische Anorganische Materialien der Universität Stuttgart
Max-Planck Institut für Metallforschung, Stuttgart
Pulvermetallurgisches Laboratorium
2004

Dedicated to my parents

Acknowlegments

It is a pleasure for me to express my thanks to Prof. Dr. Fritz Aldinger for providing me the possibility to carry out my thesis work in his department, as well as for his steady guidance throughout the past three years.

I would like to thank Prof. Dr. G. Petzow for his support and accepting to become the "Mitberichter" for my thesis. I am also grateful to Prof. Dr. E.J. Mittemeijer for his interest in my work and accepting to examine my thesis.

Many thanks to Prof. Dr. M. Rühle for his friendly encouragements and including me in the Graduiertenkolleg "Innere Grenzflächen", which gave me the opportunity to widen my knowledge in the field of material science.

I am very grateful to Prof. Dr. B Lawn, (National Institute of Standards and Technology, Gaithersburg, USA) who gave me many important hints that deepened my understanding of fracture mechanics, and the numerous discussions that helped me to focus on the central goal of my thesis.

Furthermore, I would like to thank Prof. Dr. J. Rödel (Institut für Materialwissenschaft, Technische Universität Darmstadt) and Dr. T. Fett (Institut für Materialforschung, Forschungszentrum Karlsruhe) for stimulating discussions about my experimental results.

I am thankful to Dr. A. Zimmermann for the supervision of my work.

I highly appreciate the continuous support of Dr. G. Rixecker, and his thorough reading of the thesis manuscript.

For the careful preparation of many samples and further experimental support, I would like to thank Mr. R. Mager.

My rich thanks to Ms. U. Täffner for her friendly introduction to the atomic force microscope, and her effective help in case something did not work easily.

Further thanks to my colleague Nana (Mr. N. Janakiraman) for giving me the privilege to examine his highly valuable samples, as well as for the fruitful collaboration.

I am indebted to Dr. U. Wegst, who arranged for the sample preparation by ion beam thinning, and Ms. B. Heiland for managing this rather difficult task.

I would like to thank Mr. H. Kammerlander and his co-workers from the glass technique for high-quality cutting of many samples.

Moreover, I received friendly support for scanning electron microscope investigation by Mr. H. Labitzke and Ms. S. Kuchemann, and for transmission electron microscopy by Dr. N. Bunjes.

The preparation of my thesis would not have been possible without the good working atmosphere and the warm welcome of the following persons: Ms. Paulsen, Ms. Garcia, Ms. Weber-Bock, Ms.Schäfer, Mr.Hammound, Mr.Bruckner, Mr.Schweitzer, Mr.Dahmen, and all other people from PML. Many thanks to my roommates Steffi and Stefanie and other colleagues Marija, Branko, Reinhold, Arnt …

Finally, I express my thanks to my family, especially my parents and my sister, for their support, and my husband who kept me holding on by continuous encouragement and to my daughter who gave me warm smile in each difficult moment.

Contents

1. Symbols and abbreviations

A, A_0	amplitude damping constant
a	indent half diagonal
B	thickness
b	radius of the plastic zone
c, c_1	crack length, inner crack tip
d	distance between two indentations
E, E'	Young's modulus, Young's modulus for plane strain
F	dimensionless crack shape factor
f_{ij}	angular function
H	hardness
h	Green's weight function.
K, K_0, K_A	stress intensity factor, stress intensity threshold, applied stress intensity
K_C	fracture toughness or critical stress intensity factor
n ,v_0	the sub-critical crack growth parameters
P	applied load on indenter
R	radial distance from the point of contact
R,R',C,C'	normalized coordinates
r	radial coordinate
r',c'	integration variables
r_i ,r_{i+1}	radial distance interval
T	temperature
t	time
U	normalized crack opening
u	half crack opening;
V,ΔV	volume of the plastic zone, indentation volume
v	crack velocity
x	crack tip coordinate
W	width
α	material dependent parameter
β	relative plastic zone dimension
δ	dimensionless constant
ϕ	indenter half-angle

ν	Poisson' s ratio
ρ	density
χ	calibration parameter
σ_{11}, σ_{22}, σ_{33}	principal normal stresses
σ_i,	residual stress acting in the interval i
σ_R, $\sigma(r)$	maximum residual stress, stress distribution
ξ	dimensionless constant that depends on the type of deformation
ψ	geometrical dependent parameter
AFM	atomic force microscopy
COD	crack opening displacement
CT	compact tension
DCB	double cantilever beam
FEM	finite element method
FIB	focused ion beam
HRSEM	high resolution scanning electron microscopy
ICL	indentation crack length
LEM	Lawn, Evans,Marshal model
OM	optical microscopy
SENB	single edge notched beam
SCCG	subcritical crack growth
WOL	wedge opening load

2. Zusammenfassung und Ausblick

In der vorliegenden Arbeit wurden detaillierte Studien an Vickers-Eindrücken mit dem Ziel durchgeführt, die Methode des Rissöffnungsprofils zur Bestimmung der Bruchzähigkeit und des Restspannungsfeldes zu etablieren. Hierfür wurden neben amorphen SiCN-Keramiken, welche aus Polymervorstufen bei vier unterschiedlichen Pyrolyse-Temperaturen erhalten wurden, zwei Arten von Gläsern als Vergleichsmaterialien untersucht. Als Gläser wurden Kalknatron- und Borosilikat-Glas gewählt, da deren "normales" bzw. "anormales" Verhalten unter Kontaktspannungen gut dokumentiert ist. Ihre besondere Eignung als Referenzmaterialien erklärt sich aus dem Vorliegen umfangreicher Ergebnisse zu Eindruck-Experimenten. Während Eindruckversuche an spröden Materialien wie Siliziumnitrid, Aluminiumoxid und Siliziumcarbid schon durchgeführt wurden, sind keine entsprechenden Daten für polymer-basierte amorphe Keramiken verfügbar. Da sich die letztgenannten Materialien jedoch in ihrer Entwicklungsphase befinden, wird eine insbesondere für kleinere Proben geeignete Methode zur Bestimmung der Bruchzähigkeit dringend benötigt.

Für Messungen des Rissöffnungsprofils sind generell Methoden mit hoher Ortsauflösung, wie z.B. Rasterkraft- oder Rasterelektronenmikroskopie, erforderlich. Im Rahmen der vorliegenden Arbeit hat sich die Rasterkraftmikroskopie als insgesamt am geeignetsten erwiesen. Dies geht insbesondere darauf zurück, dass sie eine sehr genaue Bestimmung der Position der Rissflanken gestattet. Die Rasterkraftmikroskopie besitzt zusätzlich den Vorteil, dass die Probe nicht verändert wird, im Gegensatz zur Rasterelektronenmikroskopie, bei welcher es zu einer Ablagerung von amorphem Kohlenstoff auf der Probenoberfläche und somit zu einer Verengung des Risses kommt. Ferner setzt der Einsatz der Rasterkraftmikroskopie keine Beschichtung der Probe mit einem dünnen, leitfähigen Metallfilm voraus, welche bei der Rasterelektronenmikroskopie erforderlich ist. Allerdings ist die Rasterkraftmikroskopie vergleichsweise zeitaufwendig, wodurch es zu einem nennenswerten Risswachstum während der Messungen unter Umgebungsbedingungen kommen kann. Dieses Problem könnte zwar prinzipiell durch Arbeiten in einer Vakuumkammer behoben werden, allerdings sind solche Mikroskope nur schwer zugänglich.

Die Untersuchung der in Kalknatron- und Borosilikatglas mittels mechanischem Eindruck erzeugten Rissstrukturen bestätigte die Ergebnisse einer früheren Studie [79Aro], denen zufolge das letztere Glas anormales Verhalten zeigt. Für die hier untersuchten amorphen

Keramiken wurde ebenfalls anormales Verhalten gefunden, welches sich in einer kurzen Risslänge, einer geringen Ausdehnung der Eindrücke sowie in der Bildung von Kegelrissen widerspiegelt. Daraus ist ersichtlich, dass es in diesen Materialien zur Materialverdichtung aufgrund einer Komprimierung der "offenen" Mikrostruktur (oder des "freien Volumens") unter den Eindruckbedingungen kommt. Unter Verwendung des Kegelriss-Öffnungswinkels als Maß für die Anomalie des Verhaltens unter dem Eindruck erwiesen sich die amorphen Keramiken als stärker anormal als Borosilikatglass, jedoch weniger anormal als Quarzglas. Darüber hinaus trat hervor, dass sich das Verhalten der amorphen Keramiken sich mit steigender Pyrolysetemperatur demjenigen von Borosilikatglas annähert, wie aus dem ansteigenden Öffnungswinkel hervorgeht. Als Folge des anormalen Verhaltens der amorphen Keramiken kann die Risslänge (Indentation Crack Length- oder ICL-Methode) nicht zur Bestimmung der Bruchzähigkeit herangezogen werden, da die benötigten Kalibrationsparameter ausschließlich für Materialien mit normalen Verhalten in der Literatur zu finden sind. Diese Beschränkung machte es erforderlich, eine neue Methode zur Bestimmung der Bruchzähigkeit - auf der Basis des Rissöffnungsprofils - auszuarbeiten. Eine solche Notwendigkeit besteht auch für andere polymer-basierte Keramiken.

Die Rissöffnungsprofile von radialen Eindruckrissen in den untersuchten Materialien zeigten die charakteristischen Unterschiede zwischen normalem und anormalem Verhalten auf. Letzteres ist gekennzeichnet von einer geringeren Rissöffnung, da die Verdichtung einen Teil der durch den Eindruck erzeugten Spannung abbauen kann, wodurch die Rissöffnungskräfte reduziert werden. Mittels einer normierten Auftragung konnten die Unterschiede zwischen normalem und anormalem Verhalten noch stärker hervorgehoben werden. Der Vergleich zwischen den amorphen Keramiken und den beiden Glasarten ergab, dass erstere die geringste normierte Rissbreite und die kürzeste normierte Risslänge aufweisen. Aus dieser Beobachtung geht hervor, dass die amorphen Keramiken ein stärker anormales Verhalten als das Borosilikatglas aufweisen. Der direkte Vergleich ergab außerdem ein deutlich größere Steigung des Profilverlaufs im Fall des anormalen Verhaltens. Ferner wurde für die amorphen Keramiken abnehmend anormales Verhalten mit steigender Pyrolyse-Temperatur gefunden.

Messungen des gesamten Rissöffnungsprofils gestatteten es, die Art und Stärke der relevanten Rissöffnungskräfte (Restspannungsfelder) zu bestimmen. Hierfür wurde ein numerisches Verfahren basierend auf der Methode der Gewichtsfunktionen entwickelt. Außerdem wurde das Expanding-Cavity-Modell (Hills Modell) verwendet, um die maximale Restspannung zu

bestimmen. Im Fall der Gläser wurde ein deutlich höhere Spannung bei anormalem gegenüber normalem Verhalten gefunden (σ_R = 1,04 GPa für Kalknatron- und σ_R = 0,49 GPa für Borosilikatglas). Diese Werte befinden sich in guter Übereinstimmung mit früheren Untersuchungen mittels polarisiertem Licht [79Aro]. Für die amorphem Keramiken wurden vergleichbare maximale Restspannungen wie in Borosilikatglas erhalten. Die Keramiken weisen zudem einen Anstieg in der maximalen Restspannung von 0.5 auf 0.8 GPa mit steigender Pyrolyse-Temperatur auf, in Übereinstimmung mit dem in der selben Richtung zunehmend normalen Verhalten.

Die erhaltenen Werte für den Spannungsintensitätsfaktor der Gläser (0,51 MPa $m^{1/2}$ für Kalknatron- und 0,56 MPa $m^{1/2}$ für Borosilikatglas) stimmen gut mit Literaturwerten überein. Für die amorphen Keramiken wurden größere Werte als für die Gläser gefunden. Es wurde ferner ein genereller Anstieg des Spannungsintensitätsfaktors mit steigender Pyrolyse-Temperatur beobachtet (mit einem Maximum für SiCN-1000°C). Es ist festzuhalten, dass das verwendete Verfahren zur Auswertung des gesamten Rissöffnungsprofils eine ausreichend genaue Bestimmung des Restspannungsfeldes und des Spannungsintensitätsfaktors in den amorphem Keramiken gestattet, und es somit erlaubt, eine erste Einschätzung hinsichtlich ihres Eindruckverhaltens (normal oder anormal) zu erhalten.

Um die Verlässlichkeit der mittels des entwickelten numerischen Verfahrens berechneten Restspannungen und Spannungsintensitätsfaktoren zu testen, wurde ein neuartige Methode verwendet, welche auf dem sogenannten Geometrieparameter beruht. Dieser Parameter sollte eine Konstante für unterschiedliche Materialien sein. Obwohl eine geringe Abweichung vom Öffnungswinkel der verwendeten Vickers-Pyramide beobachtet wurde, geht aus der guten Übereinstimmung zwischen den berechneten Werten für die Eindruckwinkel und Geometrieparameter der unterschiedlichen Materialien hervor, dass das Verfahren verlässliche Ergebnisse liefert. In Anbetracht der grundsätzlichen Schwierigkeiten einer genauen Bestimmung von Restspannungen gestattet die hier verwendete Methode eine beachtlich gute Abschätzung dieses wichtigen Materialparameters.

Die maximale Restspannung und der Spannungsintensitätsfaktor, bestimmt aus dem gesamten Rissöffnungsprofil, ermöglichten ferner eine Abschätzung des Restspannungsparameters χ. Dieser Parameter ist für neue Materialien von Wichtigkeit, da von diesen oftmals nur kleine Proben hergestellt werden können, welche den Einsatz konventioneller

Bestimmungsmethoden nicht gestatten. Mit Hilfe des auf diesem Wege bestimmten Parameters χ wird es möglich, die ICL-Methode zur Bestimmung der Bruchzähigkeit für unterschiedliche Materialien zu verwenden.

Die Messung des Rissöffnungsprofils in der Nähe des Rissendes eröffnet einen alternativen Zugang zur Bestimmung der Bruchzähigkeit, wobei von dem angenähert parabolischen Verlauf der Rissflanken in Nähe der Rissspitze Nutzen gezogen wird. Die Bruchzähigkeit kann durch Anpassen eines parabolischen Verlaufs an das Rissöffnungsprofil im Bereich der Rissspitze gewonnen werden. Hierzu wurde eine geeignete, universelle Anpassungsfunktion bestimmt, welche die für anormale Materialien charakteristischen Abweichungen von dem ideal parabolischen Verlauf berücksichtigt. Nahezu identische Bruchzähigkeit wurde für die zwei Gläser gefunden, in Übereinstimmung mit Ergebnissen der DCB ("Double Cantilever Beam") Methode. Die Bruchzähigkeit der amorphen Keramiken ist größer als die der Gläser und zeigt einen Anstieg mit der Pyrolyse-Temperatur bis 1000°C, während die bei 1100°C synthetisierte Keramik eine geringe Bruchzähigkeit aufweist. Somit tritt eine gute Übereinstimmung zwischen der Auswertung des gesamten und des Rissspitzennahen Öffnungsprofils zutage.

Der Einfluss unterkritischen Risswachstums auf das Rissöffnungsprofil, der bei den amorphen Keramiken nicht auftritt, wurde für die Gläser eingehend untersucht. Hierfür wurde das gesamte Öffnungsprofil nach drei unterschiedlichen Zeitspannen (30 min, 2 Tage, 10 Tage) jeweils mittels Rasterelektronenmikroskopie bestimmt. Dabei wurde festgestellt, dass der Großteil der Änderungen in der Rissöffnung innerhalb von 2 Tagen erfolgt. Zur Bestimmung des Einflusses des Risswachstums auf die Bruchzähigkeit und die maximale Restspannung wurde sowohl Berechnungen anhand des gesamten Rissöffnungsprofils als auch Anpassungen des Profils nahe der Rissspitze durchgeführt. Dabei ergab sich, dass die Bruchzähigkeit mit zunehmender Risslänge ansteigt, während die Restspannung nahezu unverändert bleibt.

Aus der vorliegenden Arbeit geht hervor, dass die Auswertung des Rissöffnungsprofils eine zuverlässigere Methode zur Bestimmung der Bruchzähigkeit darstellt als die Messung der Risslänge (ICL-Verfahren). Allerdings setzt die erst genannte Methode mikroskopische Untersuchungen mit hoher Ortsauflösung voraus, wodurch sich ein höherer Messaufwand ergibt. Wenn dieser Aufwand getragen werden kann, sollte die hier beschriebene Methode es

gestatten, die Deformationsantwort einer breiten Vielfalt spröder Materialien (Gläser, etc.) zu bestimmen.

3. Abstract

A Vickers indentation study is presented focusing on the crack opening displacement (COD) method as one new approach for fracture toughness determination. COD measurements over the entire radial indentation crack lengths enable quantitative evaluations of residual stresses at the contact site. An alternative estimation of toughness, without knowledge of the calibration parameter which is required for the indentation crack length (ICL) method, is provided by COD measurements in the vicinity of the crack tip. In addition, this method allows to study slow crack growth which is another important phenomenon. The measurements generally require recourse to high magnification, high accuracy observation techniques like atomic force microscopy (AFM) that has been used in this work.

Two different types of glasses, as reference materials, and fully dense, amorphous SiCN ceramics produced from precursor polymers through a casting route are investigated. Soda lime and borosilicate glass have been selected, which are well documented to behave as "normal" and "anomalous" glass under contact stress, respectively. A set of four different pyrolysis temperatures for polymer-derived ceramics differing in pyrolysis temperature (800°C, 900°C, 1000°C, 1100°C), were chosen.

Indents for a given load in the investigated materials reveal substantially shorter radial cracks and smaller opening in polymer derived SiCN ceramics. This effect is attributed to the different levels of residual elastic–plastic contact stresses that drive the radial crack formation. In soda-lime glass, the plastic component of contact deformation is shear-driven, with conservation of material volume; in borosilicate, as well as polymer-derived amorphous SiCN ceramics, the plastic component is compression-driven, with resultant material densification. The latter deformation mode is less effective in expanding the surrounding elastic material outward upon removal of the indenter. Hence, the opening and crack lengths are consequently smaller in the amorphous SiCN ceramics which is in agreement with the calculated lowest residual stress level in these materials. A higher toughness in polymer derived amorphous SiCN ceramics relative to the glasses is obtained, and an increase with increasing pyrolysis temperature. The influence of subcritical crack growth on the crack opening profiles was investigated only in case of the glasses since the polymer-derived amorphous SiCN ceramics did not show subcritical crack length growth.

The methodology presented in this study should prove useful as a means of characterizing the deformation response of glasses and other brittle materials under contact stress.

4. Introduction

The fracture toughness or critical stress intensity factor, K_C , is a measure of the resistance of a material to failure from fracture [98Cra]. Therefore it is an important parameter required for the prediction of the mechanical performance of structural materials.

The advent of modern high technology has led to an increased demand for strong materials. In an increasing number of engineering applications, severe service conditions such as high temperatures and hostile environments have necessitated a trend toward materials with intrinsically strong, covalent/ionic bonding. However, as structural components these materials suffer from one major disadvantage; they tend to be brittle. Consequently, the improvement of fracture toughness, especially of high-quality ceramics, remains one of the most important goals in materials development. An associated problem is the accurate measurement or estimation of fracture toughness in such brittle or semi-brittle materials, particularly in small samples.

A large variety of experimental methods have been developed for fracture toughness determination [93Sak], including the single edge notched beam (SENB), compact tension (CT) or wedge opening load (WOL) and double cantilever beam (DCB) method. These methods, however, usually require a minimum number of samples of sufficiently large dimensions, which limits their application range especially with respect to the development of new materials.

As an alternative, indentation methods have recently emerged as a powerful tool for evaluating and characterizing the deformation and fracture properties of brittle glasses and ceramic materials, particularly as quantified by hardness and toughness. These methods fall into two main categories:

- tests in which K_C is evaluated from direct measurement of crack length as a function of indentation load [75Lawa, 84Bin, 87Ost];
- tests where the indentation crack serves as a controlled flaw in a flexural specimen so that K_C is determined by strength measurement [79Mara, 81Cha, 92Bra].

In the study of fracture properties of ceramic materials, direct length measurement of cracks produced by the standard Vickers diamond pyramid is most widely used. Apart from its simplicity, this approach offers the following important advantages:

- many tests can be performed on the same small sample, making this technique an economic, powerful tool for the characterization and optimization of materials. In

addition, the localization of the fracture enables toughness determination to be performed on small areas with dimensions on the micrometer scale, such as individual grains or grain boundaries. It thus allows to access the basic fracture information, which has not previously been amenable to experimental determination in porous materials [98Nis, 01Bau, 03Tan], or thin films [03Zhea];

- it has also proved useful for investigating residual surface stresses [94Zen,95Zen] or characterising subcritical crack growth [99Gre, 81Wie, 01Koc] associated with fatigue of ceramic materials [81Lawb, 99Sgl, 99Sglb,01Sgl];
- it allows to study crack initiation as well as propagation (thereby enabling the determination of the 'brittleness' of a material [76Law, 97Qui]);
- the test samples are easy to prepare - only polishing is required;
- it simulates individual events in the impact process yielding very useful information about the micromechanism, relevant for erosion and wear resistance [77Swa]);
- the fracture initiating crack can be considered as a model for natural defects.

Despite these advantages, a critical factor in any toughness determination by measuring the indentation crack length is that no general formula is available that could be applied to all possible types of crack profiles, and which is valid over a large range of loads for all ceramic materials [89Pon]. The main problem is to properly account for the residual contact stresses that play a primary role in driving the cracks at all stages of growth, both during and after the indentation cycle. The existing models are insufficient in this respect, since the required residual stress field term is not directly available. This obstacle has been overcome for materials of known fracture toughness by using an appropriate calibration process. The latter requires that the plastic component of deformation is a constant volume, radial displacement process, characterised by a well-defined yield stress. However, this is not fulfilled for all materials. As a consequence, unacceptable error levels arise in the toughness estimation when this method is used for materials that show differing indentation behaviour. In light of these problems a new approach for fracture toughness determination by indentation is needed, which minimizes the dependence on the residual stress parameter, and is therefore applicable to a wide range of materials.

Recently, a new promising approach for examining the intrinsic toughness properties by measuring the crack opening displacement (COD) of indentation cracks has been proposed [90Röd, 97Sei]. The major advantage of this approach is that it can be applied to materials showing any type of indentation behaviour, without requiring calibration parameters. In

addition, COD measurements performed over the entire indentation crack length enable quantitative evaluations of residual stresses at the contact site.

However, the development of this approach is currently in its infancy. In particular, its applicability to different materials has still to be explored, which includes the comparison of the achievable accuracy with that of other methods. This requires an appropriate measuring technique as well as a means to quantitatively evaluate the COD data.

Towards this end, the present thesis investigates the COD in two different types of material, namely glasses and polymer derived amorphous ceramics. This comparative study aims to determine whether this approach is able to reliably yield the fracture toughness in both materials. On the one hand glasses were chosen as a suitable reference due to the large number of indentation studies that have been performed on this material. On the other hand, although indentation techniques (apart from glasses) have been applied to brittle materials such as silicon nitride, alumina and silicon carbide, no detailed investigations are reported for polymer derived amorphous ceramics. Since the latter material class is still under development, a reliable method for fracture toughness determination would be very helpful for optimising its mechanical properties. Especially for the examination of the near tip crack region, a microscopic technique of high resolution is principally required. To achieve this, atomic force microscopy (AFM) was employed for the first time to investigate indentation crack profiles.

5. Principles of indentation technique – Literature survey

5.1. Contact stress fields – Sharp and blunt indentation

In indentation fracture, the contact stress field within which the cracks develop is of central importance. The contact stress field evolving beneath the indenter is principally determined by geometrical factors (indenter shape) and material properties (elastic modulus, hardness, toughness). The indentation shape can be classified as either 'blunt' or 'sharp' [75Lawa], depending on whether there exists irreversible deformation at the contact. Contacts which are elastic in nature up to the point of fracture, *e.g.* those usually formed by a spherical indenter, may be considered as 'blunt'. By contrast, contacts which are essentially plastic–like those produced by pyramid or cone indenters (Vickers or Knoop diamonds) – are said to be 'sharp'. In this context, the term plastic describes any irreversible deformation process. Due to the presence of an elastic matrix around the plastically deformed region, this type of contact is often called elastic-plastic. In some cases, however, the spherical indenter can behave more like a sharp indenter, especially at high applied loads [77Wie, 77Eva], or when the radius of sphere is less than critical [76Swaa]. On the other hand, if densification occurs during indentation, the indenter gets somewhat "blunted" [79Aro, 82Isi, 95Kur] and thus behaves like a blunt indenter.

Although both blunt and sharp indenter crack patterns can be used to determine fracture toughness [76Evaa], sharp indenters are more suitable for this purpose. This holds especially in opaque materials which produce surface cracks with radial morphology. In addition, sharp indents are more close to real contact situations, where the extent of surface damage is a prime concern. Further, as crack formation with sharp indenters typically occurs at loads a few orders of magnitude less than for blunt indenters [77Law], the former allows the use of a smaller testing machine. Finally, a major advantage of sharp indenters is the constant geometry of the residual impression, *i.e.* the indentation does not change shape as the indenter penetrates in a specimen. The contact pressure is thus independent of indent size and affords a convenient measure of the hardness [51Tab]. The most commonly used sharp indenter is the Vickers indenter [83Mar].

5.1.1. Elastic stress field

In the simplest configuration, the contact stress field is represented by an isotropic, linear, elastic half-space subjected to a normal point load. The solutions corresponding to this stress field configuration were first formulated by Boussinesq in 1885 [70Tim]; these are summarized in the Appendix 1. This approach enables the determination of stress contours of the three principal normal stresses formed under contact.

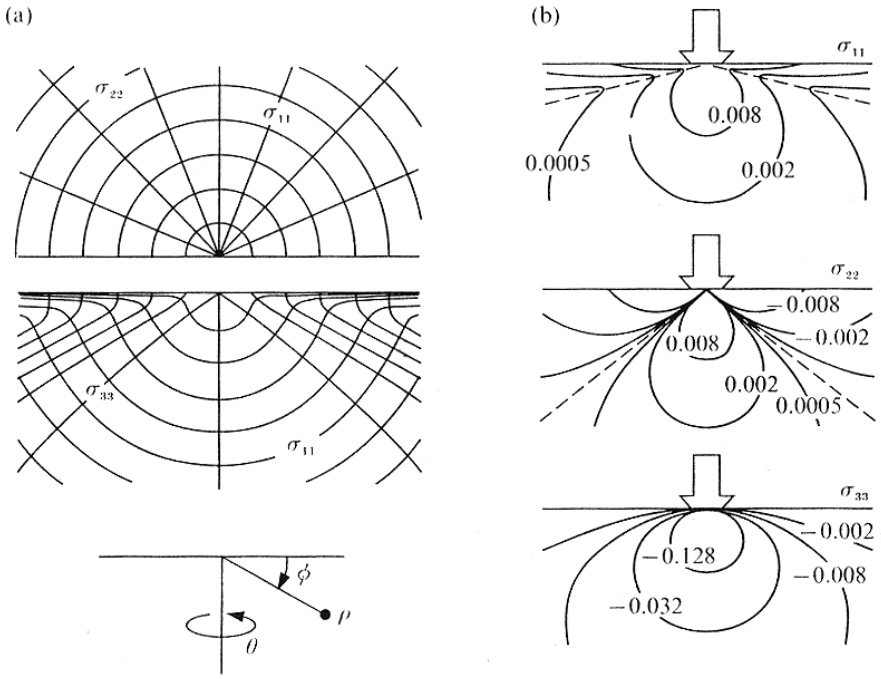

Figure 5.1. Boussinesq field for principal normal stresses σ_{11}, σ_{22}, and σ_{33} plotted for $\nu=0.25$. (a) stress trajectories (tangents to which denote direction) shown in half surface view (top) and side view (bottom); (b) contours (numbers on which denote magnitude) shown in plane containing contact axis (side view). Note sharp minimum in σ_{11} and zero in σ_{22}, indicated by broken lines. After [93Law].

The stress field is axisymmetric around the force direction (Figure 5.1a), and the stress components σ_{ij} have the following general form in spherical coordinates (ρ,θ,φ)

$$\sigma_{ij} = \frac{P}{\pi R^2}\left[f_{ij}(\phi)\right]_\nu \qquad (5.1)$$

where P is the applied load, R the radial distance from the point of contact, and $\left[f_{ij}(\phi)\right]_\nu$ an independent angular function which is itself a function of Poisson' s ratio ν.

These stresses are defined such that $\sigma_{11}>\sigma_{22}>\sigma_{33}$ everywhere, and their magnitude falls off rapidly with distance from the contact point. The σ_{11} and σ_{33} stresses lie in planes of symmetry through the load axis. The σ_{11} stress is tensile at all points in the field, and shows a maximum at the surface (ϕ=0) and along the contact axis (ϕ=π/2) (Figure 5.1b). Stress σ_{22} which encircles the contact (hoop stresses) is tensile in the region below the indenter but compressive near the surface (Figure 5.1b). In contrast, σ_{33} is everywhere compressive (Figure 5.1b).

The singularity at *R=0* in Equation (5.1) is a characteristic of the Boussinesq field, and a consequence of the implicit assumption of a zero contact area for supporting the applied load. In reality, the contact is accommodated elastically or plastically over a nonzero area of characteristic linear dimension *a*, to relief the high stress concentration about the singular point and to avoid a stress singularity. In that sense the field can be characterised by two scaling quantities [75Lawa], *i.e.*

- in spatial extent, by the contact dimension *a* itself
- in intensity, by means of the contact pressure that is given by

$$P_0 = \frac{P}{\alpha a^2} \tag{5.2}$$

where P is applied load and α is a constant dependent upon the geometry of the indenter.

For an indenter which leaves a geometrically similar impression in a homogeneous specimen at all loads, the mean indentation pressure remains invariant and accordingly provides a measure of the hardness of the material [51Tab].

Shear and hydrostatic compression components of the stress filed can be derived from the principal normal stresses (see Appendix 1). Since the intensities of these components substantially exceed those of the tensile stress, typically by an order of magnitude, the indentation contact stress field is dominated by them [75Law]. As a consequence, immediately under the contact, especially in sharp contacts, the material may be irreversibly deformed leaving a residual, plastic impression.

5.1.2. Inelastic deformation field

Physically, in the case of a sharp indenter, the singularity in Boussinesq stress field is averted by irreversible inelastic deformation beneath the indenter point until the contact is large enough to support the load. Two basic, competing processes dominate within the contact zone in any given material:

- shear induced flow, either plastic or viscous, associated with the conservation of volume under indentation. This is often referred to as "normal" indentation behaviour. Most brittle materials, including a wide range of glasses with a substantial amount of network modifiers in the structure (network-modified glasses, *e.g.* soda-lime glass, aluminosilicate glass), behave in this way [79Aro].
- pressure induced densification involving a phase change or compaction of an "open" microstructure. This is referred to as "anomalous" indentation behaviour. Glasses with an "open structure" containing network formers (network-forming glasses, *e.g.* fused silica and borosilicate glasses) behave in this manner [79Aro,00Zie]. Moreover, porous or phase-transforming ceramics (*e.g.* materials containing ZrO_2) can accommodate the indentation volume, at least partially, by structural densification [83Coo].

Each type of deformation is characterized by its own, complicated stress-strain response, according to the limiting stress level (yield stress or densification pressure) that is possible within the material.

A simple, but generally accepted model for inelastic deformation within ideal elastic-plastic contacts in glasses was proposed by Marsh [64Mar]. The idealization includes the assumption that the inelastic component of the deformation is a constant volume, radial displacement process, characterized by a well defined yield stress. Starting from the fact that the material is often displaced radially outwards from the indentation, this model assumes spherical symmetry in the deformation field below the indenter (Figure 5.2). Noteworthily, later experimental observations have provided evidence that the plastic zone exhibits spherical symmetry [78Hag].

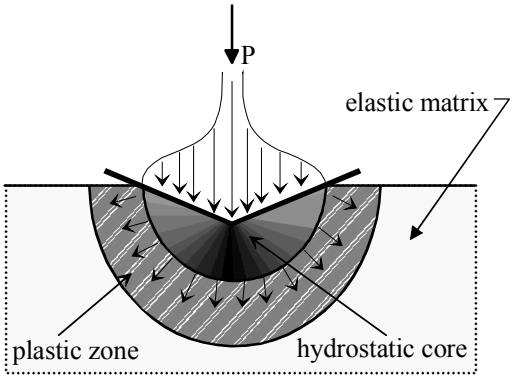

Figure 5.2. Schematic representation of the model for elastic-plastic indentation according to Marsh. P is the applied load.

More specifically, this model assumes that

- immediately below the indenter the material behaves as an outwardly expanding core, exerting a uniform hydrostatic pressure on the surrounding material;
- an ideally plastic region encases the core;
- beyond the plastic region lies the elastic matrix.

The assumptions made within Marsh´s model constitute the basis of essentially all indentation studies performed so far.

In indentation experiments, the irreversible deformation within the contact zone does not allow full recovery of the initial stress-free state in the surrounding elastic matrix after one complete loading and unloading cycle. As a consequence, a residual stress field is built-up in the unloaded solid, which provides the primary driving force for the radial crack formation in the final stage [80Law]. In general, the volume of the plastic zone (V) is dictated by the main pressure contact (given by Equation (5.2)) and the indentation volume (ΔV). Accordingly, the relative plastic zone dimension β in the reference geometry is:

$$\beta = \left(\frac{V}{\Delta V} \right)^{1/3} . \tag{5.3}$$

For a pyramidal indentation with hemispherical plastic zone, ß is given as [82Cha]

$$\beta = \left(\frac{b}{a} \right) \left(\frac{\sqrt{2}\pi}{\cot \phi} \right)^{1/3} , \tag{5.4}$$

where b is the radius of the plastic zone, a is the impression half diagonal, and ϕ is the indenter half-angle.

The elastic-plastic field in the general indentation problem is extremely complex. However, a convenient approach is found by assuming that the volume of the plastic zone is identical to that of an expanding cavity under internal pressure, which illustrates the essential features of the stress distribution in the elastic-plastic field. Then Hill's mathematical solution [98Hil] to this problem can be used. According to Hill's expanding cavity model, the relative plastic zone size (β) is linked to the ratio of Young's modulus (E) and hardness (H) of the indented material as

$$\frac{E}{H} = \frac{9\left[(1-\nu)\beta^3 - 2/3(1-2\nu)\right]}{2\left(1+\ln \beta^3\right)}, \tag{5.5}$$

where ν is Poisson's ratio. The quantity E/H represents an important parameter to quantify the accommodation of material inside the elastic-plastic contact zone. This is apparent from the

fact that H determines the loading half-cycle, while E determines the unloading half cycle. Accordingly, higher E/H ratios (*e.g.* in hard ceramics) correspond to a lower residual stress field intensity, implying a stronger elastic recovery and, thus, more pronaunced radial extension during the unloading half-cycle [93Law].

5.2. Mechanics of indentation fracture

Considerable effort has been devoted to explain two important aspects of indentation fracture mechanics with respect to crack formation. These are:

- initiation (how and where in the indentation field the cracks start);
- propagation (once started, what path do the cracks take, and what determines the extent of their growth).

Of these two, initiation is less amenable to quantification in terms of basic material properties. Crack initiation begins from "flaws", which are either pre-existing [75Lawb] or induced by the indentation process itself [79Haga]. Pre-existing flaws occur typically as micron-scale cracks. Their nature and distribution depend in a complex way on the mechanical, thermal and chemical history, but relate most commonly to the susceptibility of brittle surface to contact and handling damage. Deformation-induced flaws tend to nucleate at points of intense stress concentration in front of locally impeded bands or zones of inelastically deformed material. According to the Boussinesq stress field, in which the tensile stress σ_{11} is maximal at the specimen surface and contact axis (Figure 5.1b), the crack will tend to initiate at one of these favoured locations [75Law]. Thus, provided the surface does not contain severe handling damage, crack initiation would be expected to occur preferentially below the contact point [82Chia]. On the other hand, since brittle cracks have the tendency to propagate along paths normal to the greatest tensile stresses [93Law], the fully developed cracks will lie on either the quasi-conical (σ_{22}-σ_{33}) or median (σ_{11}-σ_{33}) trajectory surfaces (Figure 5.1b).

5.2.1. Type and formation of cracks in contact fields

The type of the created cracks, as well as their formation mechanism, vary according to the nature of the brittle material and the indenter geometry. Moreover, the stage at which the cracks form (*i.e.* upon loading, unloading or at peak load) is strongly influenced by the relevant material parameters, Young's modulus E and hardness H [90Coo]. Experiments have revealed four major crack types that differ in morphology, sequence and nucleation position. These are the cone, median, shallow radial and lateral cracks.

5.2.1.1 Spherical indenter - Cone cracks

Cone cracks are commonly generated by the elastic loading of spherical or 'blunt' indenters [75Law, 75Lawb]. However, these cracks can also be observed for sharp indenters in case of glasses showing "anomalous" behaviour, *e.g.* borosilicate [79Aro, 02Ber] or fused silica glass [82Ish, 79Hag]. Their first observation by Hertz in 1881 during his examination of solids under elastic contact has led to the term ´Hertzian cone cracks´. The cone crack formation is schematically illustrated in Figure 5.3. It starts with the nucleation of a precursor circular crack (indicated by dashed line) at the specimen surface, just outside the elastic contact (shaded region) where the principal tensile component σ_{11} reaches its maximum (Figure 5.3a). Pre-existing flaws on the specimen surface (short dashes) play the main role for the crack initiation [79Haga]. When the critical load is reached, the surface circular crack becomes unstable and propagates from the surface downward at a characteristic angle to the load axis, which results in a cone crack (Figure 5.3b). Upon unloading, the cone cracks tends to close (but rarely to heal), and on the surface a circular crack becomes visible (Figure 5.3c). If additional cracks appear in the system, which usually occurs with sharp indenters, the cone crack is first nucleated, then it propagates during loading and finally it gets closed during unloading [86Cha].

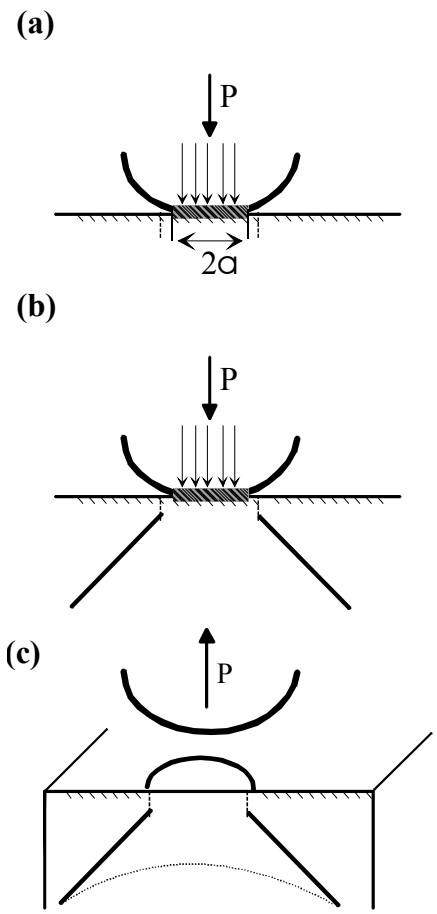

Figure 5.3. Evolution of a cone crack during blunt indentation. (a) nucleation of ring crack at the surface; (b) downward propagation of the crack; (c) final crack shape (side and surface view). P and a are the applied load and resulting contact size, respectively.

5.2.1.2 Sharp indenter – Median, radial and lateral cracks

Figures 5.4-5.7 illustrate the basic sequences during the evolution of cracks patterns crated by the Vickers pyramidal indenter. In the initial stage of loading, an inelastic deformation zone (plastic zone, depicted as a grey region in Figures 5.4-5.7) is formed.

At a critical indenter load, median cracks initiate below the contact point at the elastic-plastic interface where the stress concentration is maximal (Figure 5.4a) [77Law]. In general, the nucleation sites are created by the actual deformation process that causes intersecting shear or slip bands beneath the indenter (named "shear faults") [78Hag], although pre-existing surface flaws can sometimes act as suitable nuclei [76Evaa, 79Swa]. Different values of critical applied load have been reported to be necessary for median crack formation [80Law, 82Ish, 90Coo, 92Smia]. Median cracks consist of two mutually perpendicular penny shaped cracks which lie in directions parallel to the indenter diagonal. With increasing load, the median cracks become unstable and propagate incrementally downward, until their maximum size is reached for the peak load (Figure 5.4b). Upon unloading, they close up below the surface but simultaneously expand towards the indented surface forming the final crack with half penny shape (as indicated by the dashed lines in Figure 5.4c) [75Lawb, 76Phi]. Crack extension is primarily directed along the corners of the remnant impression [75Lawa]. The terminology is now changed: the surface cracks are referred to as radial, whilst the subsurface cracks are still referred to as median. In the literature, this crack system is often termed 'median- radial' crack system. [79Mar]. For many ceramics with low fracture toughness values, apparently only median–radial crack systems develop during Vickers indentation [89Li].

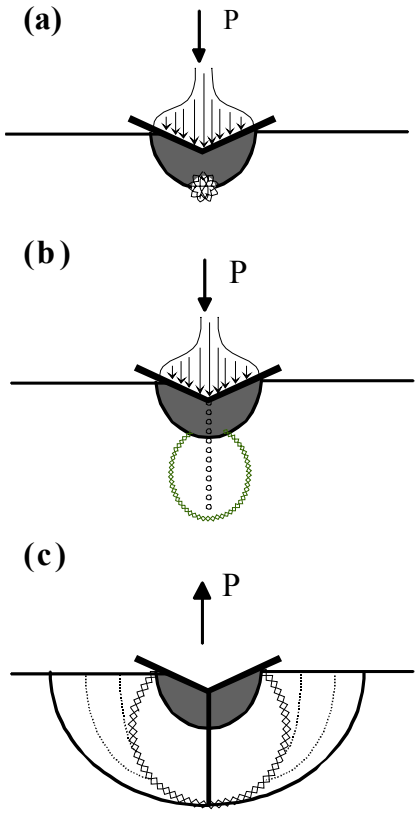

Figure 5.4. Evolution of the median crack system associated with Vickers indentation. (a) the crack nucleates at the bottom of the plastic zone (b) downward propagation (c) expansion towards to surface

Generally, when applied loads are smaller than the critical load for median crack formation [82Nii, 79Lana] or when the specimen has a rough surface [82Lan], shallow radial cracks can form (Figure 5.5). This also tends to happen with materials which have a very high toughness [84 Bin], or when small spherical indenters are used (indenter radius $r < r_{cr}$ for sharp indentation) [76Evaa]. This type of crack is often called ´Palmqvist´ crack after its discoverer, who first observed it in the WC-Co system [57Pal]. During loading, nucleation of shallow

radial cracks occurs on the specimen surface at the edge of the plastic contact impression, usually at the indentation corner (Figure 5.5a) [79Lan, 81Lan]. Propagation of these cracks, however, is prevented until unloading. Just prior to complete removal of the indenter they start to grow both in length and depth, parallel to the load axis (Figure 5.5b), resulting in four mutually perpendicular, semielliptically-shaped cracks. Experimental observations on the crack geometry [76Evaa, 76Swaa] indicate that the maximum depth is approximately of the order of the indentation depth, while the crack shape can differ from elliptical (for cemented carbides) to circular (in case of ceramics) [85She]. Such partially formed cracks tend subsequently to propagate downward and merge beneath the plastic zone into half–penny geometry, either during unloading [98Gre] or post-indentation growth [93Law] (Figure 5.5c). The radial-median crack system formed in this way is not of fully half penny shaped, but rather slightly semielliptical [95Sgl].

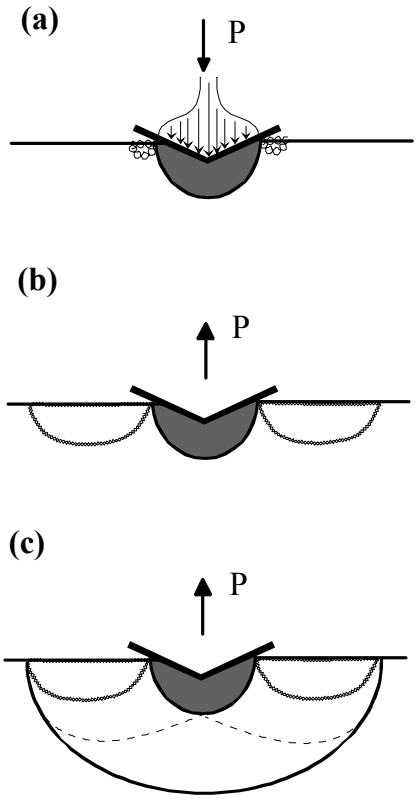

Figure 5.5. Evolution of the shallow radial crack system associated with Vickers indentation. (a) nucleation at the corner of indentation contact; (b) growing in length and depth; (c) propagation downward and formation of half–penny shaped crack

A second type of cracks that occurs for Vickers indentation are lateral cracks (Figure 5.6) [78Hag, 80Hag, 82Mar, 01Whi]. They are generated below the surface regardless of whether the threshold for median crack initiation is exceeded. It has been found that the maximum stress for lateral crack propagation occurs at the depth of the contact impression [76Evaa]. Lateral cracks nucleate at the beginning of the unloading part of the cycle (usually at about 10% of the maximum load [76Swaa]), and grow upon further unloading outwards from the site of the plastic deformation in a plane parallel to the surface (Figure 5.6a). If the applied load is too high for the given specimen then these lateral cracks tend to divert upwards toward the surface, and can result in material removal at the surface – this process is called “chipping” (Figure 5.6b,c) [75Lawc].

One of the most important characteristics of both the lateral and radial cracks is their growth to the final length as the indenter is unloaded [75Lawb, 76Swa]. This observation has led to the assumption of a residual stress, generated as a result of incompatibility between the deformation zone and the surrounding elastic material as the prime driving force for crack propagation. The importance of residual stresses is in agreement with the observation that during elastic contact, lateral and radial cracks are not generated due to the absence of plastic deformation. Different behaviour is found for median and cone cracks, which are closed during unloading.

The mechanical mismatch results in a "reversed field" prior to complete withdrawal of the indenter. Accordingly, the stresses which were tensile upon loading and acted to open up the median cracks, now tend to compression. Near the surface, however, the reverse effect occurs: The original compressive stress becomes tensile and any partially formed penny cracks evolve into the full half penny shape. The residual stress state thus created ensures that a crack configuration close to the ideal half-penny shape invariably occurs at the end of the indentation cycle (Figure 5.7) [75Lawb]. In addition, the dwell time influences the final shape of the median-radial crack system. While short dwell times lead to semicircular cracks, a more semielliptical shape is obtained for longer times (varied between 5 s and 30 min) [95Sgl]. It should further be noted that median and radial cracks are associated with strength degradation [81Lawa], whereas lateral cracks are linked to erosion and wear due to their tendency to chipping [98Gre].

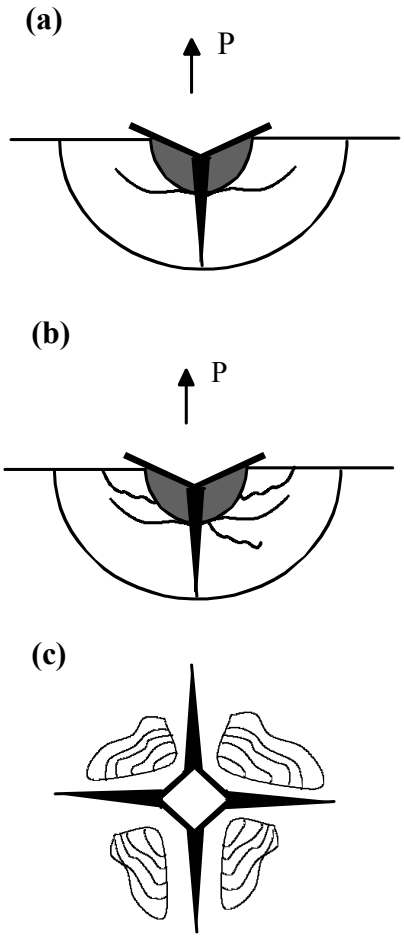

Figure 5.6. Lateral crack system associated with Vickers indentation. (a) crack nucleation at the bottom of plastic zone and propagation outwards from the seat of plastic zone. Propagation toward the specimen surface - the "chipping" effect - in cross sectional (b) and plane view (c).

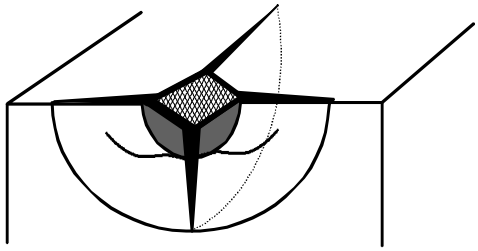

Figure 5.7. Final configuration of median –radial and lateral crack system resulting from Vickers indentation.

5.2.2. Subcritical crack growth

It has been observed that after indentation of ceramic materials, both the median-radial and lateral cracks can undergo subcritical growth, propagating primarily along the surface [81Wie]. After this process, the surface trace dimension can be almost twice the length of the initial crack [95Sgla]. Although there are several possible mechanisms for subcritical crack growth, most attention has been directed to stress corrosion [81Wie, 81Gup, 93Coo].

The relation between the crack velocity v and the stress intensity factor K for intrinsically brittle solids in active environments is well established, and presented by v-K curves (Figure 5.8). There are three distinct regions designated as I, II and III. Each region shows a characteristic dependence on stress intensity and extraneous variables such as concentration of active environmental species [67Wie]. At low values of stress intensity there often appears to be a threshold K_0, below which crack growth does not occur [91Fet, 02Ber]. Low crack velocity (region I) depends sensitively on K and chemical activity. It usually is associated with chemical interaction of the environmental molecules with the strained crack tip bonds (Figure 5.9). A plateau region (region II) often follows, which is associated with the inability of reacting species to keep pace with crack tip motion (transport limited case). The final region (region III) is insensitive for environment, and usually associated with the kinetics of intrinsic bond rupture, when critical stress intensity factor(K_C) is reached in the material.

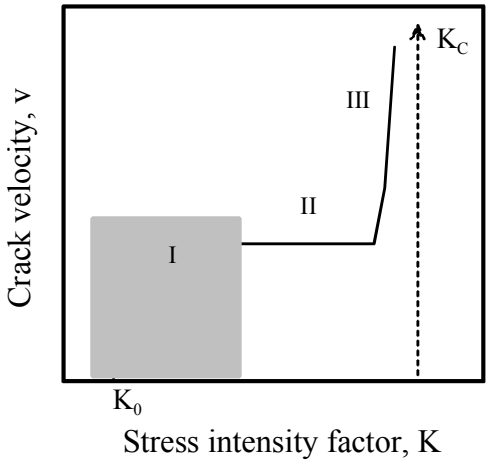

Figure 5.8. Schematic of a general subcritical crack velocity v-***K*** curve showing the differing mechanistically controlled regions. The grey region denotes the most important region

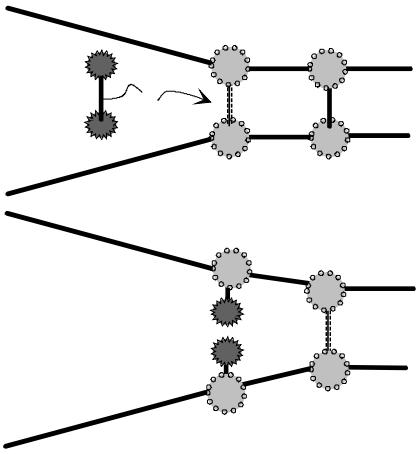

Figure 5.9. Schematic model for chemical reaction of environmental species on strained crack tip bond.

The threshold and region I behaviour is of special importance to engineering ceramic materials, which often spend most of their "life time" in this region. An adequate description for $K \geq K_0$ is achieved by an empirical power law, which expresses the crack velocity as

$$v = v_0 \left(\frac{K}{K_C} \right)^n , \qquad (5.6)$$

where n and v_0 are the sub-critical crack growth parameters. In general, these parameters depend on the choice of material, environment as well as temperature [81Wie].

The subcritical crack growth in silicate glasses originating from chemical interaction of the indent with the environment (within region I), especially with atmospheric humidity, has attracted by far the most attention in the literature on ceramics [72Wie, 90Ger, 96Sgl, 99Gre]. Humidity can affect the crack system in silicate glasses in two ways. In the first case it penetrates into the crack front, and the formed hydroxyl ions react with the strained siloxane bonds in the silicate network, thus effecting crack propagation [82Mic]. As the second possibility, moisture diffuses into the damaged zone, which may result in a decrease of the strain mismatch of this zone within the surrounding elastic matrix [87Law].

Apart from chemical activity, residual stress plays another important role for subcritical crack growth. Relaxation of the residual stress has been observed to occur by crack extension as well as by diffusion processes in the deformed zone [89Han]. Since radial cracks are more exposed to the environment, this type of cracks will suffer more from environmental attack than lateral cracks. The crack depth, in contrast, does not increase with crack extension and appears to be controlled by the intersection with the lateral cracks [92Smi, 95Sgla].

5.3. Indentation toughness evaluation

Observation of the crack evolution during indentation reveals that the surface crack growth occurs upon unloading, *i.e.* when the constraining elastic stresses are removed. This indicates that a residual stress field, induced by the irreversible deformation within the elastic-plastic zone, is the driving force for crack growth. Because of decreasing stress field, the stress intensity factor of a radial indentation crack decreases as the crack length increases. Thus, an indentation crack is in equilibrium and the value of the stress intensity factor at the crack tip (K_{tip}) can be considered as the fracture toughness (K_C). However, due to subcritical crack growth, the stress intensity factor can further decrease with time (section 5.2.2.) which should be taken in account for fracture toughness determination. The importance of residual stress is reported in many circumstances [76Eva, 80Law], and various experimental observations [90Coo] as well as analytical modelling [82Chi, 82Chia, 91Lat] reveal that it is sufficient to

cause “pop–in” and extension of the radial cracks during the unloading process. Furthermore, the critical load for unstable propagation of the crack nucleus to form the observed crack is related to the fracture resistance of the material. On this basis, measurement of the crack length [75Law] has been developed into a method for fracture toughness determination of brittle materials. In addition, determination of the crack opening profile [90Röd] has more recently been proposed for this purpose.

5.3.1. Indentation crack length (ICL) method

It was demonstrated by Palmqvist that the length of cracks, which emanate from the corner of an indent, can be empirically related with the toughness of the investigated material [57Pal]. This observation set the ground for a fundamental approach for determining fracture toughness by crack length measurements, as developed by Lawn et al. [75Law, 75Lawa, 75Lawb]. The indentation crack length (ICL) method, most often using Vickers indentation, has been widely applied for fracture toughness determination, especially for glasses and ceramics. This procedure involves measurement of:

- the half indent size (a), and the lengths of the cracks (c) that emanate from its corners (Figure 5.10);
- the applied indentation load (P).

Measurements of indentation crack length should be done as soon as possible after withdrawal of the indenter owing to the possibility of subcritical slow crack growth which tends to reduce the determined value of K_C.

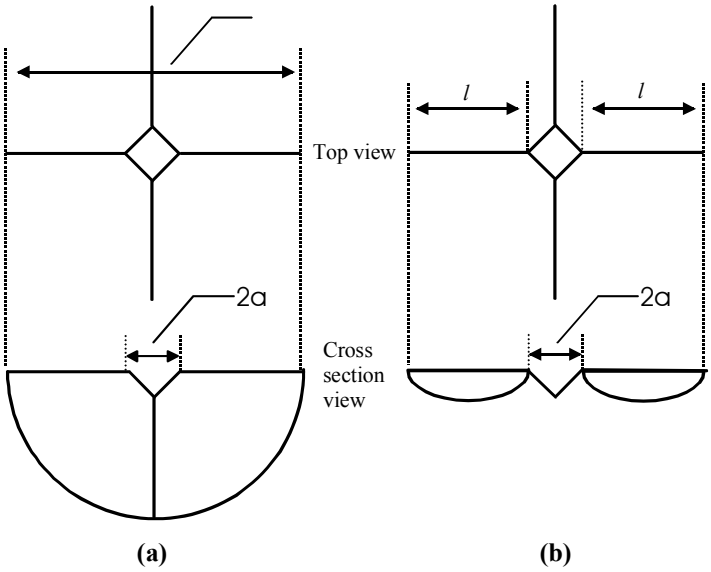

Figure 5.10. Schematic representation of geometry and characteristic parameters of the radial/median (a) and radial Palmqvist (b) crack system around a Vickers indent

The main advantages of the crack length approach are:

- the small size of specimen required for a large number of indents;
- the speed with which many results may be obtained.

Numerous semi-empirical equations (Table 5.1) relating fracture toughness to the measured indentation parameters have been derived based on experimental observations and/or theoretical considerations

Table 5.1. Equations available in the literature for estimation of fracture toughness via the ICL method with Vickers geometry *

K_C, [MPa $m^{1/2}$]	Author
Radial - median- crack system	
$[(1-2\nu)(\alpha H)^{1/2}(P/c)^{1/2}]/[2^{1/2}\pi 2\beta]$	*Lawn et al.* [75Law]
$0.0726(P/c^{3/2})$	*Lawn et al*. [75Lawb]
$0.0752(P/c^{3/2})$	*Evans et al.* [76Eva]
$0.129(c/a)^{-3/2}(H/E\phi)^{-0.4}(Ha^{1/2}/\phi)$	*Niihara et al*. [82Nii]
$0.014(E/H)^{0.5}(P/c^{3/2})$	*Lawn et al*. [80Law]
$0.016(E/H)^{0.5}(P/c^{3/2})$	*Anstis et al.* [81Ans]
$0.010(E/H)^{2/3}(P/c^{3/2})$	*Laugier* [85Lau]
$0.0752(P/c^{3/2})$	*Tanaka* [87Tan]
$[(c/a)^{(c/18a)-1.51}Ha^{1/2}(H/(E\phi))^{-0.4}\alpha]/\phi$	*Liang et al*.[90Lia]
$0.046(EH)^{1/2}(a^2/c^{3/2})$	*Gong* [99Gona]
$0.044(EH)^{1/2}(a^2/c^{3/2})$	*Gong* [01Gon]
Palmqvist crack system	
$0.035(l/a)^{-1/2}(H/E\phi)^{-0.4}(Ha^{1/2}/\phi)$	*Niihara et al.* [82Nii]
$0.048(l/a)^{-1/2}(H/E\phi)^{-0.4}(Ha^{1/2}/\phi)$	*Niihara et al.* [83Nii]
$(HP/41)^{1/2}/[3(1-\nu^2)(2^{1/2})\pi\ \tan\psi)^{1/3}$	*Shetty et al.* [85She]
$0.015(l/a)^{-1/2}(E/H)^{2/3}(P/c^{3/2})$	*Laugier* [87Lau]
Mixed type of median-Palmqvist crack	
$0.142(Ha^{1/2})(E\phi/H)^{0.4}(c/a)^{-1.56}/\phi$	*Lankford* [82Lan]

** E - Young's modulus; H - Vickers hardness; ϕ - constraint factor (≈3); α - geometry constant of indenter (=2/π); b – dimensionless factor (≈2); n – Poisson's ratio; ψ – half apex angle of the Vickers indenter (=68°); v is Possion ratio;P – applied load on indenter; a, c, and l are as shown in Figure 5.10.*

The semi-empirical equations can be classified into three groups. The first group applies to well-developed radial-median cracks with half penny geometry. The second group is based on

the assumption of radial Palmqvist cracks. Distinction between radial-median and radial Palmqvist cracks has been made by using the crack length to indent ratio (c/a). It has been found that for small ratios (c/a ≤2.5), the crack profile is of Palmqvist type [82Nii]. In the third group, it is considered that Palmqvist cracks behave identically as fully developed radial-median cracks, as has been argued by Lankford [82Lan]. It is noted, however, that such equations have led to significantly varying fracture toughness values, obtained from the same set of data [99Ray].

The equation proposed by Anstis et al. [81Ans]

$$K_C = 0.016\left(\frac{E}{H}\right)^{0.5}\frac{P}{c^{3/2}}, \tag{5.7}$$

has proven to be most accurate, and has, therefore, been used extensively. It was extended on the basis of a model proposed by Lawn, Evans and Marshal (often referred to as LEM model in the literature) [80Law]. The main assumptions within the LEM model are that (i) fully-developed indentation cracks in ceramics are of half-penny shape, (ii) the residual stress is concentrated at the point located at the crack center at the elastic/plastic interface, and acts as crack mouth opening point force, and (iii) the volume of the indentation plastic zone can be equated to that of an internally pressurized spherical cavity, allowing the use of Hill's solution for the expanding spherical cavity (discussed in section 5.1.2). Based upon these postulations, the fracture toughness K_C (critical stress intensity factor) is predicted to depend on the indentation load and radius of the crack according to

$$K_C = \chi\frac{P}{c^{3/2}}. \tag{5.8}$$

The coefficient χ characterizes the residual elastic/plastic contact field, which drives the radial cracks during [79Mar] and even after [85Law] unloading. It is the residual component of the contact stress field that determines the ultimate radial crack size in Vickers indentations. Detailed consideration of the manner in which the volume of the plastic impression is accommodated by the surrounding elastic matrix shows that χ is proportional to the square root of the ratio between Young's modulus and hardness [76Swa]:

$$\chi = \delta\left(\frac{E}{H}\right)^{1/2}, \tag{5.9}$$

where δ is a dimensionless constant that is primarily a function of the indenter geometry according to:

$$\delta = \xi(\cot\phi)^{2/3}, \tag{5.10}$$

where ξ is a dimensionless constant and ϕ the indenter half-angle.

The constant δ is generally regarded as material independent, and usually determined by averaging data obtained from reference materials with known fracture toughness. Anstis and co-workers, who calibrated the constant δ by plotting data obtained from Vickers indentation in a wide range of ceramic materials as $P/c^{3/2}$ versus K_C (obtained by the double cantilever beam technique), found a value of δ= 0.016±0.004 [81Ans].

In selecting standard materials for calibration, candidates are sought for which the deformation response is as close as possible to ideal. This is fulfilled when irreversible deformation occurs with volume conservation ("normal" indentation behaviour). The results of Anstis et al. [81Ans] may be taken as evidence that many ceramic materials behave in this manner. However, brittle materials that densify or compact below the indenter, or that undergo phase transformations beneath the indenter ("anomalous" indentation behaviour), would not be expected to fall within this group. They are rather characterized by substantially diminished residual stress intensities at indentation sites, with consequently reduced radial crack lengths [79Aro]. Thus, evaluation of crack lengths in these materials using equations with calibrated parameters can lead to gross overestimates of fracture toughness [83Coo]. Hence the quantity δ in Equation (5.9) is then no longer material-independent, and the constant ξ in Equation (5.11) must depend on the nature of deformation. This places the universality of Equation (5.7) in question, and it follows that the constant ξ should be smaller for the densification than for volume conserving processes, since in the former the indentation strain can be relaxed by compaction as well as by elastic compression within the deformation zone [93Law].

In addition to this complication, there are several further disadvantages inherent to the ICL method:

- the derived K_C values deviate often by ~30% from those obtained by conventional methods [84Bin];
- all indentation fracture models given in the literature assume that either one or the other of two idealised crack systems is formed during indentation testing, which may or may not be the case for the material in question;
- the wide diversity of indentation fracture toughness equations reported in the literature.

5.3.2. Crack opening displacement (COD) method

An alternative method of toughness determination consists of measuring the COD along the length of radial cracks. As an important advantage over the ICL method, the COD approach does not require calibration parameters, and is therefore applicable to a wide range of materials, independent of the crack shape. In addition, the COD method enables the quantitative evaluation of residual stresses at the contact site.

The crack opening profile of indentation radial cracks can be approximated by the Sneddon double integral equation [69Sne], which has the following general form:

$$u(r,c) = \frac{1}{E'}\int_{r}^{c} h(c',r')\left(\int_{0}^{c'} h(c',r')\sigma(r')dr'\right)dc', \qquad (4.11)$$

where u is half the crack opening; the radial coordinate (r) is related to the crack tip coordinate x and the crack length c (r=c-x); r' and c' are integration variables while $\sigma(r')$ describes the distribution of applied stresses. E' is the Young's modulus for plane strain ($E'=E/(1-\nu^2)$), and *h* is a Green's weight function.

In order to use this double integral for indentation radial cracks, the problem arises that the stress that drives the crack opening ($\sigma(r')$) is not known (as in the case of applied stresses), and has therefore to be determined. Moreover, the stress distribution is more complex due to the presence of both an elastic and plastic stress field around the indent. The solution to this problem is an issue under current investigation. Until now, two different materials have been considered, namely soda-lime glass [93Röd] and alumina [97Sei], in both cases by using a simple fitting procedure. In order to get an accurate solution, however, a full numerical evaluation of the COD data would be required.

With the aid of the double integral (Equation (5.11), the pre-crack residual stress σ(r') can in principle be determined from measurements of the crack opening along the crack. The relevant geometrical parameters, referring to the indent impression with the crack system, that have to be measured for this approach are indicated in Figure 5.11a.

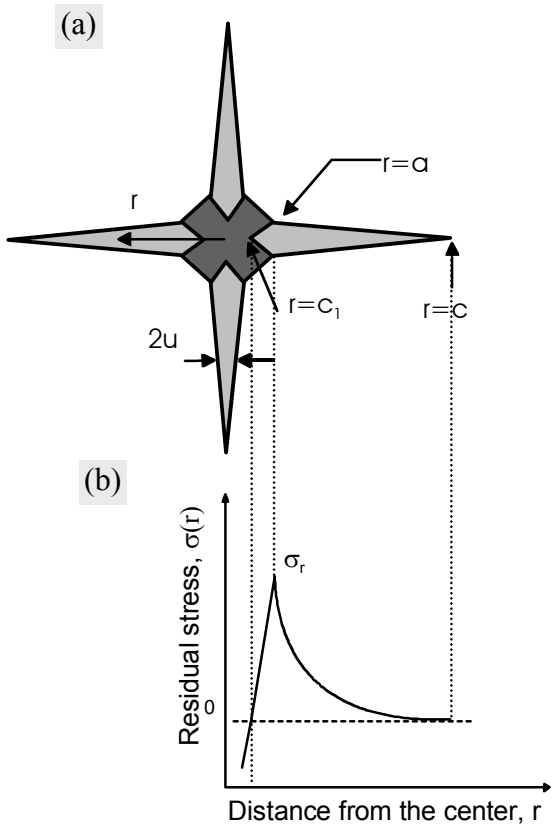

Figure 5.11. Schematic representation of the radial crack system around a Vickers indent with relevant geometric parameters where c is the crack length, c_1 the inner tip of the crack, a the half diagonal of the indent impression, 2u the crack opening and r the radial coordinate (a); residual stress distribution along the crack, σ_r maximum residual stress (b).

Residual stress formed due to accommodation of an irreversibly deformed volume, that drives the opening of the crack in mode I, has the characteristic of a tensile-hoop stress. Its maximum (σ_R) occurs at the mismatch region between the elastic and plastic field after unloading [82Chi]. Consequently, in the vicinity of the impression corner the radial cracks "pop in" from shear faults [91Lat, 91Lata] and the maximum crack opening is reached at r=a, where the distance r from the indenter center is equal to the half diagonal a of the indent impression (Figure 5.11b). Inside the highly compressive plastic zone (c_1<r<a) the residual stress decreases rapidly from its maximum towards the indentation center and reaches zero at r=c_1. Closer inwards (r<c_1), the hoop stress becomes compressive (σ(r)<0).

The residual stress distribution inside the plastic zone can be expressed by the following linear equation [98Hil]:

$$\sigma(r) = -k\sigma_R + (k+1)\left(\frac{r-c_1}{a-c_1}\right) \qquad (c_1<r<a), \qquad (4.12)$$

where k is a load-dependent constant that determines how far the crack will propagate [93Röd].

On the other hand, the monotonous decrease of the residual stress outside the plastic zone (a<r<c) can be described by the following power-law equation:

$$\sigma(r) = \sigma_R \left(\frac{a}{r} \right)^m \qquad \text{(a<r<c)}, \qquad (5.13)$$

with the parameter m determining how rapidly the stress decreases with distance. Within Hill's model of an expanding sphere, m assumes the value of 3 [98Hil].
Therefore, for an indentation crack, the distribution of residual stresses that are caused by indentation must be inserted in the double integral as sum of two stresses according to Equations (5.12) and (5.13) [95Fet].

Fracture toughness becomes directly available when the solution of the crack opening function (4.11) is restricted to the near-tip region. This approach is based upon the crack profile for constant applied load under Mode I conditions [57Irw], and exploits the fact that the applied stress intensity (K_A) is transferred to the stress field at the crack tip (K_{tip}), the near-tip half crack opening (u) shows a parabolic dependence on the distance (x) from the crack tip [90Röd]:

$$u(x) = \frac{K_{tip}}{E'} \sqrt{\frac{8x}{\pi}} \, . \qquad (4.14)$$

In this equation, K_{tip} is the stress intensity factor at the crack tip, and E' is Young's modulus for plain strain. The K_{tip} value can be obtained by fitting a parabolic profile to the measured crack tip COD as a function of the distance from the crack tip. This approach was introduced by Rödel et al. for compact tension (CT) specimens [90Röd], including alumina [90Röd, 97Sei] and whisker-reinforced alumina [91Röd]. However, for using this method to determine K_{tip} from indentation, a complication arises because only a small part of the COD profile close to the crack tip is of parabolic shape. At larger distance from the tip, due to the high residual stress originating from the region near the indent, the parabolic shape can be severely distorted (Figure 5.12). In order to account for this deviation, Seidel et al. [97Sei] suggested a phenomenological fit for the measured COD data within a more extended range from the crack tip by

$$u(x) = Ax^{1/2} + Bx^{5/2} \, . \qquad (5.14)$$

The first term describes the parabolic crack tip profile as in Equation (5.13), whereas the second term accounts for the distortion due to residual stress. To date, a preliminary trial to use this phenomenological approach for determining the fracture toughness has been performed with a polymer derived amorphous SiCN ceramic obtained by a powder technique [01Bau], however without thorough evaluation of the accurateness of the obtained results.

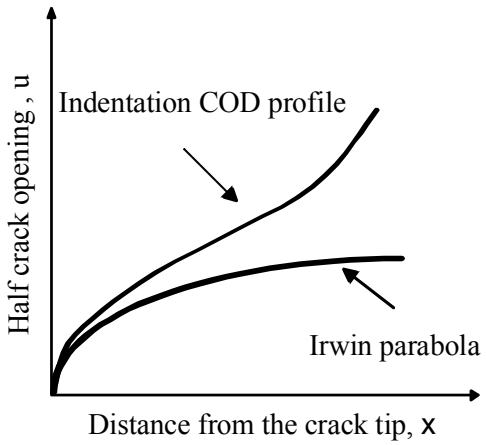

Figure 5.12. Schematic representation of the crack tip COD profiles.

An alternative method for fracture toughness determination using indentation COD measurements, involving the overall crack opening profile, has been developed by Haubensak et al. [97Hau]. For that purpose, the following equation was proposed

$$K_C = \frac{(COD)E}{F(r/c)c^{1/2}}, \qquad (5.15)$$

where F(r/c) is a dimensionless crack shape factor which depends on the geometry and the mode of loading, c is the crack length and E is Young's modulus. In this study, the function F was determined by finite element method (FEM). Although the fracture toughness obtained for soda lime glass was in good agreement with the value obtained by the DCB technique, this method did not find widespread application which is mainly due to the complicated FEM-based evaluation.

6. Experimental methods

6.1. Materials

Commercially available soda lime glass (Euroglas Haldensleben, Dammmühlenweg 60, Haldensleben, Germany) and borosilicate glass (Duran, Schott-Rohrglas GmbH, Postfach 101152, Bayreuth, Germany) were selected as representative normal and anomalous silicate glasses, respectively.

These two glasses were selected due to their following properties. Firstly, they are inexpensive, widely available materials, which furthermore offer the advantages of transparency and isotropy. Secondly, extensive data relating to their mechanical properties are available in the literature, especially for soda lime glass. This makes them appropriate for testing the indentation methods that shall be used to determine the fracture toughness of ceramics. In this respect, one glass showing normal and another glass showing anomalous indentation behaviour have been chosen as suitable reference for materials whose behaviour is still unknown. The different indentation behaviour can be explained by the chemical composition of the two glasses (Table 6.1).

Table 6.1. Chemical composition of the glasses under investigation (wt.%)

Glass	SiO_2	B_2O_3	Al_2O_3	CaO_2	MgO	Na_2O
Soda lime	72	-	0.3	9	4	14
Borosilicate	81	13	2	-	-	4

The major difference in their composition relates to the larger component of network modifiers (sodium, calcium) in the soda-lime glass, whereas a significant amount of network former (boron) is contained in the borosilicate glass. The latter is characterised by a relatively “open” network structure (Figure 6.1b), which allows on one hand densification under the indenter. On the other hand, the modifying ions within the soda lime glass (Figure 6.1a) restrict densification, thus leading to volume conservation.

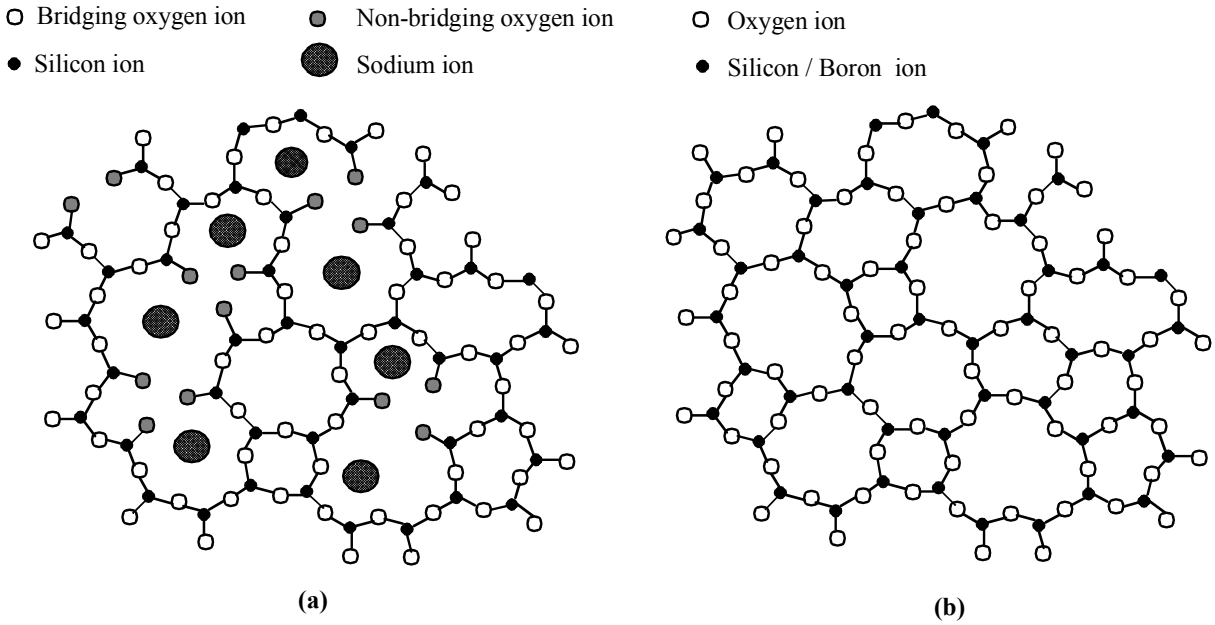

Figure 6.1 Schematic representation of the structure of normal (a) and anomalous (b) glass[97 Bar]

The third material investigated belongs to a new class of amorphous ceramics derived from polymers. This class of ceramics is very promising for structural applications, because they are known to exhibit high temperature stability, high creep resistance, retarded crystallization behaviour and low oxidation rates [02Bau]. The material investigated here was a fully dense amorphous polymer-derived SiCN ceramic produced by the casting route. The specific choice of investigating amorphous SiCN ceramics is motivated by the following reasons. First, only little information about the toughness of polymer-derived ceramics is currently available. In addition, since up to now mainly the powder technique has been utilized for their production, available fracture toughness values refer to amorphous ceramics that suffer from porosity. Moreover, in the literature no information is reported about the indentation behaviour of this class of materials, which would be required for a better understanding of their contact properties at the microscopic scale. This is relevant, *e.g.,* for machining. Finally, as the optimisation of the processing steps is still under development, a reliable method for fracture toughness determination would be very helpful for optimising their mechanical properties.

The polymer-derived amorphous SiCN ceramics were produced from the liquid commercial polysilazane precursor Ceraset (KiON Corporation, Pennsylvania, USA), as described by Janakiraman [03Jan]. This fabrication involves casting of the precursor in closed polytetrafluoroethylene (PTFE) circular moulds, followed by thermal crosslinking to produce cured glassy bodies. The latter are then further pyrolysed in argon atmosphere using a controlled heating program (heating rate 100 K/h and holding time 1 hour) to obtain fully dense, almost defect free ceramic bodies. A set of four different samples (SiCN-800, SiCN-

900, SiCN-1000 and SiCN-1100), produced at pyrolysis temperatures of 800°C, 900°C, 1000°C and 1100°C, respectively, was investigated. The elemental composition of these samples is presented in Table 6.2. It is seen that while the silicon and carbon content is almost constant, the amount of hydrogen decreases with increasing pyrolysis temperature. The presence of oxygen originates from exposure of the green bodies to air [03Jan].

Table 6.2. Chemical composition (wt%) of polymer derived SiCN ceramic materials [03Jan]

Sample	**Si**	**C**	**N**	**H**	**O**
SiCN-800	52.6	22.4	20.6	1.9	2.4
SiCN-900	52.7	22.2	22.2	1.48	1.4
SiCN-1000	53	22.7	21.2	0.97	2.1
SiCN-1100	54	22.1	21.5	0.75	1.6

6.2. Determination of elastic properties

The elastic properties Young's modulus, *E,* and Poisson's ratio, ν, of the glasses and SiCN specimens were measured by the impulse excitation method using a RDFA-MF apparatus (IMCE, B-3590 Diepenbeet, Belgium). In case of the glasses, rectangular samples with a length of 50 mm, a width of 25 mm, and a thickness of 0.32 mm were examined. Measurements on the SiCN ceramics were carried out with circular-shaped samples having a diameter of 12 mm and a thickness 0.4 mm. The corresponding results are summarised in Table 6.2.

Table 6.2. Measured values of Young's modulus (E) and Poisson's ratio (ν) of the materials studied

	Soda lime glass	**Borosilicate glass**	**SiCN 800°C**	**SiCN 900°C**	**SiCN 1000°C**	**SiCN 1100°C**
E, GPa	70.3	64	82	106	117	127
ν	0.220	0.200	0.245	0.240	0.220	0.216

6.3. Sample preparation

Glass samples were cut into rectangular shape with dimensions of 12 mm (length) x 5 mm (width) x 0.3 mm (thickness). The length was chosen to fit to the width of the AFM sample

holder. Prior to indentation, the surface of the glass samples was thoroughly cleaned with acetone.

Since the fully dense polymer-derived amorphous SiCN ceramics can be produced only as thin samples (0.45 mm thickness), a special preparation technique was developed to allow their use in the indentation experiments (Figure 6.2). For that purpose, plates of 2 mm width and 8 mm length were cut from the produced circular shaped samples with 12 mm in diameter (Figure 6.2a) and mounted into an alumina frame (Figure 6.2b). Since the plates were oriented with their side face upwards, a width corresponding to the sample thickness became available for indentation. In addition, this configuration ensured that the samples were self-supported, which is important for indentation testing of materials. In the last step, the sample surface was polished to a final roughness of ¼ µm.

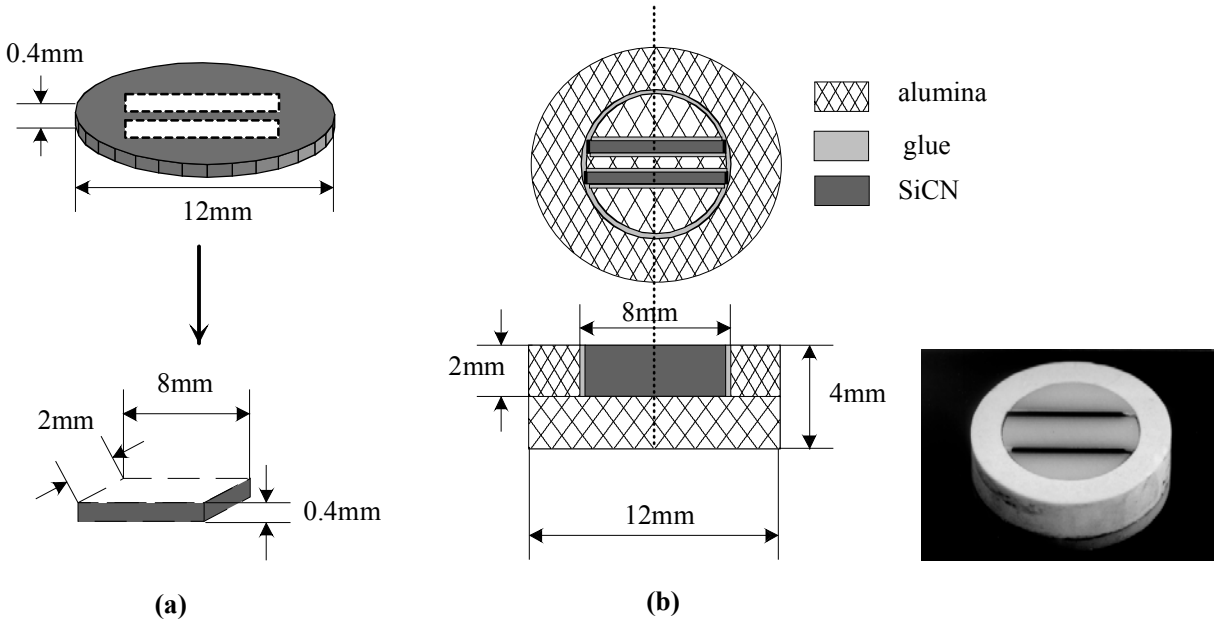

Figure 6.2. Schematic presentation of the polymer-derived amorphous SiCN ceramic samples. Plates were cut out of the produced samples (a). Plates mounted in alumina holder (b).

6.4. Indentation

Vickers indentation of samples was performed with a Buehler Micromet1 micro indenter for loads of 10 g - 1000 g (Buehler LTD, Lake Bluff, IL, USA), while for loads in the range of 1 kg -10 kg an indenter apparatus (Zwick & Co. KG, Einswingen, Germany) was used. All indentation tests were conducted in laboratory air (relative humidity 45-47%, temperature T=25°C) using a dwell time at the maximum load of 15s. The speed of the indenter at the instant of contact was approximately 0.3 mm/s. This particular procedure was employed in

order to obtain indentation cracks with an initial semi-circular shape [95Sgl]. The loads that were applied in the different investigations are given in Table 6.3.

Table 6.3. Overview of used indentation loads [N] and microscopy techniques for different investigations.

Sample	SCCG Measurement		Overall and crack tip COD	Hardness and crack length estimation	Crack shape analysis
	Overall *COD	ICL			
Soda- lime glass	49.05	9.81, 49.05	9.8, 29.4, 49.0, 78.5, 98.1	0.24, 0.49, 0.981, 1.962, 2.94 4.90, 9.81, 19.62, 29.24, 39.24, 49.05	49.05
Borosilicate glass	49.05	9.81, 49.05	9.8, 29.4, 49.0	0.24, 0.49, 0.981, 1.962, 2.94 4.90, 9.81, 19.62, 29.24, 39.24, 49.05	49.05
SiCN-800		19.62	19.62, 24.52	0.24, 0.49, 0.981, 1.962, 2.94 4.90, 9.81, 19.62, 24.52	24.52
SiCN-900		29.4	29.4	0.24, 0.49, 0.981, 1.962, 2.94 4.90, 9.81, 29.4	29.4
SiCN-1000		39.24	29.4, 39.24, 49.05	0.24, 0.49, 0.981, 1.962, 2.94 4.90, 9.81, 29.4, 39.24, 49.05	39.24
SiCN-1100		39.24	29.4, 39.24, 49.05	0.24, 0.49, 0.981, 1.962, 2.94 4.90, 9.81, 29.4, 39.24, 49.05	39.24
Microscopy	HRSEM	OM	AFM	OM	OM; HRSEM

SCCG-subcritical crack growth; ICL-indentation crack length measurement; COD-crack opening displacement; HRSEM-high resolution scanning electron microscopy; AFM-atomic force microscopy; OM-optical microscopy. "Overall" denotes measurement along the complete crack.

Indentations were made in the middle of samples to avoid any influence from residual stress induced by the cutting process. Moreover, a distance of approximately 3.5 times the crack length was kept between the indentations in order to avoid a mutual influence of the residual stresses induced by indentation (Figure 6.4).

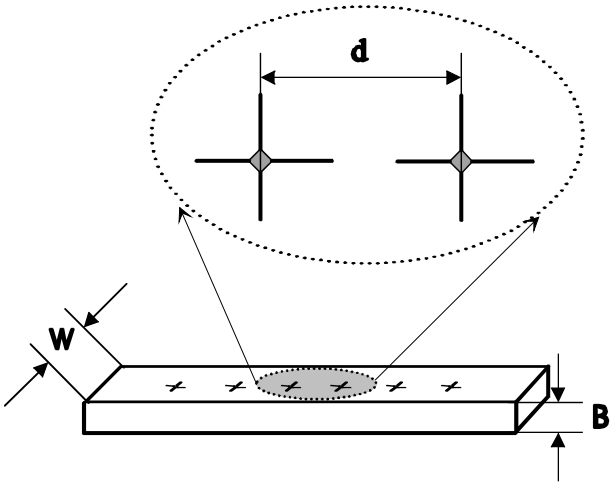

Figure 6.4. Schematic drawing of a sample with indentations made in the middle; W is the width, B the thickness, and d the distance between two indentations.

6.5. Measurement of crack length and indentation impression size

Measurement of the crack length and the indentation impression size was performed with a Leitz DMRM optical microscope (Leica, Bensheim, Germany). For the investigation of subcritical crack growth, measurements were made after different periods of time in laboratory environment. For determination of the crack length as a function of applied load and hardness, measurements of crack length and indentation impression size were been done immediately after indentation to reduce the influence of subcritical crack growth especially for glasses.

6.6. Measurement of the crack opening

6.6.1. Principle of atomic force microscopy (AFM)

To investigate the crack profiles, an atomic force microscope was used which proved to be an excellent tool for high precision measurements of the crack opening due to its high spatial resolution. Atomic force microscopy (AFM) is a relatively new microscopy technique often used for topographic investigations. It can be used to study almost any samples, including insulators and semiconductors as well as electrical conductors. A significant difference between AFM and scanning electron microscopy for imaging surface topography is that the AFM gives a quantitative surface profile.

Figure 6.5. Image of the Digital Instruments Nanoscope IIIa scanner with attached head that holds the AFM tip. The operation mechanism consists of scanning the sample below the tip which is at fixed position.

The principle of the AFM relies on the use of a sharp tip to probe the sample surface. The tip is mounted on a cantilever (100-200 μm in length) which is brought into close proximity to the surface where intermolecular forces acting between the tip and the surface cause the

cantilever to bend. A piezoelectric crystal positioner is used in order to position the sample accurately, with the tip held at a fixed position (Figure 6.5). Depending on the scanner type (piezo tube length) the maximum scan sizes vary between ca. 1 μm and several hundred micrometers. Today, most AFMs use a laser beam deflection system, where laser light is reflected from the back of the reflective AFM lever and onto a position-sensitive detector (Figure 6.6). The measured cantilever deflections allow a computer to generate a map of the surface topography. The data, (*i.e.* topography (height)), can be displayed graphically using a colour scale to indicate the height of each point observed.

AFM tips and cantilevers are usually microfabricated from Si or Si_3N_4. AFM tips often have the shape of a pyramid, with a radius of curvature at the apex between a few and tens of nanometers. It is important to emphasise that the true resolution for imaging is limited by the shape and the radius of the tip.

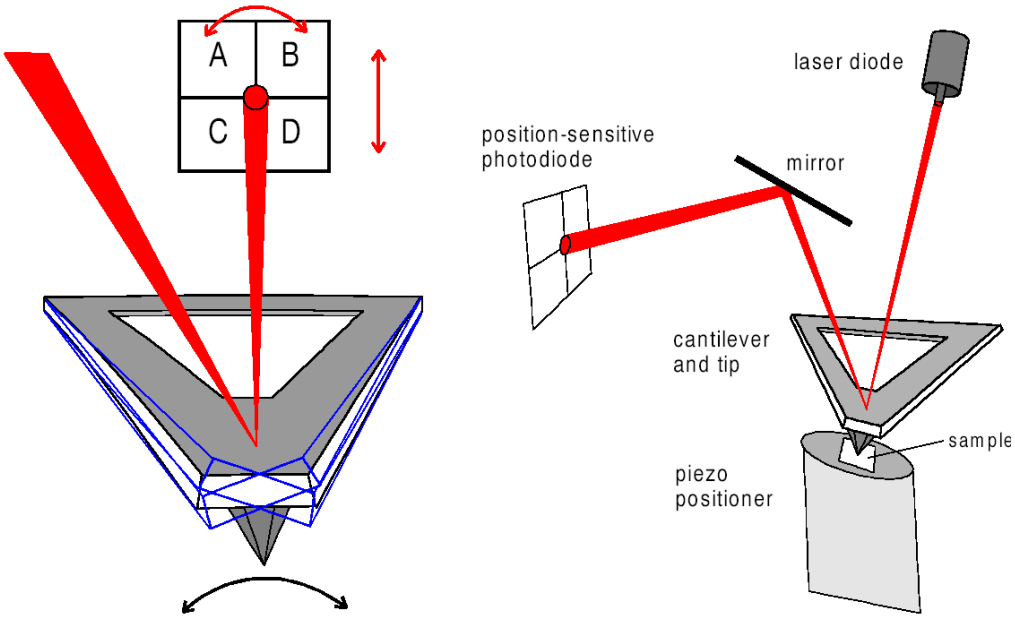

Figure 6.6. Bending of the cantilever and corresponding displacement of the deflected laser beam (left); schematic diagram of the laser deflection system used to detect bending of the cantilever (right).

A number of different AFM modes of operation have been developed in recent years. In the simplest case, the tip is brought in direct contact with the surface (contact mode). One disadvantage of this mode is that considerable forces are exerted on the sample, which may cause partial destruction of surface features. This drawback has been circumvented by the tapping mode, which uses a relatively stiff cantilever. It operates by oscillating the cantilever at or near its resonance frequency with an amplitude ranging typically from 20 nm to 100 nm. When the cantilever is vibrating far away from the sample surface in air, the vibration is

damped only by the molecules in the gas. Close to a sample surface, in contrast, the vibration gets further damped. The original amplitude A_0 is reduced to A depending on the distance to the surface. A feedback loop keeps a certain amplitude damping constant, typically 90% of A_0. Such high A/A_0 ratio is chosen in order to keep the contact time and peak forces during one cycle of oscillation to a minimum. Thus the tip only lightly "taps" on the sample surface. A change in the phase difference between exciting voltage and vibration of the cantilever can be used to obtain contrast due to different surface characteristics related to materials properties (tapping mode AFM phase imaging).

6.6.2. COD measurement

The measurements of crack opening were conducted in a laboratory environment using a Nanoscope IIIa AFM (Digital Instruments, Veeco Metrology Group, Santa Barbara, California, USA) in tapping mode. Since a very low scan rate of 0.5 Hz per line had to be used, the AFM scans were time consuming (about 20 min per image). Moreover, the complicated repositioning of the tip to the next location along the crack usually required several trials. As a consequence, the full investigation of one crack took several days. Therefore the indented samples were kept for two days in laboratory atmosphere before measurement. This period of time was found to be sufficient to allow for subcritical growth, such that a "stable" configuration is reached [85Law, 95Sgl]. Prior to the actual measurements, a calibration of the AFM was carried out by using a reference grid.

For measuring the overall crack opening of glasses, standard Si cantilevers with ~15 nm tip radius were used to scan the sample areas of 10x10 μm^2 and 5x5 μm^2. Displacements at positions close to the crack tip were measured to higher accuracy over surface areas of 3 x 3 μm^2 using much sharper super-cone tips (tip length 9 µm / 5-10 nm tip radius). For polymer derived ceramics, due to their short crack lengths of ~30 µm and small opening (max 250 nm), exclusively super cone cantilevers have been used, with scan areas of 3x3 μm^2, 1.5x1.5 μm^2 and 1x1μm^2.

A typical topographic AFM image of a crack is displayed in Figure 6.7a. The crack can be identified by a very dark contrast, which is due to the very deep position of the tip, with respect to the sample surface. The crack opening can be determined from the height profile across the crack at a desired position, as exemplarily shown in Figure 6.7b, with the position of the crack edges taken as the point where the cantilever tip just leaves the surface plane. As a result of the finite tip size, the shape of the height profile appears rounded (Figure 6.8), which leads to an uncertainty in the measured crack opening of the order of the tip radius.

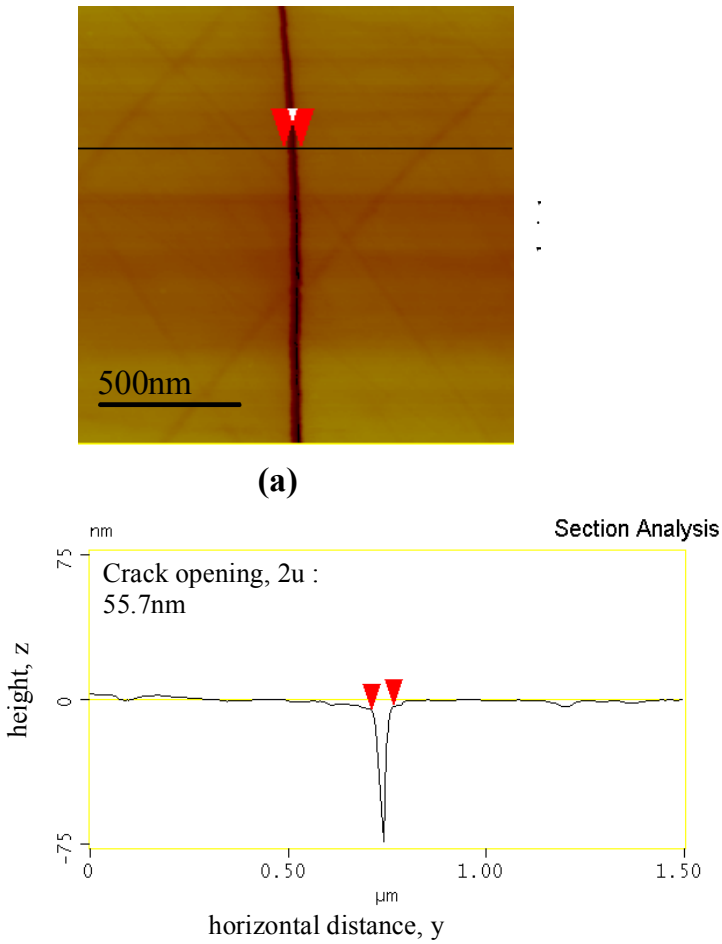

Figure 6.7. Topographical AFM image of a crack (a); the corresponding height profile of a scan across the crack from measuring the crack opening (b).

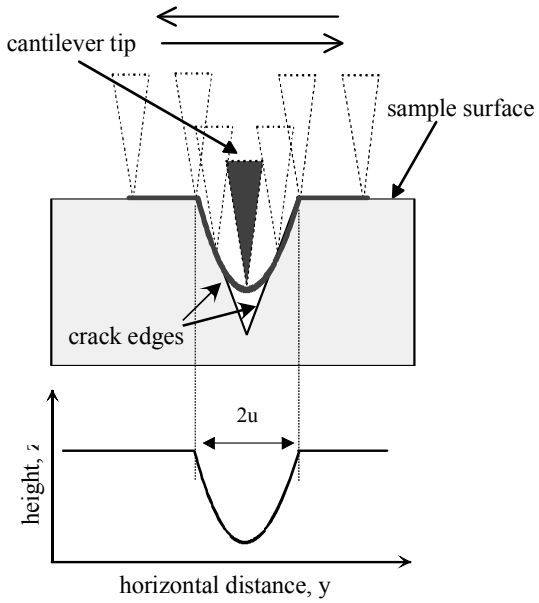

Figure 6.8. Schematic of an AFM tip scanning across a crack within the indentation specimen (top), and corresponding height scan of the tip as a function of the tip position along the scan trail (bottom)

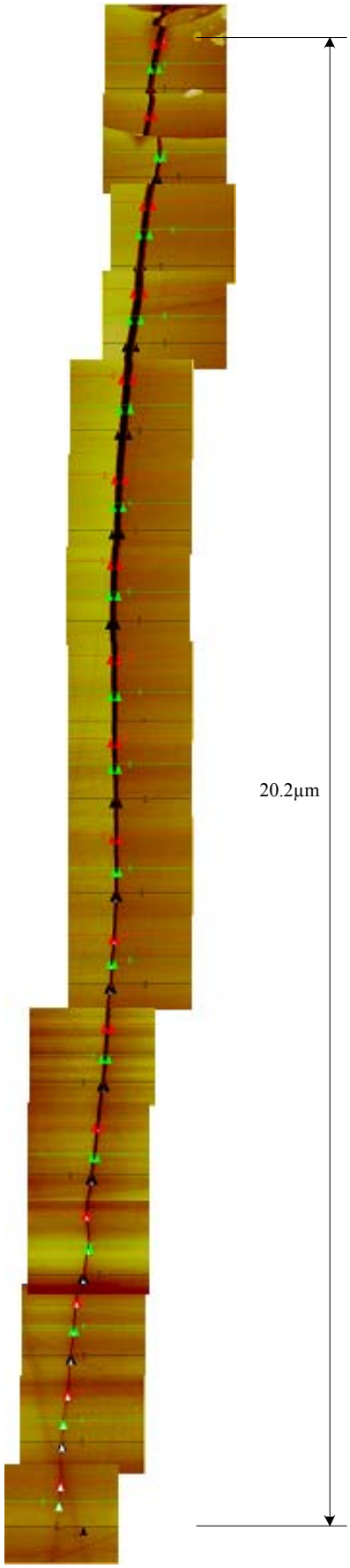

Figure 6.9. Full crack geometry displayed by an appropriately arranged set of individual AFM images.

6.6.3. High resolution scanning electron microscopy

A high resolution scanning electron microscope (DSM 982 Gemini, Zeiss, Oberkochen, Germany) was used to investigate the influence of subcritical crack growth on crack opening in glasses. Electron microscopy was used for this purpose because it allows for fast measurements under vacuum. This is in contrast to atomic force microscopy, which could be performed only in air, and which requires long measuring times.

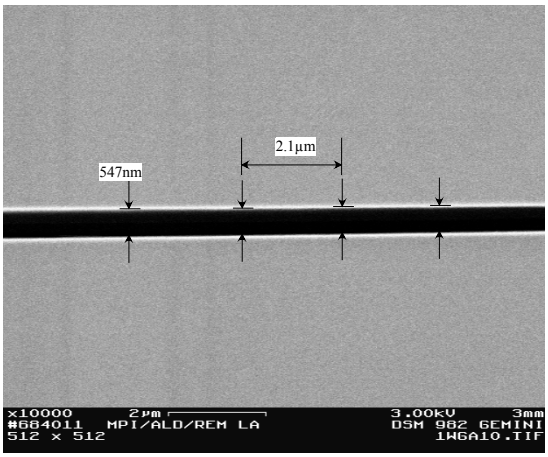

Figure 6.10. Electron micrograph of part of the crack within a glass substrate.

Electron microscopic investigations were performed immediately after indentation, after 2 days, and after 10 days. Between these measurements, the samples were stored in laboratory atmosphere. The samples were sputtered with a very thin film (few nm thickness) of $Pt_{80}Pd_{20}$ alloy. The opening displacements were taken visually from the micrographs. The edges of the crack faces are not perfectly defined due to deposited carbon contaminations and the sputtered metal (Figure 6.10). To achieve as high reproducibility as possible, in all micrographs the border line between the inner dark region and the white edge region was defined as crack edge position. To investigate the crack opening along the entire crack the same image assembling procedure as in the AFM investigation was used.

6.7. Investigation of crack shape beneath the indentation

In order to examine the crack shape, indentation was performed in the middle of bend bars, which were broken several minutes later by using three point bending tests, as shown in Figure 6.11. Geometry and dimension of the samples were identical to those in the previous investigations.

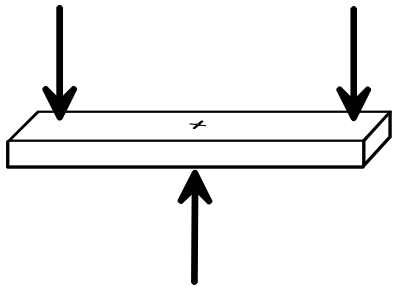

Figure 6.11. Schematic representation of bending tests performed to investigate the crack shape underneath the indent.

The fracture surface was investigated by scanning electron microscopy.

7. Results and discussion

7.1. Deformation - fracture morphology

7.1.1. Normal and anomalous glass

The material-specific behaviour under indentation is reflected in the central contact impression and surface traces of the two orthogonal crack systems. The indentation surface damage in the two reference glasses is compared in Figure 7.1 for an applied load of 49 N. This load represents the highest load that could be used for borosilicate glass without occurrence of chipping. Some of the features observed in the present samples had been noticed before in other studies [79Aro, 82Ish, 83Law]. In the following, the main differences between the normal and anomalous contact stress behaviour will be summarised.

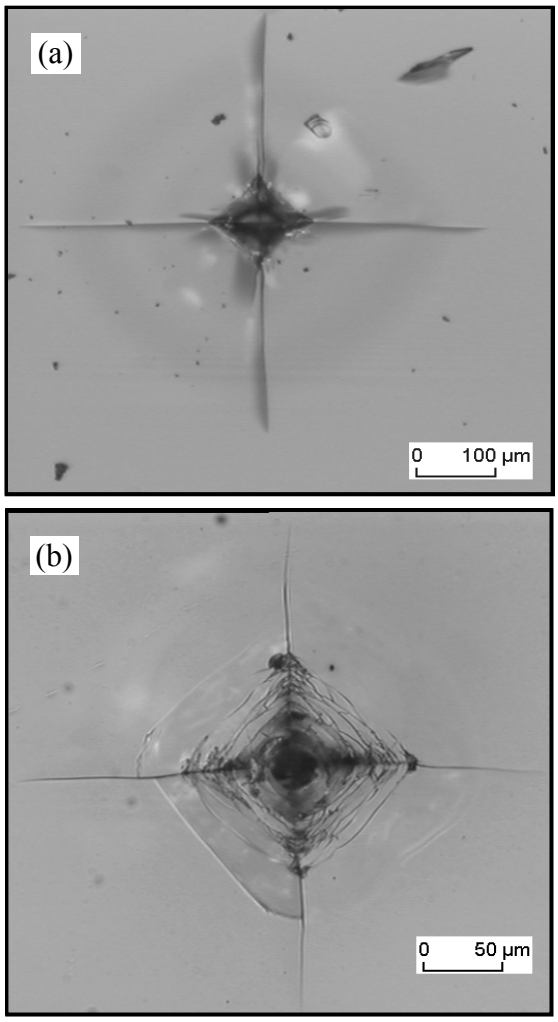

Figure 7.1. Optical micrographs of the indentation impression with the associated radial crack system in soda lime (a) and borosilicate (b), in each case resulting from Vickers indentation with 49 N load. Note different magnification in two images.

As apparent from the optical micrograph in Figure 7.1a, the soda lime glass exhibits a well-defined, impression of the indenter shape, characteristic for normal behaviour. For borosilicate glass, in contrast, one observes a multitude of microcracks within the region of the impression as a typical signature of anomalous behaviour (Figure 7.1b).

The homogeneous appearance in the case of soda lime glass is due to the modification of the glass structure, which leads to volume conservation of the deformation underneath the indent [79Hag]. This results in a shear fault pattern with very small spacing [81Lat] that is unresolved by the optical microscope. In borosilicate glass, in contrast, there is a high surface

roughness originating from the presence of a smaller number of shear faults, parallel to the edges of the indentation impression, with relatively large separation.

Despite the obvious differences in the "plastic" deformation patterns, the two glasses show essentially the same tendency for radial cracking from shear faults at or near the indentation diagonal. However, it is evident that soda lime glass shows longer radial cracks relative to the indentation impression size than borosilicate glass. This difference is related to the higher residual stress present in normal glasses [79Aro].

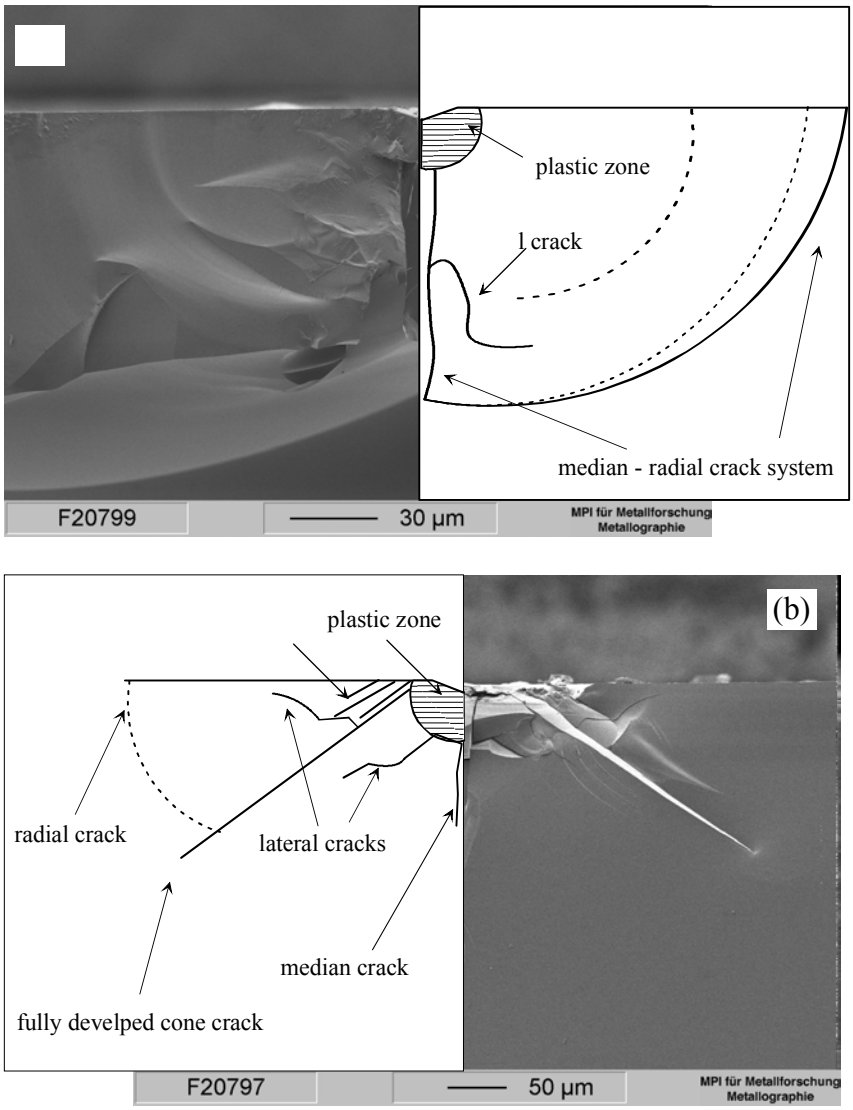

Figure 7.2. Scanning electron micrographs of the fracture surface of specimens broken at the indentation sites, combined with a schematic view of the crack systems. Indentation was performed by applying a load of 49 N to soda-lime (a) and borosilicate (b) glass.

A further difference is seen from the fracture subsurface beneath the indent (Figure 7.2). Specifically, soda lime glass shows a well-developed semi-circular (half penny shaped) radial-median crack system together with a lateral crack (Figure 7.2a). On the other hand, borosilicate glass exhibits a well-developed cone crack (Figure 7.2b). In this case, the lateral,

median and radial cracks are also developed but only to a small extent due to the restriction exerted by the cone crack.

The normal behaviour of soda lime glass, reflected in volume conserving deformation, can be explained by the presence of a network modifier (soda, Na_2O) that provides weak points (non-bridging oxygen atoms, see Figure 6.1a) for flow and formation of the shear faults, while at the same time the modifier fills the interstices and reduces the compressibility. The anomalous behaviour of borosilicate glasses is a result of the more "open" structure of the three-dimensionally coordinated boron-doped silica which lends itself to densification [68Ern]. There is evidence that permanent impressions go along with glass mass displacement downward, which leads to an increase in glass density associated with changes in the O-Si-O and Si-O-Si bond angles as well as the Si-O bond length [00Zie]. The formation of well-separated shear faults in borosilicate glass is a consequence of the small but non-zero sodium ion content (see Table 6.1).

7.1.2. Polymer-derived amorphous SiCN ceramics

Examination of the indents in the polymer-derived amorphous SiCN ceramics revealed a certain load threshold for radial crack formation around the indentation impression. This load was found to be ~20 N, depending only weakly on the pyrolysis temperature. For smaller applied loads, only a perfect indentation impression with no visible radial cracks is obtained, as exemplified in Figure 7.3. The threshold of ~20 N is considerably higher than observed for the glasses, where it is 2.9 N for borosilicate glass and 0.9 N in window glass. On the another hand, the maximally applicable load was found to vary between different polymer-derived SiCN samples. For SiCN-800, loads above 24.5 N lead to chipping at the surface (Figure 7.4), and not all of the four orthogonal radial cracks are formed. The same effect was observed for SiCN-900 with loads above of 29.4 N. Furthermore, in the case of SiCN-1000 and SiCN-1100, loads of maximally 49 N were applied to avoid the formation of radial cracks that extend over the whole width of

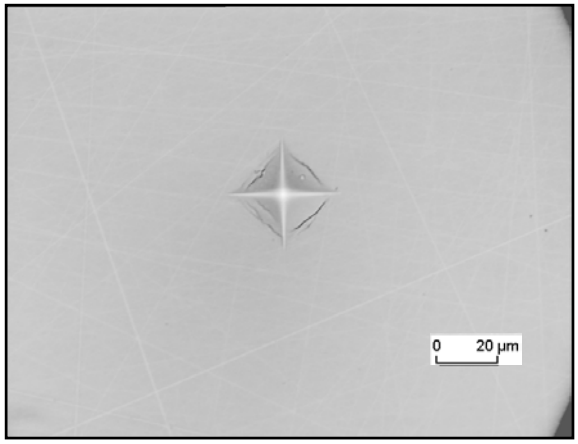

Figure 7.3. Optical micrograph of a well-shaped indentation impression produced in SiCN-1000 by Vickers indenter with an applied load of 9.8 N.

the sample. This load was not sufficient to cause chipping which is however, likely to occur under higher loads.

Typical surface views of indentations with loads above the crack generation threshold, presented in Figure 7.5, reveal the classical "anomalous" crack pattern with small radial crack lengths relative to the indentation impression size, and a small number of clearly visible shear-faults. Moreover, in all cases, circular cracks are clearly seen in the center of the indents. Their formation, which is usually observed when blunt indenters are used, provides a hint that the sharp indenters employed in the present studies get blunted due to densification that occurs

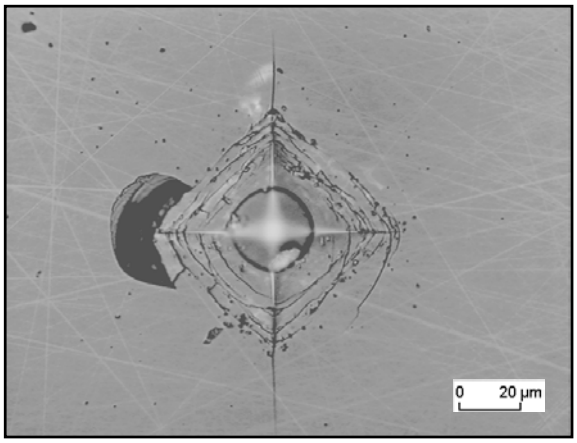

Figure 7.4. Optical micrograph of "chipping" around an indent in SiCN-800 produced by an applied load of 29.4 N with Vickers indenter.

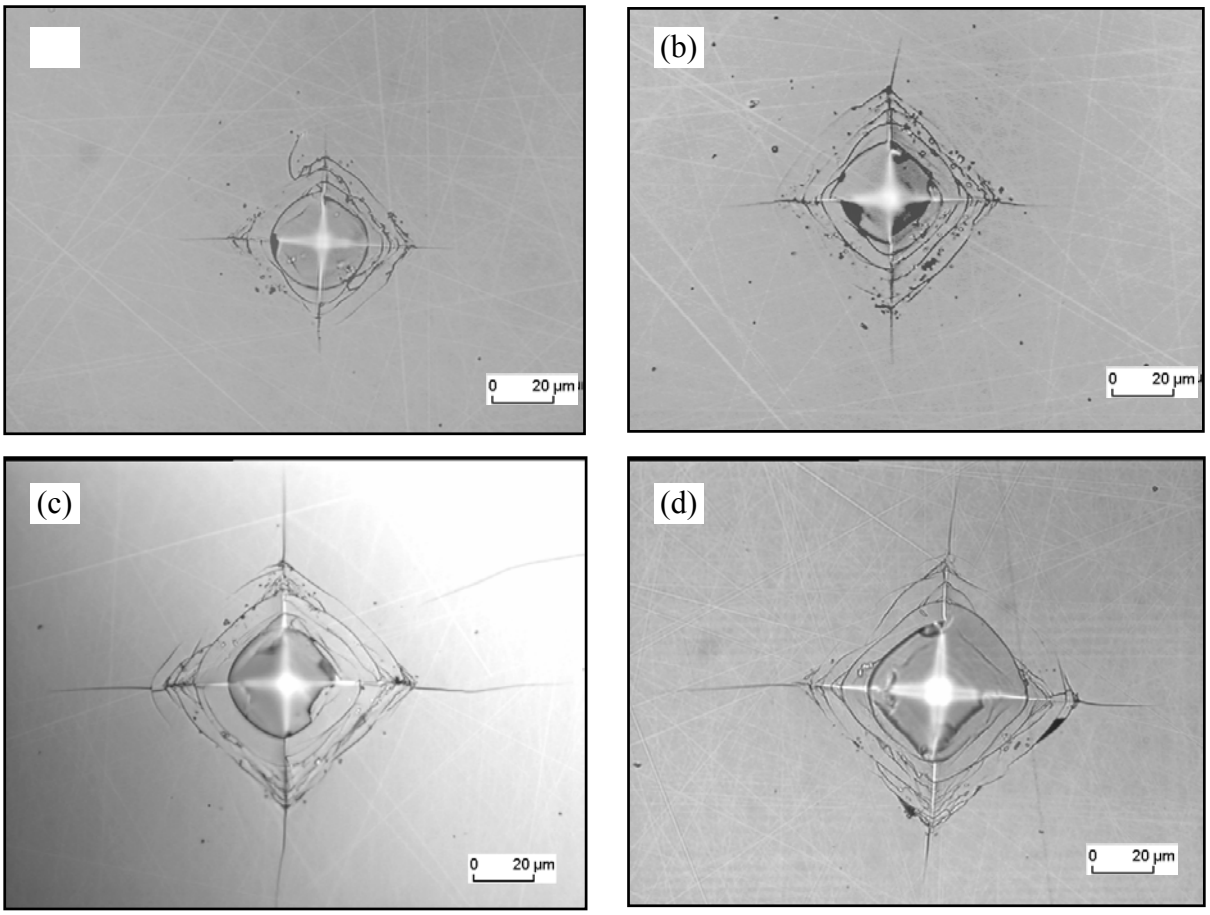

Figure 7.5. Optical micrographs of indents with associated radial crack system in SiCN-800 (a); SiCN-900 (b); SiCN-1000 (c) and SiCN-1100 (d) produced by applied loads of 24.5 N, 29.4 N, 39.2 N, 49.02 N, respectively with Vickers indenter.

upon indentation.

The indentation shape in polymer derived amorphous SiCN ceramics more closely resembles that of the borosilicate than that of the soda lime glass. However, the relative length of the radial cracks is even shorter than in the borosilicate glass. In addition, the separation of the shear faults is larger in the amorphous ceramics. Considering that shear faults are created at the weak positions in the structure [79Hag] (like non-bridging oxygen in soda lime glass), the latter observation can be taken as evidence for stronger covalent bonding in the precursor derived amorphous ceramic materials, from which a larger extent of densification could be expected.

Although the crack morphologies in Figure 7.5. were obtained with different loads, their comparison reveals that with increasing pyrolysis temperature less pronounced ring crack formation takes place, and somewhat longer (relative to the indent size) radial cracks are formed (Figure 7.5d). This result suggests that the degree of densification of the indented material (and consequently blunting of indenter) slightly decreases with increasing pyrolysis temperature.

The circular cracks at the surface of the amorphous ceramics indicate a tendency towards formation of cone cracks, which are characteristic of blunt indentation. One example of such cone crack formation observed on the fracture surface is given by Figure 7.6, which shows the

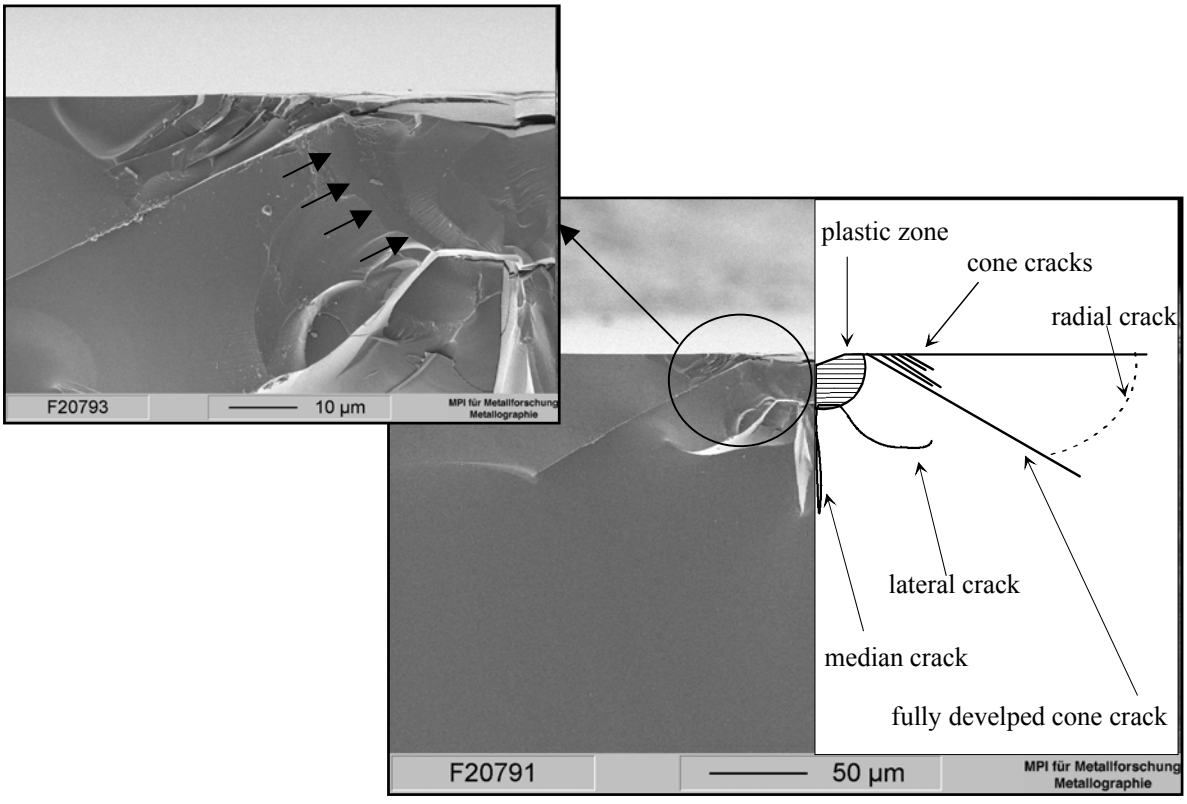

Figure 7.6. Scanning electron micrograph of the fracture surface of polymer derived SiCN-1000 specimen broken at the indentation site, combined with half-schematic view of the crack system. Vickers indentation was performed by applying a load of 39.2 N.

crack system in a SiCN–1000 specimen.

It can be seen that the cone crack separates the median and radial cracks (the shape of the latter is difficult to see), indicating that these cracks grew independently. In addition, the cone crack restricts the development of the radial and median cracks because of its earlier initiation [86Cha]. The samples also show a well-developed lateral crack system. Moreover, the fracture surface micrograph reveals a deformation region (plastic zone, compare 6.2.1.2) of hemispherical shape, located underneath the indenter impression (marked by the arrows in Figure 7.6). In addition to the fully developed cone crack, a series of partially developed cone cracks are visible close to the surface.

To demonstrate that the above described features are a general characteristic of the crack system in the polymer-derived amorphous SiCN ceramic, the fracture surface of three additional specimens is displayed in Figure 7.7. The plastic zone of hemispherical shape, located just beneath the indenter, is seen to be associated with well-developed cone and lateral cracks. Median and radial cracks are also developed, but they do not appear to be very

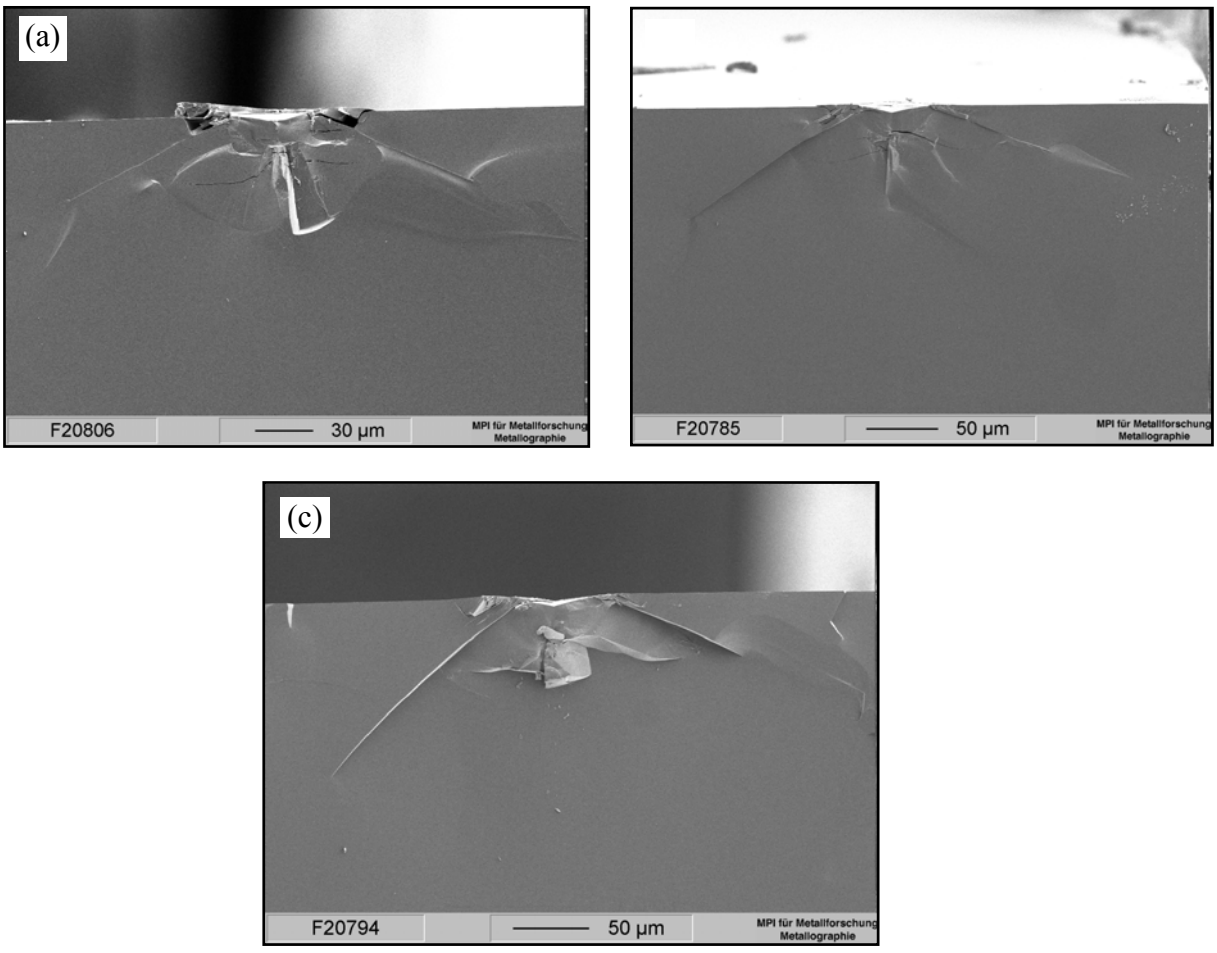

Figure.7.7. Scanning electron micrographs of the fracture surface of the indentation crack system in a SiCN-800 (a), SiCN-900 (b) and SiCN-1100 (c) sample, produced by applying a respective load of 24.5 N, 29.4 N, and 39.2 N with a Vickers indenter.

pronounced due to the restriction exerted by the cone crack.

Despite the increasingly higher applied loads, the size of the deformation zone is found to be similar in all samples.

Pressure induced densification can involve a phase change (crystallization) or compaction of "open" microstructures [75Law]. In order to clarify whether crystallization occurs beneath indentations, a part of the deformation zone was prepared out from the samples to enable investigation by transmission electron microscopy. In this process, a focused ion beam (FIB) method was used for high precision cutting of the desired region.

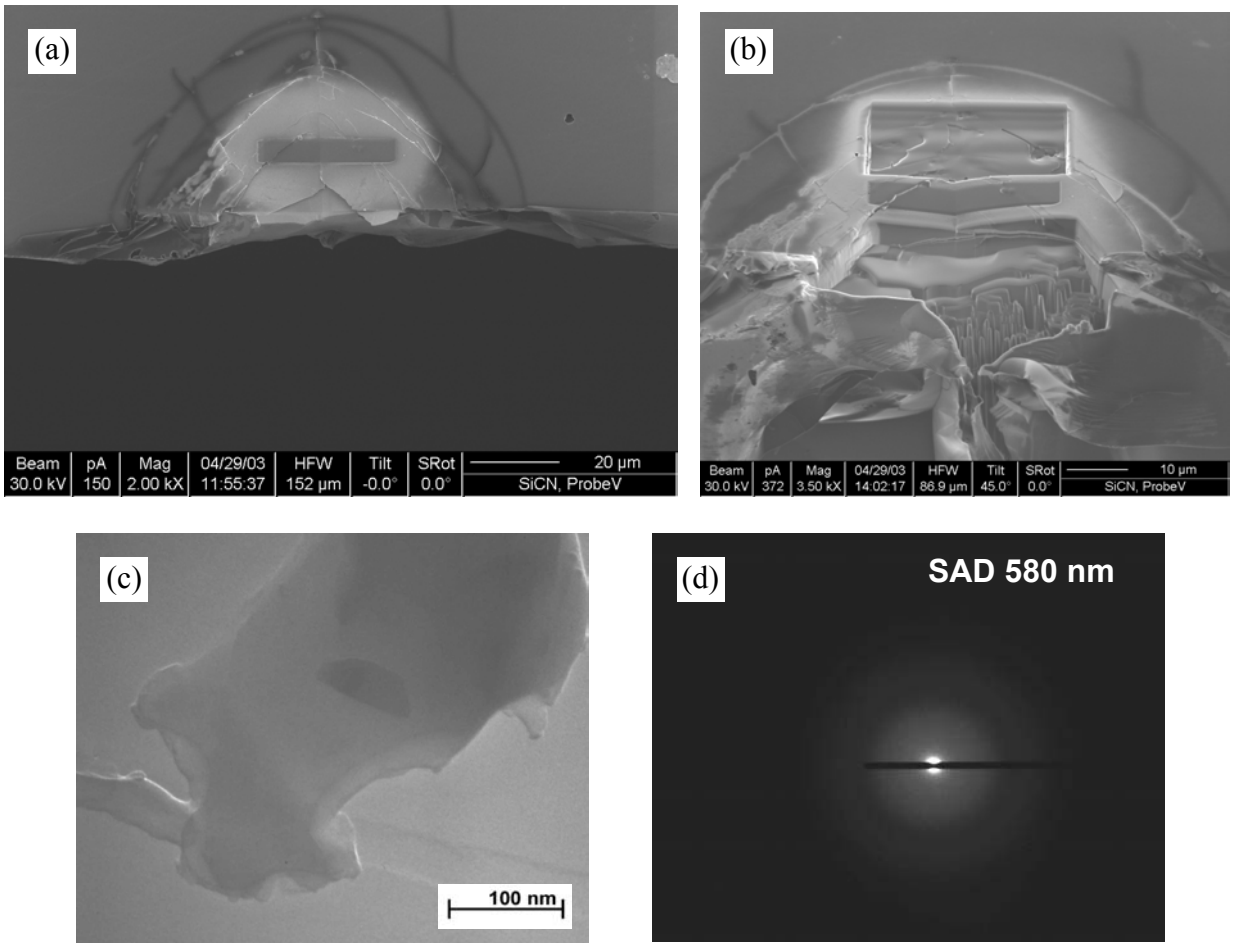

Figure 7.8. Scanning electron micrograph of half of the indent in a polymer-derived amorphous SiCN-1000 ceramic specimen in top view (a); this specimen was indented with a load of 39.2 N. Micrograph of the region from which the slices were cut for subsequent analysis by transmission electron microscopy (b). Transmission electron micrograph of thin section taken from the deformation zone of the sample (c). Transmission electron diffraction pattern recorded within the deformation zone (d).

A top view of half of the indenter impression is given in Figure 7.8a, where the region from which the slices have been taken appears bright. Figure 7.8b shows a close-up image after cutting of the slides, which were of non-uniform shape, as can be seen from Figure 7.8c. The irregular shape results from the high stress within the deformation zone, which complicates the cutting by FIB. Nevertheless, the quality of the obtained part was sufficient for

subsequent analysis by transmission electron microscopy. The major result is the absence of discrete diffraction spots or rings in Figure 7.8d, from which it is concluded that the material contained in the deformation zone is amorphous, *i.e.* no crystallisation has occurred. It consequently follows that pressure-induced densification is due to compaction of the "open" microstructure or free volume.

The amorphous SiCN ceramics clearly reveal anomalous indentation behaviour. This is apparent from the following characteristics, all of which are also observed for borosilicate glass:

- a small number of shear faults;
- formation of short radial cracks;
- circular crack formation in the center of indent;
- tendency for cone crack formation.

These features result from the fact that the structures of both, polymer-derived amorphous ceramics and borosilicate glass, allows for densification under the indentation load. In borosilicate glass, this property has been related to the possibility to compact the spatial arrangement of the Si-O tetrahedra. A similar compaction leads to anomalous behaviour in case of threefold coordination, such as in B_2O_3 networks [82Ish]. In the amorphous ceramics, densification can occur due to the "open" structure of the amorphous Si-C-N network. The existence of such free volume has been revealed by molecular dynamics simulations of the atomic structure, as illustrated by the structure model in Figure 7.9. In analogy to observations made on anomalous glasses [68Ern], it is expected that the Si-C or Si-N bond angles can be changed under applied load.

In view of these similarities between amorphous ceramics and borosilicate

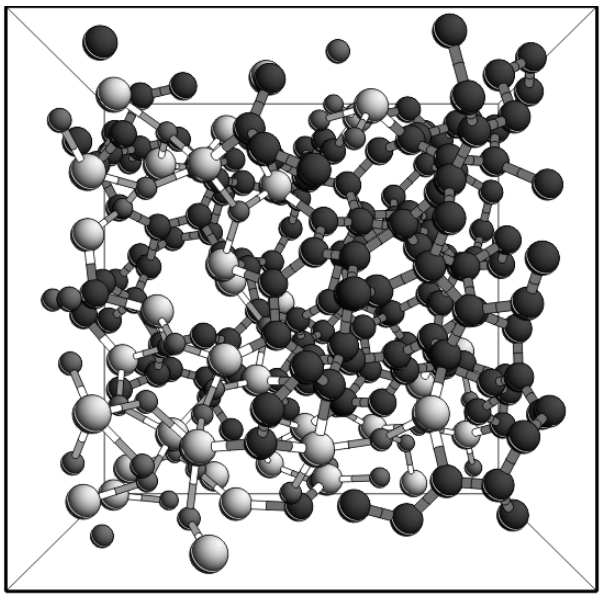

Figure 7.9. 3D figure of modelled simulation of atomic structure of amorphous polymer-derived SiCN ceramics [03Res]. The large light atoms are Si, the small grey atoms are N, and the medium sized dark atoms are C.

glass, a suitable means was sought to quantitatively compare the extent to which these two materials behave anomalously under indentation. The cone angles measured (from the scanning electron micrographs) in the different amorphous SiCN ceramics are compared in Table 7.1 with those observed in borosilicate glass and fused silica glass. The latter glass is included since it experiences very strong densification, and therefore represents the extreme case of anomalous behaviour [93Law]. This is reflected in the significantly smaller cone angle (~22°), as compared to that in borosilicate (~35°), which can be explained by the presence of sodium ions (4 wt%) acting as a structure stabiliser in the latter glass. It is an important observation that the cone angles in the amorphous SiCN ceramics (~23 - 31°) fall between those of the two glasses. Taking the cone angle as a measure for anomalous behaviour, it is thus concluded that the amorphous SiCN ceramics behave more anomalous than borosilicate but less than fused silica glass. It follows that stronger densification occurs in the polymer-derived amorphous SiCN ceramics than in borosilicate glass. Moreover, this result is in accordance with the fact that the threshold for radial crack formation in polymer-derived amorphous SiCN ceramics (9.8 N) is higher than in borosilicate glass (2.9N).

Table 7.1. Measured cone angles and densities for the investigated amorphous ceramics, in comparison with two types of anomalous glasses.

	Fused silica glass[93Law]	SiCN-800	SiCN-900	SiCN-1000	SiCN-1100	glass
Density,ρ ,g/cm^3	2.2	1,85	1,90	2,00	2,10	2.23
Cone angle, °	22	23	26	28	31	35

Furthermore, when the pyrolysis temperature is increased, the indentation fracture behaviour of the SiCN amorphous ceramics is observed to approach that of borosilicate glass, as apparent from the increase in cone angle. This trend towards less anomalous behaviour can be understood from the structural changes that are expected in the amorphous ceramic network upon increasing the pyrolysis temperature. Under these conditions, organic residues (methane and hydrogen) are released [95Bil], which leads to shrinking of the available free volume and consequently a smaller ability to densify. Evidence that these changes occur is gained from the observed increase in the density of the samples [03Jan] (Tabele 7.1). However, it should be emphasised that the load required for crack formation would also be decreased for such type of samples.

7.2. Overall crack opening profiles

7.2.1. Normal and anomalous glass

The crack opening profiles of radial indentation cracks in soda lime and borosilicate glass are displayed in Figure 7.10. While for soda lime glass a maximum indentation load of 98.1 N could be applied, the load was limited to a maximum of 49.0 N in the case of borosilicate glass to prevent chipping. The radial coordinate, r, corresponds to the distance from the indent center. For both glasses and all loads, the shape of the profiles in the range (r>a) is concave upward, except in close vicinity of the crack tip. This behaviour is consistent with a centrally-loaded crack [80Law]. The maximum crack opening is observed at the distance that corresponds to the vicinity of the indent corner (r=a), and is smaller in borosilicate glass than in soda lime glass for the same indentation load. The measured values for the indent size, a, are given in Table 7.2. In soda lime glass, the crack opening decreases gradually with increasing distance from the indent corner (r>a), while in borosilicate a rather steep decrease of the crack opening is observed due to the comparatively short crack length. Upon approaching the indent center (r<a), on the other hand, both glasses show a similarly steep decrease of the crack opening. It is noted that especially in borosilicate glass, measurements of the crack opening inside the indent are

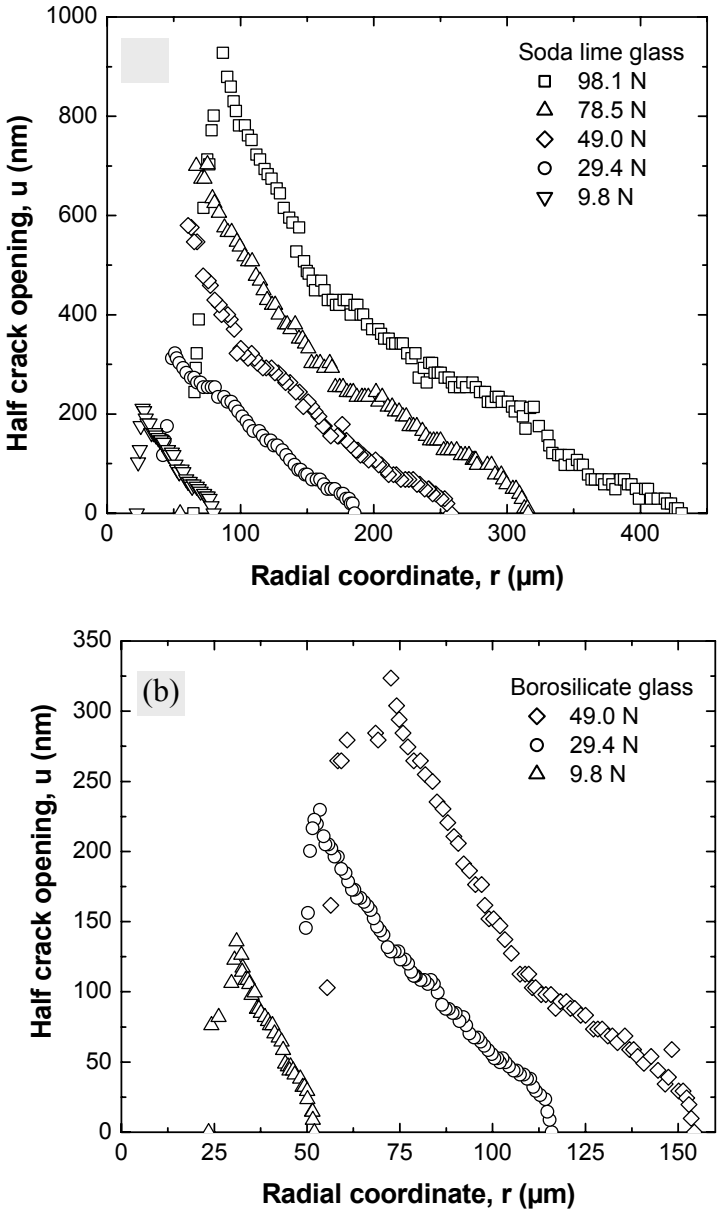

Figure 7.10. Crack opening profiles of radial indentation cracks of soda lime (a) and borosilicate (b) glass measured by AFM.

difficult to perform due to the crack distortions associated with the pronounced shear faults, which allow reliable measurements only at certain locations (Figure 7.11). In addition, the high surface roughness increases the risk of cantilever damage.

For both glasses, the crack profile depends strongly on the indentation load, as reflected in the increase of both the maximal crack opening and crack length with increasing load. Moreover, the ratio c/a between crack length and indent size rises with applied load (Table 7.2), and for a given load it is smaller for borosilicate glass.

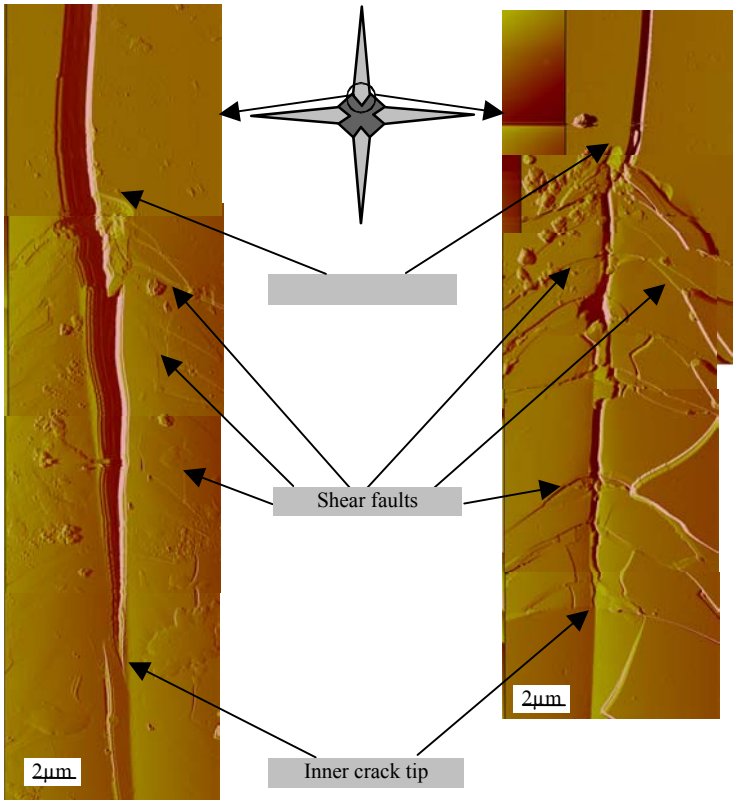

Figure 7.11. Overlapped AFM images of the crack opening for radial dentation cracks inside the indent (r<a); left soda lime and right borosilicate glass. Note the smaller distance of shear faults in soda lime glass.

Table 7.2 Measured values of the relevant geometrical parameters of the radial crack system of Vickers indents in glasses obtained with different applied loads; $\mathbf{c_1}$ is the position of the inner "crack tip" measured from the indent center, **c** is the crack length, and **a** the half diagonal of the indent.

Load (N)	Soda lime glass					Borosilicate glass				
	c_1 (µm)	c_1 (µm)*	a (µm)	c (µm)	c/a	c_1 (µm)	c_1 (µm)*	a (µm)	c (µm)	c/a
9.8	22.2	22.4	26.5	80	3.0	23.5	26.1	30.9	52	1.7
29.4	36.5	35.0	48.0	185	3.8	49.7	49.5	58.5	116	2.0
49.0	52.0	51.3	60.7	258	4.2	55.5	53.0	62.6	154	2.5
78.5	54.7	61.6	72.8	316	4.3					
98.1	64.7	76.2	90.0	431	4.8					

*c_1 (µm) values calculated according to Hill expanding cavity model[98Hil]

The values measured for the inner crack tip position, c_1, are in good agreement with those calculated according to Hill's expanding cavity model of the deformation zone (Table 7.2), which predicts that hoop residual stresses remain tensile within the radial region for distances larger than exp(-1/6)a=0,846a [98Hill]. This finding combined with the fact that the present cracks are of the centrally loaded type provides the basis for calculating the residual stress distribution within the framework of this model (see section 7.3).

That the maximum crack opening is measured in the vicinity of the indent corner goes back to the fact that the residual stress produced by indentation, which acts a primary driving force for the crack opening as well as its propagation, reaches its maximum in this area due to the mismatch region between the elastic and plastic field. The smaller maximal crack opening in the borosilicate glass compared to that of soda lime glass for all applied loads indicates a lower residual stress in the former glass. This conclusion is further supported by the smaller crack length as well as smaller c/a ratio in the borosilicate. The low residual stress in borosilicate glasses originates from its partial consumption by the densification process (compare section 7.1.1) during indentation as a characteristic of anomalous indentation behaviour.

7.2.2. Polymer-derived amorphous SiCN ceramics

The crack opening profiles of the radial indentation cracks in the polymer-derived amorphous SiCN ceramic materials are presented in Figure 7.12. To avoid chipping, the loads for SiCN-800 and SiCN-900 are limited to maximum of 24.5 N and 29.4 N, respectively. It is apparent that the general shape of the crack opening profiles is independent of load for each material. Similar to the soda lime and borosilicate glasses, the crack opening reaches a maximum in the vicinity of the indent corner, from where it decreases rapidly with increasing distance, resulting in short cracks with a steep profile. As a consequence, the shape of the crack opening profiles is only slightly concave, in contrast to the pronouncedly concave curves obtained for the other glasses (Figure 7.10).

At a given indentation load, the maximal crack opening as well as crack length are found to increase with pyrolysis temperature.

The plots in Figure 7.12 contain only the declining component, as the crack opening could be measured only outside of the indent (r>a). The reason for this limitation is that the position of the inner crack tip falls within the region of the ring cracks, which is clearly visible from

Figure 7.13. Accordingly, the measurements of the crack opening were performed up to the indent corner where the largest opening exists. Since for the glasses good agreement between the measured and calculated values for the inner crack tip position, c_1, has been obtained (Table 7.2), Hill's expanding cavity model of the deformation zone [98Hill] was used to estimate the inner crack position in case of the polymer-derived amorphous SiCN ceramics. The obtained values are included in Table 7.3.

As a further similarity to the soda lime and borosilicate glasses, the maximal crack opening increases with applied load in all four amorphous SiCN ceramics. The same trend is observed for the crack length and the c/a ratio (Table 7.3).

In contrast to the aforementioned regular dependencies on load, the crack length and c/a ratio at a fixed load do not show a continuous increase with pyrolysis temperature.

The relatively small maximum opening as well as the short crack

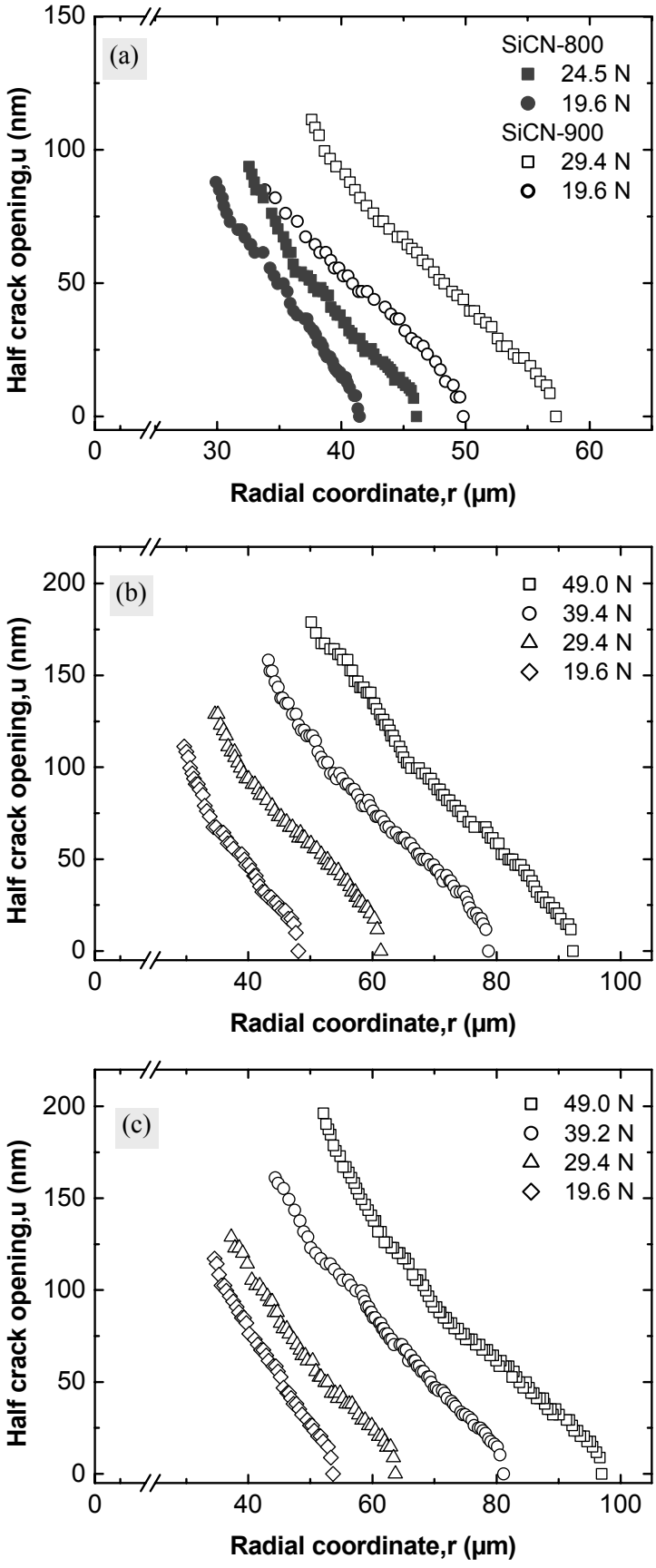

Figure 7.12. Crack opening profiles of radial indentation cracks of polymer derived SiCN-800 and SiCN-900 (a); SiCN-1000 (b) and SiCN-1100 (c) measured by AFM.

length in the SiCN samples originate from the small residual stress that prevails after indentation. Correspondingly, small values are observed for the c/a ratio, and a weakly developed concave shape of the crack opening profile arises from the fast decrease of the opening associated with the short crack length. The observed slight increase of the maximum crack opening and crack length with pyrolysis temperature are a consequence of the increased residual stress, resulting from the reduced free volume available for densification under indentation. The relatively small changes in the overall crack opening profiles upon increasing the pyrolysis temperature suggest that despite the change in free volume, the principal microstructure is not significantly altered.

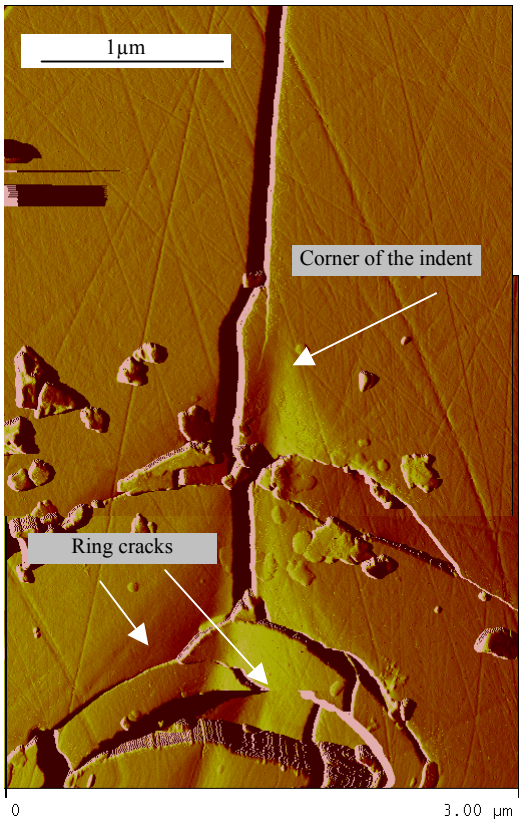

Figure 7.13. Overlapped AFM images of the crack opening for radial indentation cracks inside of the indent (r<a) of polymer derived SiCN-800.

Table 7.3 Measured values of relevant geometrical parameters of the radial crack system of Vickers indent in polymer-derived amorphous SiCN ceramics obtained with different applied loads; **c** is the crack length, **a** the half diagonal of the indent, and c_1 the position of the inner tip of the crack from the indent center estimated by Hill's expanding cavity model [98Hil].

Load (N)	SiCN-800				SiCN-900			
	c_1 (µm)	a (µm)	c (µm)	c/a	c_1 (µm)	A (µm)	c (µm)	c/a
19.6	25.3	29.9	41.5	1.39	28.6	33.8	49.8	1.47
24.5	27.6	32.6	46.1	1.41				
29.4					31.8	37.6	57.3	1.52
Load (N)	**SiCN-1000**				**SiCN-1100**			
	c_1 (µm)	a (µm)	c (µm)	c/a	c_1 (µm)	A (µm)	c (µm)	c/a
19.6	25.1	29.6	48.0	1.60	29.2	34.5	53.7	1.55
29.4	29.3	34.6	61.4	1.77	32.9	37.2	64.3	1.71
39.2	36.5	43.2	78.7	1.82	37.5	44.3	81.1	1.82
49.0	42.4	50.1	92.3	1.84	44.2	52.2	96.6	1.86

7.2.3. Normalization of COD data

In order to establish a suitable means to compare the crack opening profiles of various materials, a procedure for normalizing the crack opening data has been developed. The starting basis for this procedure is the Sneddon double integral equation [69Sne] (equation (5.11) in section 5.3.2), which has been normalized in the following manner. According to this equation, the crack opening displacement, u, of indentation cracks at the position r (Figure 7.14) is related to the residual stress σ acting at r' via

$$u(r,c) = \frac{1}{E'}\int_{r}^{c} h(c',r)\left(\int_{0}^{c'} h(c',r')\sigma(r')dr'\right)dc', \qquad (5.11)$$

where E', c and h denote Young's modulus for plane strain ($E'=E/(1-\nu^2)$), the crack length, and a weight function which depends on the geometry of the crack, respectively, while r' and c' are integration variables. The component of the residual stress σ(r') inside the plastic zone ($c_1<r<a$) is given by the following linear equation [98Hil]:

$$\sigma(r) = -k\sigma_R + (k+1)\left(\frac{r-c_1}{a-c_1}\right). \qquad (5.12)$$

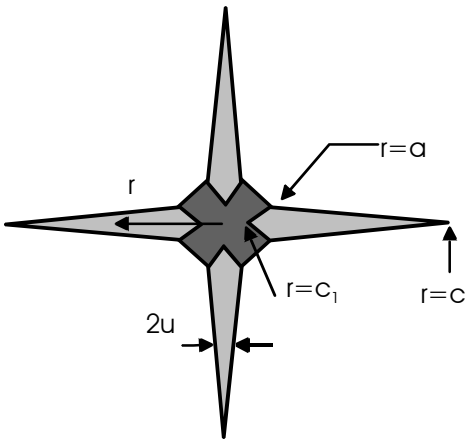

Figure 7.14. Schematic representation of the radial crack system around a Vickers indent with relevant geometric parameters.

The second component of σ(r') is the monotonously decreasing residual stress outside the plastic zone ($a<r<c$), which is described by the following power-law equation:

$$\sigma(r) = \sigma_R\left(\frac{a}{r}\right)^m. \qquad (5.13)$$

In the first step, the length scale is normalized by the indent size, more precisely the half diameter, a, and the obtained dimensionless coordinates are denoted by capital letters as follows:

$$R = \frac{r}{a};\ R' = \frac{r'}{a};\ C = \frac{c}{a};\ C' = \frac{c'}{a}. \tag{7.1}$$

For the normalization of the residual stress distribution σ acting at r', the maximum residual stress σ_R, which is reached in the vicinity of the indent corner, is used as scaling parameter:

$$\Sigma(R') = \frac{\sigma(r')}{\sigma_R}. \tag{7.2}$$

The relation between residual stresses and hardness H or indentation load P, respectively, is described by a material-dependent parameter α [79Law]:

$$\sigma_R = \alpha H = \frac{\alpha P}{2a^2}. \tag{7.3}$$

Combination of Equations 7.1-3 yields the following dimensionless representation of the crack opening profile

$$U(R) = \frac{\alpha}{2} \int_{R}^{C} h(C', R) \left(\int_{0}^{C'} \Sigma(R')\, h(C', R')\, dR' \right) dC', \tag{7.4}$$

where the normalized crack opening U is defined as

$$U = \frac{uaE'}{P}. \tag{7.5}$$

The influence of the stiffness E' is eliminated by the normalization according to Equation (7.5), while the effect of the indentation load P is reduced, but not completely removed. Although Equation (7.5) does not provide a universal plot of the crack opening profile for a specific material, it enables nevertheless a clear distinction among materials under investigation as it will be shown in the following.

The normalized crack opening displacements of soda lime and borosilicate glass are plotted in Figure 7.14. It is apparent from comparison with Figure 7.10, that the normalization leads to

bundling of the crack profiles into two distinct groups. Within each group, the profiles are extended over a similar range of radial coordinates, whereas slightly different values are observed for the maximum normalized openings. The formation of two groups of profiles effected by the normalization is very useful to visually highlight the difference in the fracture behaviour of the two glasses. In particular, the smaller normalized opening of the borosilicate glass in conjunction with the shorter crack lengths, as compared to the soda lime glass, are a clear indication of its anomalous behaviour.

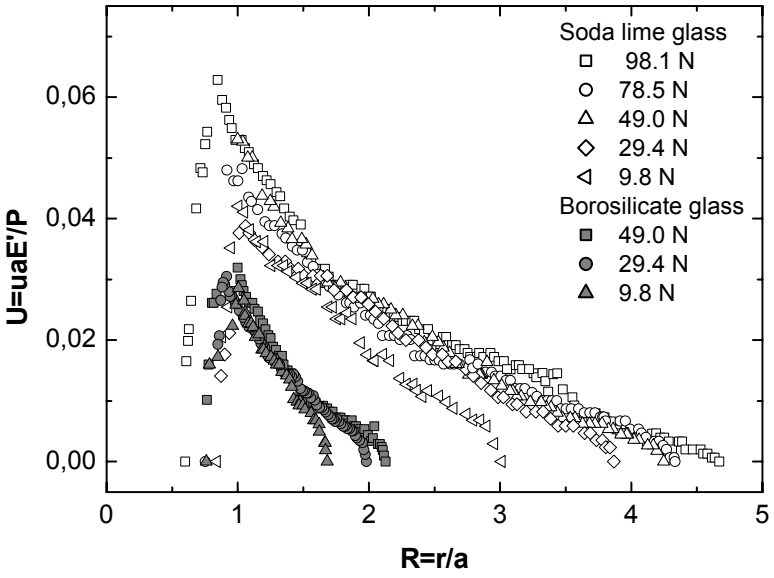

Figure 7.15. Normalized crack opening profiles of glasses tested with different applied loads. Open symbols are for soda lime glass

In order to compare the polymer-derived amorphous ceramics synthesised at different pyrolysis temperatures a normalized plot of the COD data shown in Figure 7.12 is depicted in Figure 7.16. This plot clearly reveals the effect of increasing pyrolysis temperature on the indentation behaviour of these materials, which consists in increasing the normalized crack opening and length. However, there are some small deviations from the expected behaviour. For example, the normalized crack length in SiCN-1100 is smaller than in SiCN-1000, although both were exposed to the same load of 29.4 N. These irregularities are an indication of the residual stress remaining from the processing of the SiCN samples, which

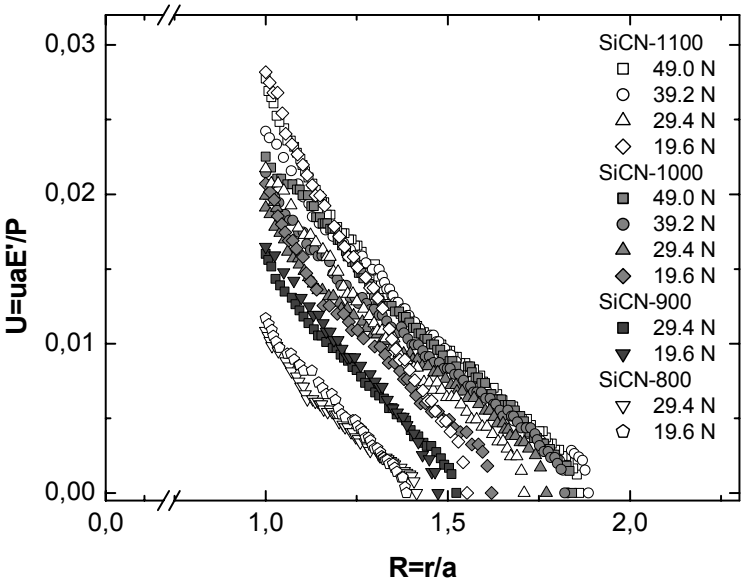

Figure 7.16. Normalized crack opening profiles of polymer-derived amorphous SiCN ceramics from different applied loads.

will be further discussed in section 7.3.2. Nevertheless, the normalized plot clearly demonstrates hat less densification occurs in SiCN samples obtained at a higher temperature of pyrolysis (compare section 7.1.2).

A comparison between the polymer-derived amorphous SiCN ceramics and the two types of glasses is made in Figure 7.17. Here the data were restricted to the load of 29.4 N, since the normalization is unable to completely remove the effect of the indentation load. It is seen that the amorphous ceramics have the smallest normalized opening as well as the shortest crack lengths among the three types of samples. This observation confirms that this type of ceramics exhibits even more anomalous behaviour than the borosilicate glass. In view of the properties of fused silica discussed in section 7.1.2, one would expect that normalized COD data of this glass to occur towards lower normalized crack opening and length with respect to SiCN-800.

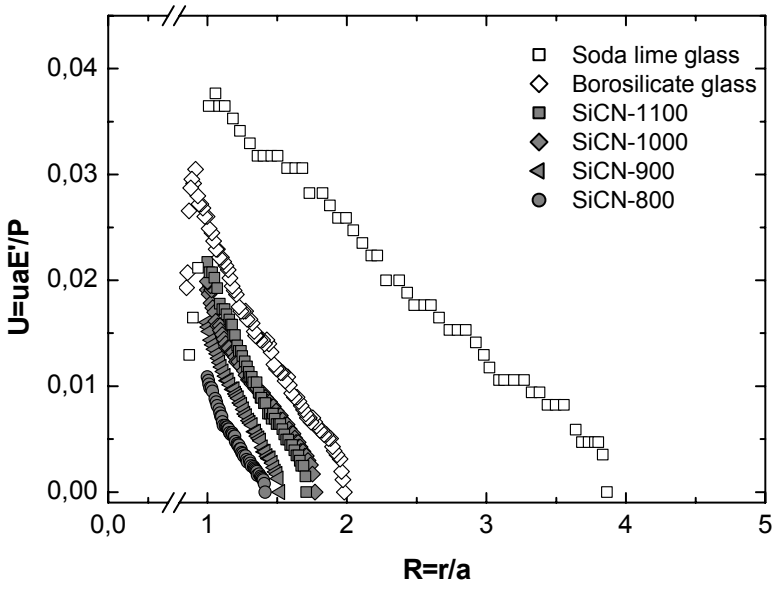

Figure 7.17. Normalized crack opening profiles of glasses and polymer derived SiCN amorphous ceramics for an applied load of 29.4 N.

The normalization furthermore brings out that the anomalous behaviour is associated with a significantly larger slope of the profiles than in case of normal behaviour.

Taken together, Figures 7.15 to 7.17 clearly demonstrate the ability of the normalization procedure to directly compare the indentation behaviour of different materials.

7.3. Determination of residual stress distribution and fracture toughness from overall COD data

Measurements of the crack opening displacements allow a quantitative evaluation of the residual stresses at the contact site. This opens the possibility to test the interpretations given in the earlier sections, specifically to determine whether and to which extent the residual stress in the anomalous materials is reduced compared to normal glasses. Moreover, the stress intensity factor or fracture toughness of an investigated material can be gained from the determined residual stress. In addition, knowledge of the residual stress is an important prerequisite for other mechanical testing methods for fracture toughness determination (such as bending tests) because of the increasing use of pointed indenters to notch brittle solids [93Law].

According to the Sneddon double integral equation for the crack opening displacement (Equation (5.11)), the residual stress field around the indent can be derived from the measured crack opening profile of the radial crack. An analytical solution to this problem, however, is not available. Hence, a numerical method based upon the weight function approach was used to solve the integral equation, which offers the advantage that no special functional dependence of the residual stress upon the distance from the indent needs to be assumed a priori. For the purpose of numerical analysis, a step function was assumed for the residual stress, where the number of the steps, n, can be chosen arbitrarily such that the stress σ_i referring to step i is constant in the interval from r_i to r_{i+1} (Figure 7.18). For a step-wise constant residual stress distribution, Equation (5.11) assumes the following form:

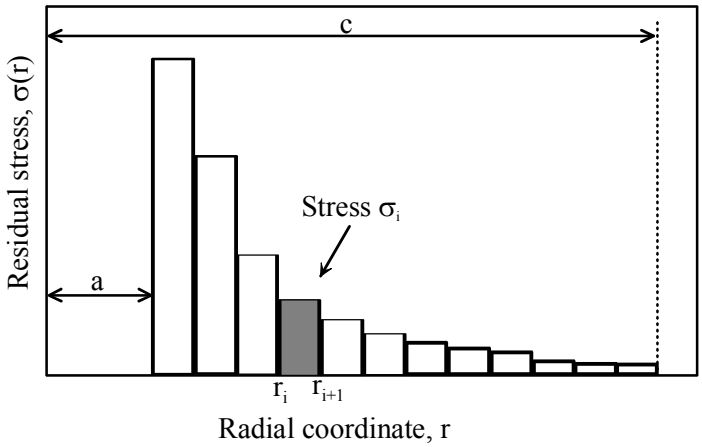

Figure 7.18. Schematic of residual stress distribution around an indent where a is indent size and c is the crack length.

$$u(r) = \sum_{i}^{n} \frac{\sigma_i}{E'} \int_{\max(r,r_i)}^{c} h(c',r) \left(\int_{r_i}^{\min(c',r_{i+1})} h(c',r')dr' \right) dc' . \qquad (7.6)$$

According to this equation, the crack opening displacement, u, is a linear function of the residual stresses σ_i,

$$u(r) = \sum_i^n \sigma_i f_i , \tag{7.7}$$

where the coefficients f_i denote geometry-dependent integrals:

$$f_i(r) = \frac{1}{E'} \int_{\max(r,r_i)}^{c} h(c',r) \left(\int_{r_i}^{\min(c',r_{i+1})} h(c',r')dr' \right) dc' . \tag{7.8}$$

In the following, the weight function for a half penny-shaped crack is utilized to describe the geometry of the radial crack system around the indent:

$$h(c,r) = \frac{2}{\sqrt{\pi c}} \frac{r}{\sqrt{c^2 - r^2}} . \tag{7.9}$$

This function is the only example currently available in the literature in this context, and it is considered as appropriate for the present evaluations, since the cracks were found to be of the centrally-loaded type (compare section 7.2.1).

The minimization of the sum of the squared error between measured and calculated crack opening profiles, *i.e.*

$$\sum_i (u_{meas}(r_i) - \sum_j f_j(r_i)\sigma_j)^2 \tag{7.10}$$

yields a system of linear equations:

$$\begin{pmatrix} \sum_i f_1(r_i) f_1(r_i) & \sum_i f_2(r_i) f_1(r_i) & \sum_i f_3(r_i) f_1(r_i) & \dots & \sum_i f_j(r_i) f_1(r_i) \\ \sum_i f_1(r_i) f_2(r_i) & \sum_i f_2(r_i) f_2(r_i) & \sum_i f_3(r_i) f_2(r_i) & \dots & \sum_i f_j(r_i) f_2(r_i) \\ \sum_i f_1(r_i) f_3(r_i) & \sum_i f_2(r_i) f_3(r_i) & \sum_i f_3(r_i) f_3(r_i) & \dots & \sum_i f_j(r_i) f_3(r_i) \\ \dots & \dots & \dots & \dots & \dots \\ \sum_i f_1(r_i) f_j(r_i) & \sum_i f_2(r_i) f_j(r_i) & \sum_i f_3(r_i) f_j(r_i) & \dots & \sum_i f_j(r_i) f_j(r_i) \end{pmatrix} \begin{pmatrix} \sigma_1 \\ \sigma_2 \\ \sigma_3 \\ \dots \\ \sigma_j \end{pmatrix} = \begin{pmatrix} \sum_i u_{meas}(r_i) f_1(r_i) \\ \sum_i u_{meas}(r_i) f_2(r_i) \\ \sum_i u_{meas}(r_i) f_3(r_i) \\ \dots \\ \sum_i u_{meas}(r_i) f_j(r_i) \end{pmatrix} \tag{7.11}$$

The residual stress, σ_i, acting in the interval i can be obtained by solving Equation (7.11).

The stress intensity factor (fracture toughness) of the material can be determined from the overall COD data with the aid of [93Law]

$$K_C = \int_0^c \sigma_{total} h(c,r) dr \,. \tag{7.12}$$

From the n values of the stress σ_i, which correspond to the whole crack area (Equation (7.11)), the actual stress intensity factor in the cracked material is obtained using the following equation

$$K_C = \frac{2}{\sqrt{\pi c}} \sum_i^n \sigma_i (\sqrt{c^2 - r_i} - \sqrt{c^2 - r_{i+1}}) \,. \tag{7.13}$$

To calculate the residual stress distribution and stress intensity factor from the overall crack opening profile via Equations (7.6 - 7.13), a program was written based on Mathematica 4.1 (see Appendix 2). As a first step, the measured data points were fitted using the Bezier spline data smoother. Then the calculation was performed with 25 steps for the glasses, while 15 steps were used for the polymer-derived amorphous SiCN ceramics due to the the comparatively smaller crack lengths.

7.3.1. Normal and anomalous glass

The calculated values for the residual stress distribution around the indent (r>a, Figure 7.14) of the two glasses are shown in Figure 7.19. For each applied load and for both glasses, the obtained curves clearly show a rapid decrease of the residual stress with rising distance from the indent. Except for the relatively high value obtained for a load of 9.81N applied to borosilicate glass, the maximum residual stress, which is reached in the vicinity of the indent corner, is almost independent of applied load. In addition, the maximum stress is smaller in the borosilicate than in the soda lime glass due the anomalous indentation behaviour of the former glass.

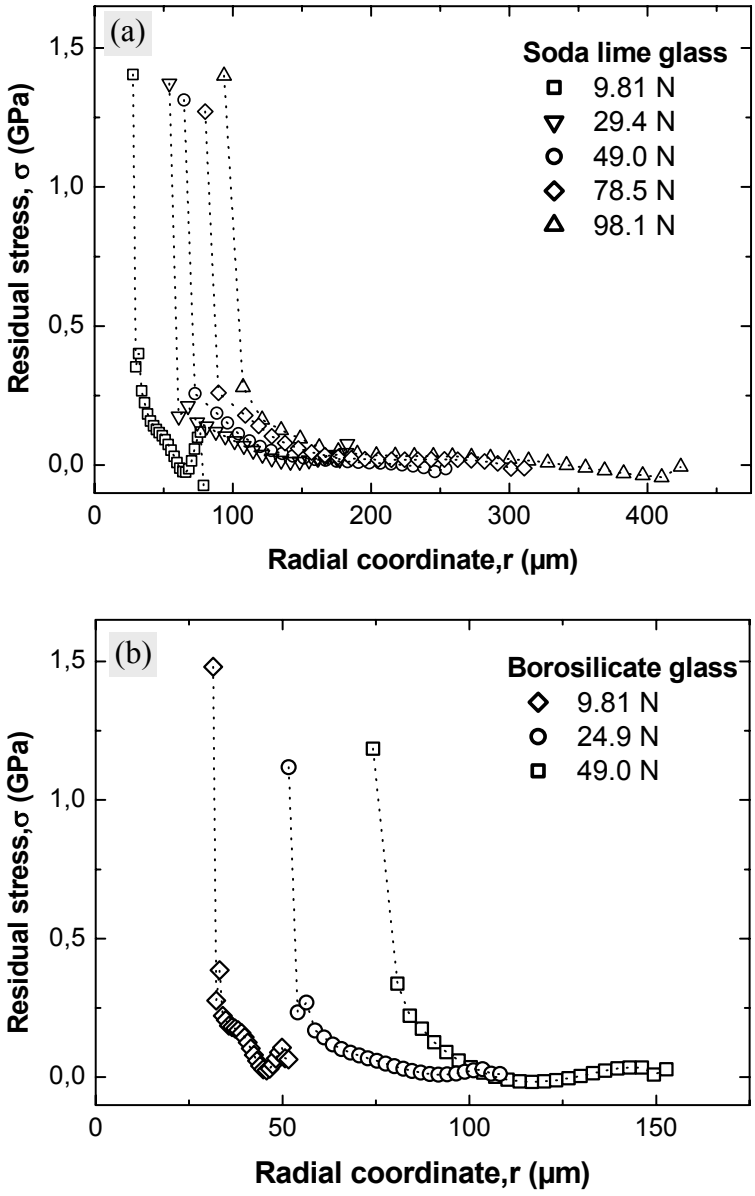

Figure 7.19. Calculated residual stress distribution around the Vickers indent (r>a) in soda lime (a), and borosilicate (b) glass.

In order to compare the residual stress distributions obtained for different loads, the radial coordinate, r, was normalized by the indent size, a; the corresponding plots for both glasses are displayed in Figure 7.20. It can be seen that the data points belonging to different loads show only weak scattering, demonstrating that the residual stress is a characteristic of the material.

The normalised plots have been used to determine the extent to which the calculated residual stresses follow the dependence predicted by Hill´s model of an expanding sphere. According

to this model, the residual stress is expected to decay with a power of three (m=3, Equation 5.13):

$$\sigma(r) = \sigma_R \left(\frac{a}{r} \right)^3 . \qquad (5.13)$$

The best fits to this power-law are drawn as solid lines in Figure 7.20. For both glasses, the fit describes the calculated data reasonably well for larger distances from the indent corner. However, the fits do not include the highest residual stress values that occur close to the indent corner (r/a = 1). An explanation for this discrepancy is the deviation of the indentation crack geometry from the ideal half-penny shape, which is more pronounced for borosilicate than for soda lime glass (Figure 7.2). This conclusion is in accordance with the fact that the quality of the fit is lower for the former glass (R^2 values, Figure 7.20). However, the observed deviations are stronger than expected, as the assumption of half-penny crack geometry is reported to be appropriate if the c/a ratio is

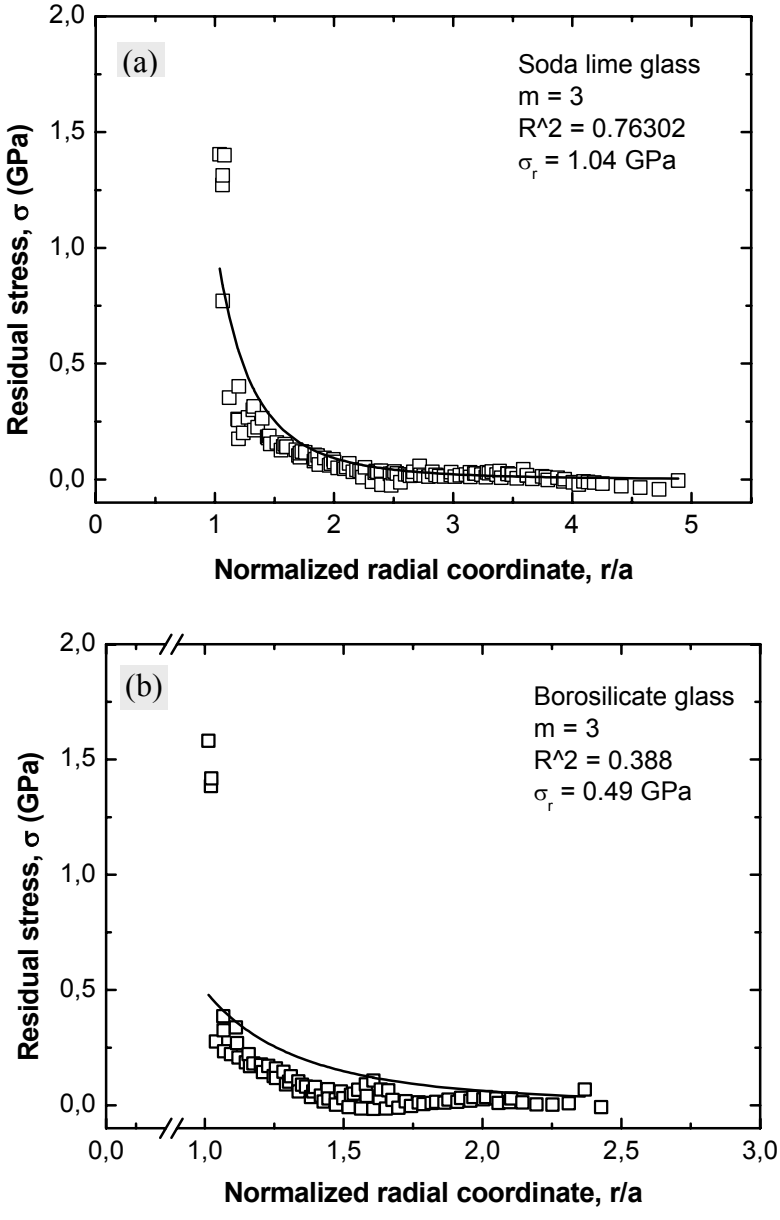

Figure 7.20. Calculated residual stress distributions around the Vickers indent in soda lime (a), and borosilicate (b) glass. The solid lines are fits to the power-law function according to Hill´s model.

higher than 2.0 [87Jon], which is fulfilled for all loads in both glasses, with the exception of 9.81 N for borosilicate glass (Table 7.2).

In addition, the geometry of the Vickers indent deviates from ideal spherical shape, and hence the residual stress distribution does not follow the power-law function valid for the spherical expansion model. In this respect, Rödel suggested that the residual stress in soda lime glass decreases with a power of four [93Röd]. In the present case, when the fits are performed with this value of four, the highest stresses close to the indent corner are indeed better reproduced. However, this improvement is achieved at the expense of the quality of the fit at larger distances. It should be stressed that if an exponent larger than 3 is used for fitting, the physical meaning of equation (5.13) is lost.

Nonetheless, the results obtained by the fitting procedure using Equation 5.13 and m = 3 reveal a clear correlation between the indentation behaviour of a material and the residual stress distribution. In particular, they indicate significantly higher maximum residual stress in the normal relative to anomalous glass, *i.e.* σ_R = 1.04 GPa for soda-lime and σ_R = 0.49 GPa for borosilicate. The relative values of σ_R are in reasonable agreement with a factor of ~3 difference between normal and anomalous glasses which was found in earlier stress birefringence measurements [79Aro]. Moreover, the high absolute values in the GPa range emphasize the intensity of the residual contact deformation. Considering the general difficulties in determining the residual stress intensity with high accuracy, the present approach allows an appropriate estimate for this important material parameter.

The stress intensity factors calculated by using Equation (7.13) are presented in Figure 7.21. For each glass, the values obtained for different loads are almost identical (the only slightly larger deviation is encountered for a load of 98.1N applied to soda lime glass). The weak scatter of the data proves that the evaluated approach is well-suited for the determination of stress

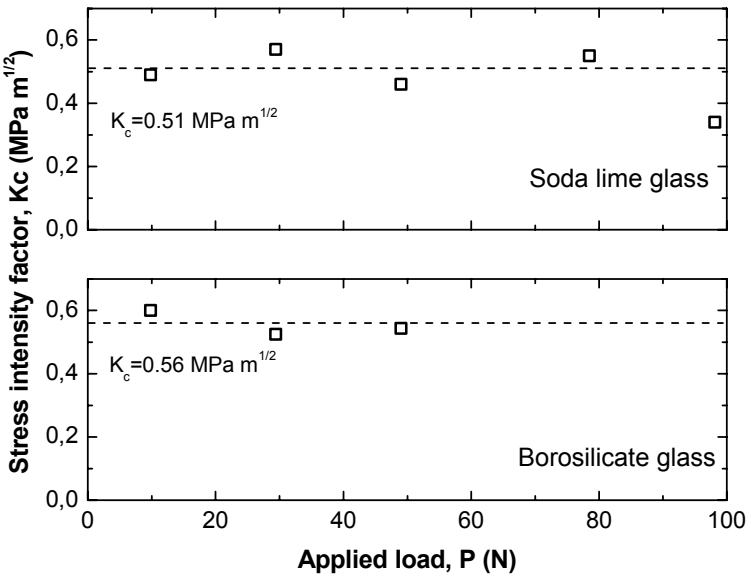

Figure 7.21. Stress intensity factors for the glasses calculated from the overall COD data.

intensity factors. For soda lime glass, an average value of 0.51 MPa $m^{1/2}$ is obtained, while a mean value of 0.56 MPa $m^{1/2}$ is calculated for borosilicate glass. These are lower than the widely quoted, respective values of 0.75 MPa $m^{1/2}$ and 0.76 MPa $m^{1/2}$, as derived from measurements using a DCB technique [69Wie]. It is well known that the values obtained for fracture toughness by indentation can be lower by about 30% than those obtained by other techniques, which is due to subcritical crack growth that occurs immediately after indentation [84Bin]. Since the present experiments were performed after storing the samples for two days in ambient atmosphere, and furthermore the complete set of measurements took several days, it is evident that subcritical crack growth must have occurred as an effect of the active environment (humidity) reinforced by residual stress. Subcritical crack growth could also explain the small deviation observed for the soda lime glass with the applied load of 98.1 N (yielding a value 0.34 MPa $m^{1/2}$ for the stress intensity factor) because in this case, the measurements were more time consuming due to the very long crack. The effect of subcritical crack growth will be described in further detail within section 7.5.

In view of the potential difficulties encountered in indentation testing, particularly when environmental effects, crack-shape effects, and model assumption are involved, the difference between the values calculated from the overall crack opening profile and the accepted value determined by DCB technique appears still reasonable. In addition, the stress intensity factor obtained for soda lime glass is in good agreement with the value of 0.54 $MPa^{1/2}$ reported by Smith and Scattergood [92Smia], who used the indentation bending test in laboratory environment.

7.3.2. Polymer-derived amorphous SiCN ceramics

Although the amorphous SiCN ceramics exhibit c/a ratios of less than 2 (Table 7.3), the residual stress distribution was nevertheless calculated from the measured crack opening profiles, using the same procedure as for the two glasses. The aim was to determine whether this approach - for the currently accessible maximum loads - yields values in agreement with the tendency expected from the normalised crack opening profiles for the different materials (Figure 7.17). In other words, it should be clarified if the obtained residual stress values fall below the value derived for glasses.

The calculated residual stress distributions around the indent are plotted for each SiCN material in Figure 7.22. The plots show a similar shape as for the glasses, *i.e.* the residual stress decreases steeply from its maximum value. However, the distributions of the low temperature samples (SiCN-800 and SiCN-900) are distinguished from those of the high

temperature samples (SiCN-1000 and SiCN-1100) in that the former show a relatively slow, approximately linear approach of the abscissa, whereas this approach is much faster in the latter cases.

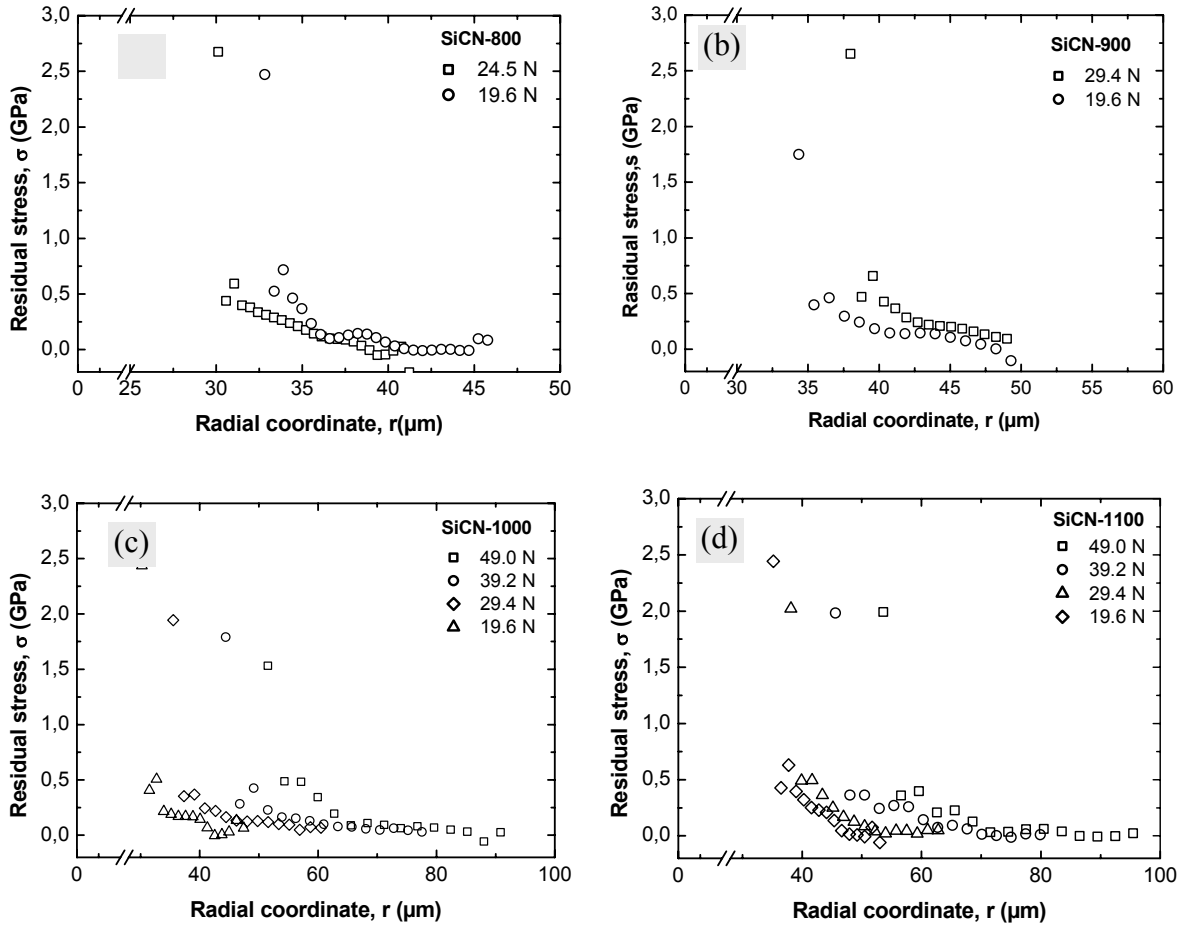

Figure 7.22. Calculated residual stress distributions around the Vickers indent for (r>a) in SiCN-800 (a), SiCN-900 (b), SiCN-1000(c) and SiCN-1100 polymer derived amorphous ceramics.

For the sake of comparing the residual stress distribution for different loads, the same normalization of the radial coordinate has been performed as in the case of glasses (previous section). The obtained plots are shown in Figure 7.23, where the solid lines are fits according to Equation (5.13). Like for the glasses, the normalization is seen to bring the data points onto one curve.

On the another hand, a strong deviation from the ideal decay with a power of three is obvious, especially in the lower temperature samples. The major deficiency of the fits is the exclusion of the highest residual stress values, which is similar to but even more pronounced than in the borosilicate glass, as a result of the stronger deviations from half-penny crack shape (Figures 7.6 and 7.7) in the SiCN samples.

The maximum residual stress values that have been extracted from the fits are summarised in Table 7.4, together with those of the two reference glasses. The SiCN data reveal an increases in σ_R from 0.5 to 0.8 GPa with rising pyrolysis temperature, in accordance with the simultaneous decrease in anomalous behaviour (Figure 7.16).

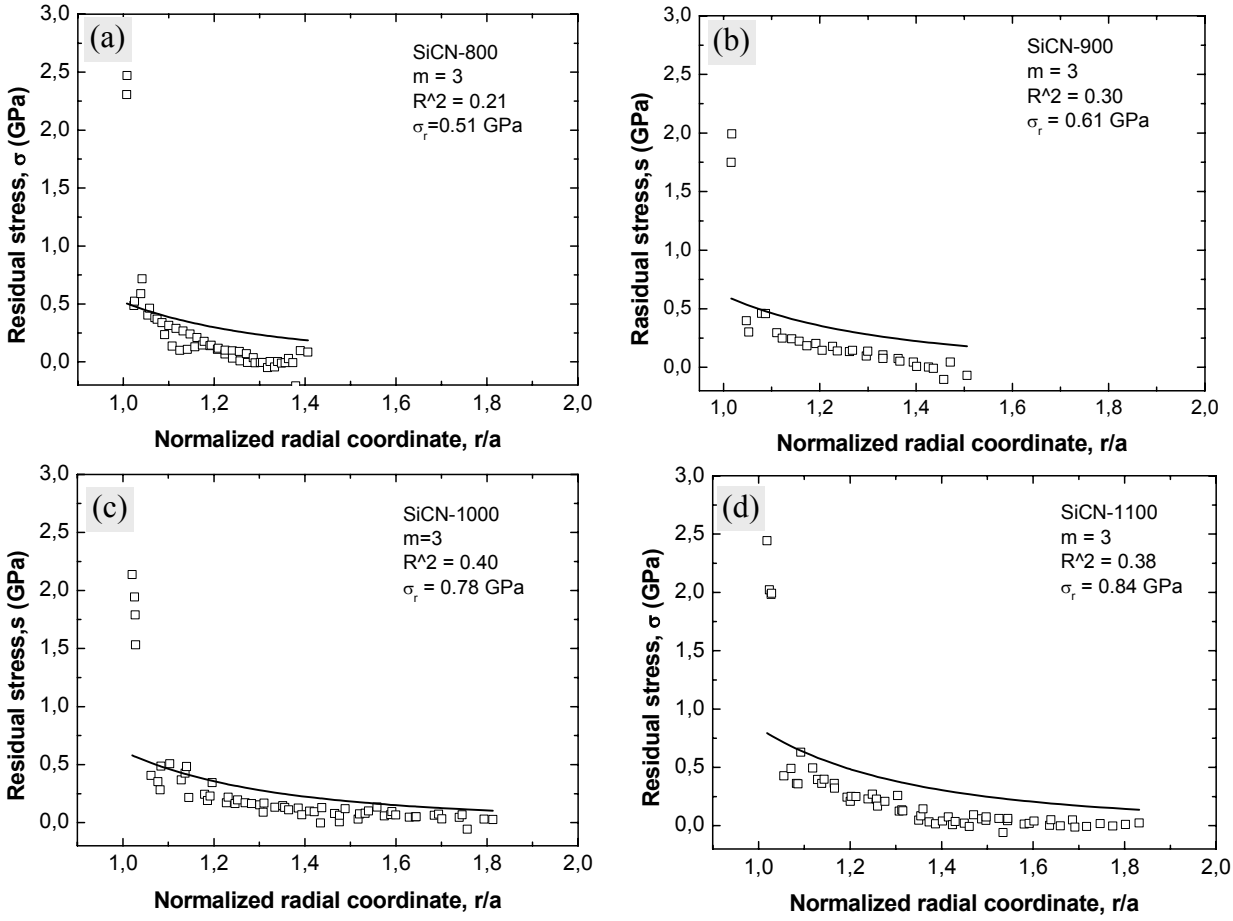

Figure 7.23. Calculated re dual stress distributions around the Vickers indent with curve fits (solid lines) in SiCN-800 (a), SiCN-900 (b), SiCN-1000(c) and SiCN-1100 (d) polymer derived amorphous ceramics.

Comparison with the glasses (Table 7.3) discloses that the σ_R values of the ceramics are smaller than for soda lime glass, in accordance with their respective indentation behaviour (normal versus anomalous).

Table 7.4 Obtained values for maximum residual stress σ_R for glasses and SiCN amorphous ceramics

	Soda lime glass	**Borosilicate glass**	**SiCN-800**	**SiCN-900**	**SiCN-1000**	**SiCN-1100**
σ_R, GPa	1.05	0.49	0.51	0.61	0.78	0.84

On the other hand, the σ_R values belonging to the amorphous SiCN ceramics are slightly higher than that of borosilicate glass. At the first glance, this result appears somewhat unexpected in light of the discussion before, in which it was favoured that the polymer-derived materials behave more anomalous than borosilicate glass (as concluded from the differences in crack length, normalized crack opening, and the cone angles). However, it should be considered that the amorphous ceramics have almost the double value of Young's modulus (Table 6.2). Hence, due to their larger stiffness, the same deformation leads to higher stress.

Another possible explanation for the higher maximum residual stresses is related to the shrinkage of the SiCN material that occurs during the pyrolysis process. Such shrinkage is expected to create stresses inside of the material, which are present already before the indentation process [03Jan]. These stresses cannot easily be eliminated because the temperatures normally applied to release stress in this type of material can induce crystallization [95Bil, 02Bau]. The importance of shrinkage in the present samples is supported by the observation that higher σ_R values are obtained with increasing pyrolysis temperature, since the extent of shrinkage should increase under these conditions. It is noted that in order to minimize the influence of the shrinkage-related residual stresses, which are documented to exist in polymer-derived amorphous SiCN ceramics [03Jan], precaution was taken by cutting the samples in the middle of the specimens (compare section 5.3). However, this measure is apparently only partially successful, indicating that the center region of the specimen still contains a sizeable amount of stress.

Taken together, it is a promising result that the maximum residual stress values obtained for SiCN are of the same order as that of borosilicate glass, especially in view of the various assumptions made within the calculation procedure.

The calculated stress intensity factors for the polymer-derived amorphous SiCN ceramics are shown in Figure 7.24. It is recognised that for each material the obtained value is almost independent of the applied load.

The stress intensity factor is found to increase with the pyrolysis temperature, although the highest value is reached for SiC-1000, despite the fact that SiCN-1100 has the highest value of Young's modulus (see Table 5.2).

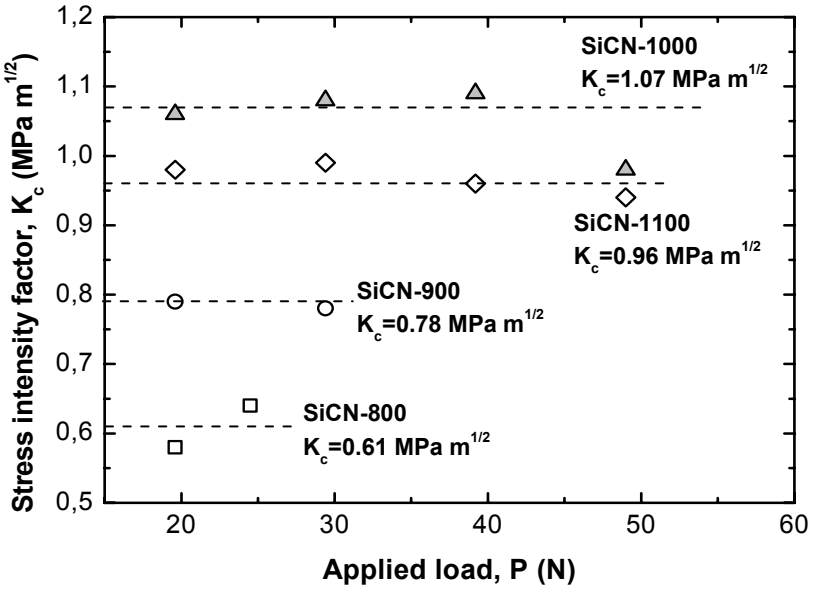

Figure 7.24. Stress intensity factors for the polymer-derived amorphous SiCN ceramics, calculated from the overall COD data.

Until now, only little has been reported about the toughness of polymer-derived amorphous SiCN ceramics. In one study, the best mechanical properties of this type of material were obtained after pyrolysis at 1050°C [02Bau], a result which is in agreement with the present calculation. The present values are larger than those reported by Bauer et al. [01Bau], who obtained 0.7 MPa $m^{1/2}$ for polymer-derived amorphous SiCN ceramic produced by an powder technology route using pyrolysis at 1050°C. In contrast, higher values of 2.1 MPa $m^{1/2}$ have been found by Nishimura et al. [98Nis] for synthesis under the same conditions. However, in the latter case, the estimation was performed by the crack length method using the equation proposed by Anstis et al.[81Ans], which is only appropriate for materials showing normal behavior (see section 7.6). Since it has been confirmed here that polymer-derived amorphous SiCN ceramics exhibit anomalous behaviour, as discussed in more detail below, the use of this equation leads to overestimation of the fracture toughness.

To conclude this section, it is emphasised that the calculation procedure applied to the overall COD data yields the residual stress distribution and stress intensity factors for polymer-derived materials with sufficient accuracy to allow a first evaluation of their indentation characteristics with respect to normal and anomalous behaviour.

7.3.3. Reliability of calculated residual stress and stress intensity factor

In order to assess the reliability of the residual stress and stress intensity factor obtained through the numerical procedure, the following approach has been devised. It is based on from the fact that at full unload, a residual stress field arises from the accommodation of the impression volume by expansion of the deformation zone against the constraining elastic matrix. An analysis of this accommodation gives the following relation for the residual stress parameter χ, which in literature is often called calibration parameter since it has to be calibrated for each material [93Law]:

$$\chi = (\cot\phi)^{2/3}\xi\left(\frac{E}{H}\right)^{1/2}, \tag{7.14}$$

where ϕ is the indenter half-angle, and ξ is a dimensionless constant that depends on the type of deformation (normal or anomalous; see section 5.3.1), E and H are Young's modulus and hardness of the material, respectively. The residual stress parameter consists of two components; the first one, ψ, depends exclusively on the geometry of the indenter:

$$\psi = (\cot\phi)^{2/3}, \tag{7.15}$$

while the other, α, is material dependent:

$$\alpha = \xi\left(\frac{E}{H}\right)^{1/2}. \tag{7.16}$$

The factor ψ can be used to check the reliability of the calculated residual stress and fracture toughness, since for a given indenter it should be constant for all materials and loads. Thus, if identical values of ψ are obtained for different materials, it follows that the maximal residual stress, $\sigma_{R,}$ and stress intensity factor, K_C, of each material have been determined with sufficient accuracy.

According to the above equations, the geometrical constant ψ can be calculated from:

$$\psi = \frac{\chi}{\alpha}. \tag{7.17}$$

The required parameter χ can be obtained in the following way. Starting from the dependence of fracture toughness on the crack length (Equation (5.8)), the latter can be expressed as:

$$c = \left(\frac{\chi P}{K_C} \right)^{2/3}, \tag{7.18}$$

which after taking the logarithm becomes

$$\log c = -0.67 \log \frac{K_C}{\chi} + 0.67 \log P . \tag{7.19}$$

Accordingly, a log-log plot of crack length versus applied load allows to determine the K_C/χ ratio. From that ratio, χ can subsequently be calculated by using the K_C value calculated from the overall COD data.

On the other hand, an estimate for the material dependent parameter α can be gained on the basis that for indenters of fixed profile (Vickers pyramid), the maximum residual stress is proportional to the hardness [79Law]:

$$\sigma_R = \alpha H , \tag{7.20}$$

hence with the calculated maximum residual stress, σ_R, the material constant can be estimated as:

$$\alpha = \sigma_R / H . \tag{7.21}$$

For this purpose, the hardness of the material can be determined in a similar manner as that performed to access the K_c/χ ratio. Explicitly, from the definition of hardness

$$H = \frac{P}{2a^2}, \tag{7.22}$$

the indent size (half of indent diagonal) can be expressed as

$$a = \left(\frac{P}{2H}\right)^{0.5}, \tag{7.23}$$

which corresponds to the following logarithmic expression:

$$\log a = -0.5\log(2H) + 0.5\log P. \tag{7.24}$$

Thus, from a log-log plot of indent size versus applied load, the hardness can be obtained. In this way, the effect of applied load on the hardness values is eliminated.

The procedure described above was applied to the glasses and the polymer-derived amorphous SiCN ceramic materials.

The corresponding logarithmic plots for the glasses are presented in Figure 7.25. For borosilicate glass, small deviations from the linear dependence are observed, which are attributed to difficulties in the determination of indent size due to the pronounced shear faults. The hardness values of both glasses obtained from the linear fits agree well with those reported in literature values

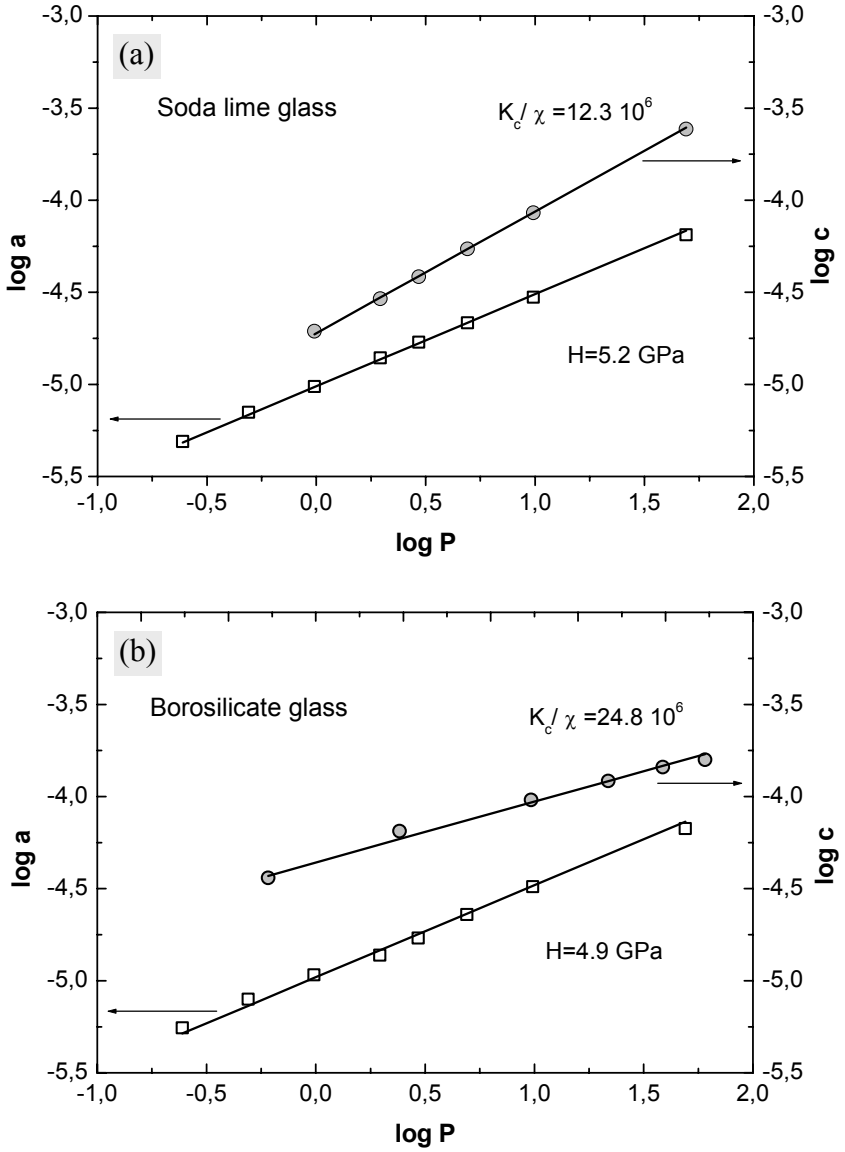

Figure 7.25. Logarithmic plots of indent size and crack length versus applied load with linear fits for soda lime (a) and borosilicate (b) glass.

[63Mar, 79Aro].

In the case of soda lime glass, very good agreement is found for the K_c/χ ratio, when compared with the ratio calculated using the K_c value obtained by the DCB technique (0.75 MPa $m^{1/2}$ [69Wie]) and the widely used value for the calibration parameter (0.058 [81Ans]). By contrast, a similar comparison for the K_c/χ ratio of borosilicate glass is not possible since the calibration parameter is not available. Nevertheless, it can be seen that that ratio K_c/χ obtained for this glass is larger by a factor of two than that for soda lime glass, as a result of the anomalous behaviour of the former one. This is in good agreement with the observation that the maximum residual stress is two times higher in soda lime glass (see previous section).

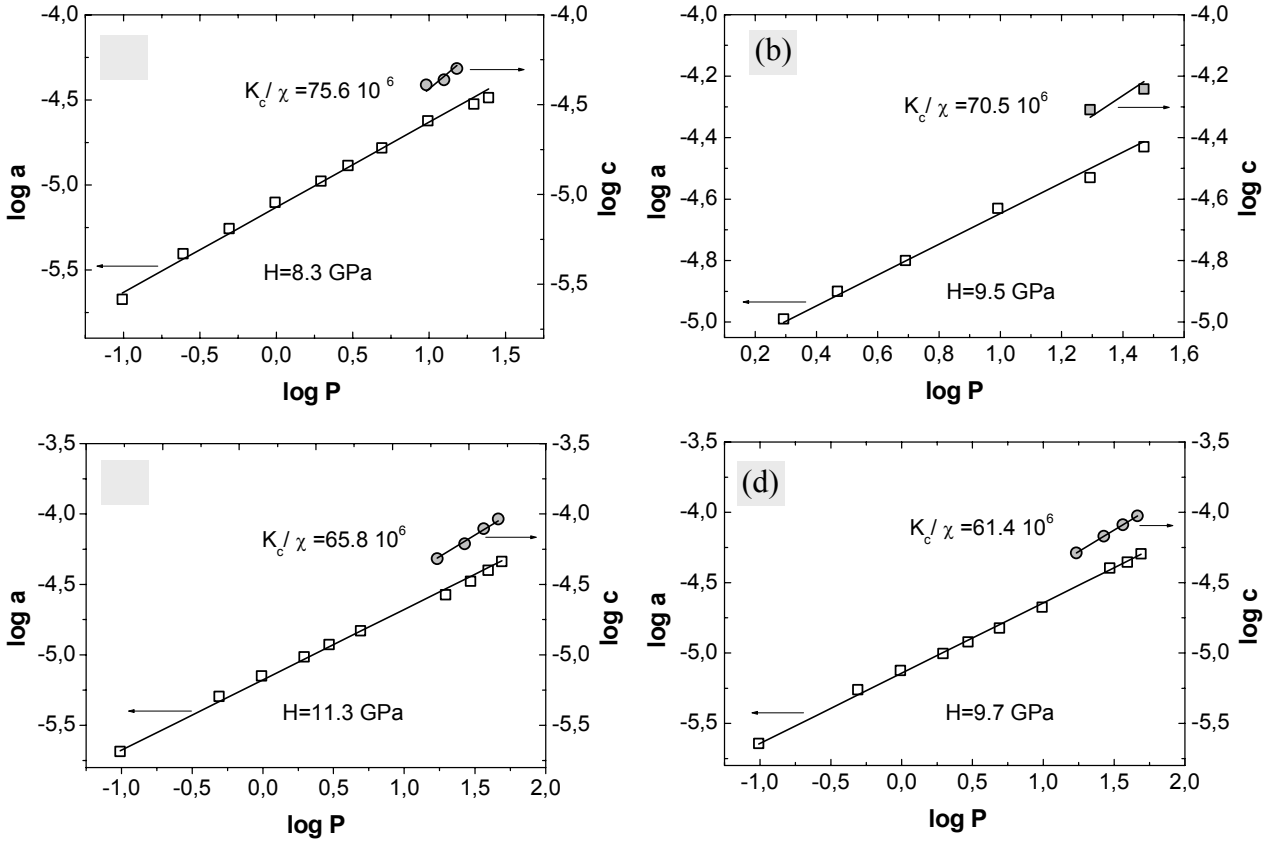

Figure 7.26. Logarithmic plots of indent size and crack length versus applied load with linear fits for polymer- derived SiCN-800 (a); SiCN-900 (b); SiCN-1000 (c) and SiCN-1100 (d) ceramics.

The log-log plots of the polymer-derived SiCN samples are displayed in Figure 7.26. The hardness values obtained from the linear fits show the same trend as the calculated fracture toughness values (Figure 7.23). Specifically, the hardness increases with pyrolysis temperature, and the maximum value is obtained for SiCN pyrolysed at 1000°C. As a further result, the K_C/χ ratio is seen to decrease with temperature; it is stressed that all values are

much larger than for the soda lime and borosilicate glass, again indicative of the more pronounced anomalous behaviour of the polymer-derived amorphous SiCN ceramics. On the other hand, the decrease of these values with temperature is consistent with the increasingly less anomalous behaviour with increasing pyrolysis temperature (as discussed in section 7.1.2).

The values obtained for the calibration parameter, as well as for the material and geometry dependent parameters are collected in Table 7.5.

Table 7.5. Determined values for calibration parameter, χ, material dependent parameter , α, and geometry dependent parameter, ψ.

	Soda lime glass	**Borosilicate glass**	**SiCN-800**	**SiCN-900**	**SiCN-1000**	**SICN-1100**
χ	0.042	0.023	0.008	0.011	0.016	0.016
α	0.19	0.10	0.073	0.064	0.069	0.086
ψ	0.22	0.23	0.11	0.17	0.23	0.18

The residual stress parameter χ = 0.042 obtained for soda lime glass is in very good agreement with the value of 0.049 reported by Lawn at al. [80Law] for Vickers indentation. This agreement is considered as a principal proof for the validity of the calculation procedure, and provides confidence that the values obtained for borosilicate glass and polymer-derived amorphous SiCN ceramics, for which no literature values are available, are also realistic. This is confirmed by the fact that the values for borosilicate glass as well as for the ceramics are smaller than for soda lime glass, as expected for materials that show anomalous behavior

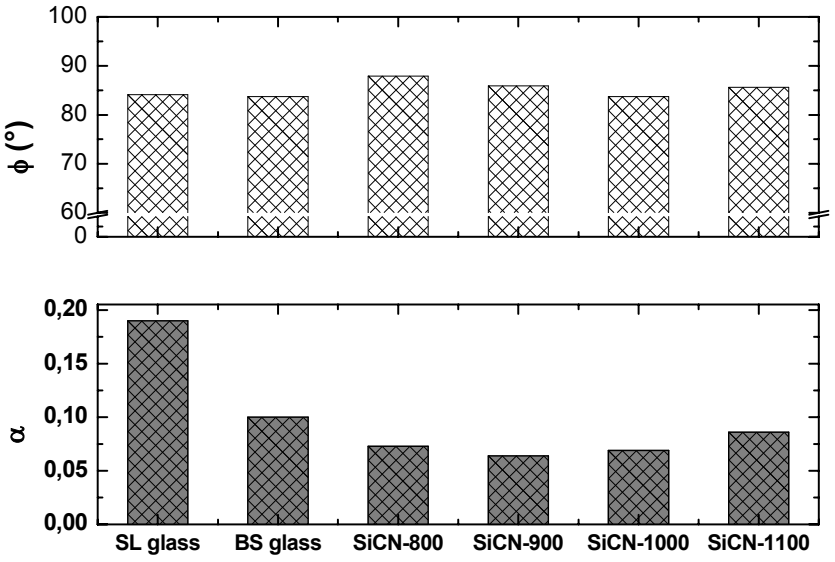

Figure 7.27. Comparison between the characteristic indenter half angle, ϕ, and the material dependent parameter, α, the latter being calculated from the geometrical indenter parameter ψ, for the different investigated samples.

[79Aro]. Further support for the reliability of this approach is apparent from the material dependent parameter α, which is larger for soda lime glass than for borosilicate glass and the amorphous ceramics (Figure 7.27).

Finally, the same conclusion can also be drawn from the parameter ψ, which is expected to depend only on the geometry of the indenter. Except for the deviation observed for SiCN-800 ceramic, the values obtained for ψ are indeed almost identical for each material (Table 7.5). From these ψ values, the half angle of the indenter was calculated by using Equation (7.15). The result is displayed in Figure 7.27, where a graphical comparison is made with the values, discussed above, of the material-dependent parameter α. It is clearly seen that whereas the latter significantly varies among the different materials, the indenter half angle is almost the same for each material, with a mean value of 85°. Compared to half of the standard angle of 136° between the opposite pyramid faces of the Vickers indenter (68°), the calculated indenter half angles are larger by about 25%. For the more anomalous materials, a major source for this discrepancy is certainly the deviation from both, the spherical cavity model and the ideal half penny geometry of the cracks. However, the fact that the soda lime glass shows a similarly high value for the half angle provides evidence that other factors, such as the experimental error, are also of importance.

7.4. Determination of fracture toughness from near tip COD data

Another possibility for fracture toughness determination from the crack opening displacement is offered by fitting the near crack tip profile with an appropriate equation (compare section 5.3.2). An important advantage of this approach is its simplicity, allowing to investigate a larger series of samples with reasonable effort of time. However, its application to a wider range of materials requires an appropriate universal fitting function, which is able to describe deviations from the ideal shape of the near-tip crack profile, as usually observed in anomalous materials. In the following, such a generally applicable fitting equation will be developed.

To measure the near-tip opening profile with optimum resolution, the crack tip region was investigated with an ultra-sharp AFM tip (see section 6.6.1.) Figure 7.28 compares the crack tip profiles of both soda lime and borosilicate glasses, which resulted from a load of 49.0 N. The plots show the half crack opening as a function of distance x from the crack tip, which is related to the radial coordinate r by x = c-r). While directly at the crack tip the crack opening displacement in both glasses is similar, the opening in borosilicate exceeds that in soda lime glass at larger distances (x > 20 µm). This behaviour goes back to the much shorter radial indentation cracks

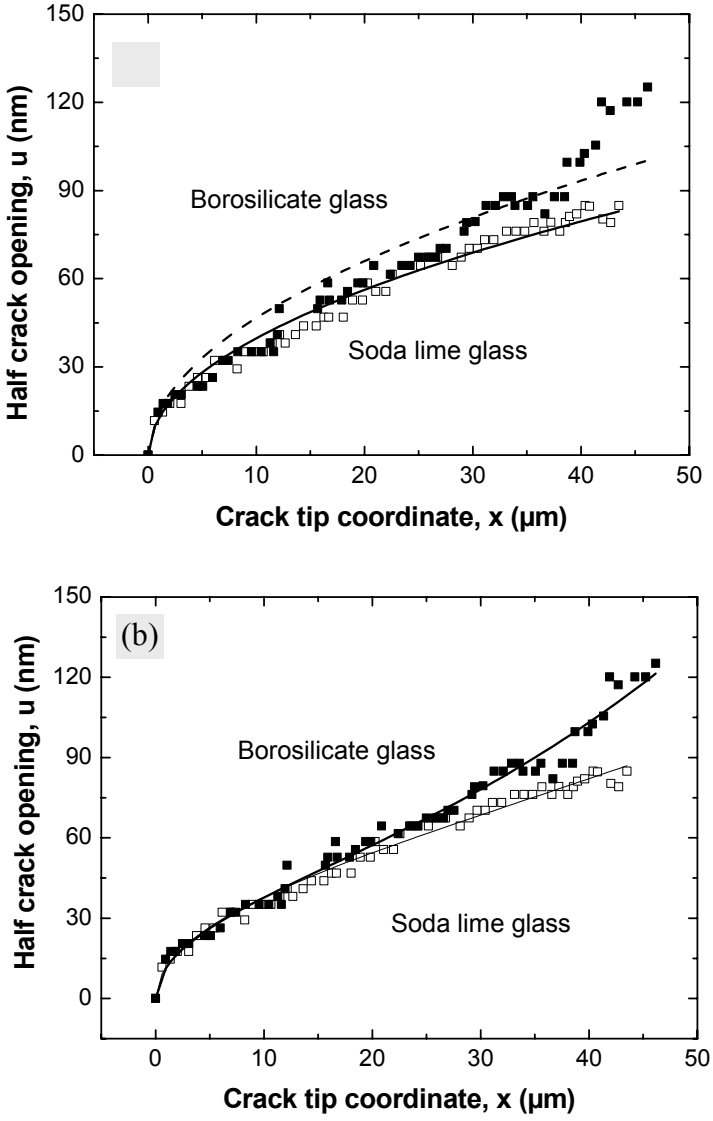

Figure 7.28. Crack opening displacement u(x) in the near tip region for Vickers indentations in soda lime glass (open symbols) and borosilicate glass (filled symbols), for a load of P=49.0 N. The curves are fits to the data, using Equation (5.14) in figure (a) and Equation (7.25) in figure (b).

in the former glass.

For determining the fracture toughness of the glasses, two different literature-reported equations were used for the fitting procedure, which was performed with the aid of the Mathematica 4.1 program given in Appendix 3.

In the first case, the following equation for the near-tip crack opening displacement, corresponding to a square-root-like dependence on the distance x from the crack tip, was applied:

$$u(x) = \frac{K_C}{E'}\sqrt{\frac{8x}{\pi}} \,. \qquad (5.14)$$

The crack profile given by Equation (5.14) is obtained from the near-tip solutions of the displacements of a crack under mode I loading, as reported by Irwin [57Irw]. Inspection of the plots in Figure 7.29 reveals that for both glasses, the dependency of Equation (5.14) is valid in proximity of the crack tip. At larger distance from the tip, by contrast, deviation from the parabolic shape occurs, which effect is stronger for borosilicate glass due to the shorter crack length and hence, more pronounced influence of the residual stress existing in the vicinity of the indent.

The second equation used for the fitting procedure was proposed by Seidel et al. [97Sei]. It is represented by the phenomenological fit

$$u(x) = Ax^{1/2} + Bx^{5/2} \,. \qquad (5.15)$$

Accordingly, an additional term is introduced into Equation 5.14, in order to account for the deviation from parabolic shape:

$$u(x) = \frac{K_C}{E'}\sqrt{\frac{8}{\pi}}x^{1/2} + kx^{5/2} \qquad (7.25)$$

As apparent from Figure 7.28b (fits represented by solid lines), Equation 7.25 turns out to give good agreement with the data of both glasses over the full experimental range.

In order to determine the maximum distance from the crack tip, up to which the two Equations (5.14) and (7.25) provide reliable results, which would be reflected in a constant value of fracture toughness, a comparison between the respective values calculated by both equations

has been made for different fitting ranges (from x=0 ...15 µm up to maximally x=0 ...45 µm), as illustrated in Figure 7.29. According to the fitting lines in Figure 7.28a, direct application of Equation 5.14 should lead to increasing toughness values with rising fitting range, because the distortion of the crack profile from parabolic shape becomes stronger with increasing distance from the crack tip and this equation does not take this effect into account (see section 5.3.2). It is seen that in case of soda lime glass, both types of fits give almost identical results up to the maximal fitting range. By comparison, for borosilicate glass one observes a sizeable difference in the fracture toughness values for fitting ranges larger than ~30 µm. In addition, the estimated variance of the fits increases with the size of the fitting range.

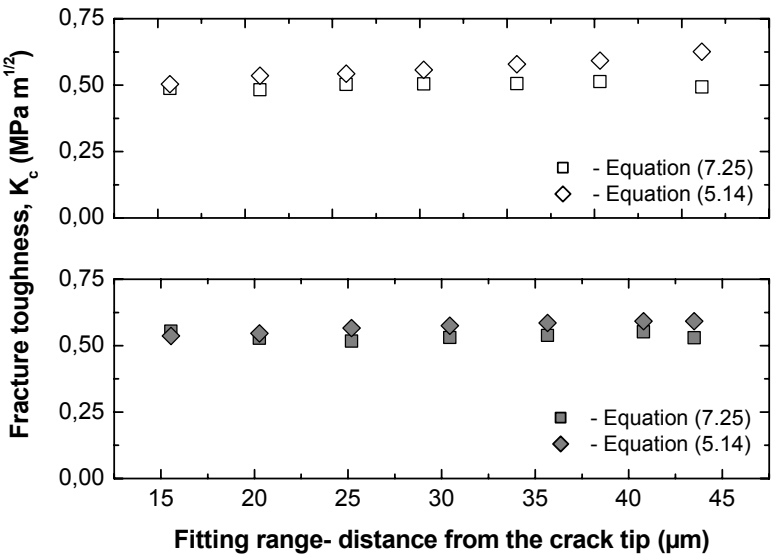

Figure 7.29. Calculated fracture toughness as a function of fitting range for soda lime (full symbols) and borosilicate glass (open symbols), obtained from the near-tip crack profile via Equation (7.25) (squares) and Equation (5.14) (diamonds).

The correction term involved in Equation (7.25) turns out to be successful, as it yields a value for the stress intensity factor which is independent of the fitting range apart from a certain scatter (squares in Figure 7.29). Furthermore, both equations lead to comparable toughness values for a small fitting range, which is expected due to the more parabolic profile right at the tip. In addition, although the indentation crack length is quite different for the two glasses due to the different residual stress concentration, the fracture toughness estimated from the near crack tip opening profile is very similar in accordance with literature [74Wie]. Since the cracks in borosilicate glass are much shorter than in soda lime glass, the deviation between the fits by Equations (5.14) and (7.25) becomes more pronounced in the former case, showing that the outlined correction procedure is more crucial for materials with anomalous behaviour.

Hence, for the polymer-derived amorphous SiCN ceramics, which show extraordinary small crack lengths, fitting attempts of the crack opening COD data were performed directly with

Equation (7.25). However, this type of fit gave only moderate agreement in case of amorphous ceramic specimens with very short cracks (~10 μm in length). One example is shown in Figure 7.30. In general, since in samples with very small crack length, the near crack tip is also very short, an equation is required that provides adequate fitting over an extended range of distances from the crack tip, allowing to include as much data points as possible. Towards this end, a new equation for fitting short cracks is proposed in the present work. In contrast to the equation proposed by Seidel at al. [97Sei], which is based upon expanding the parabolic function given by Equation (5.14) by a second term with an exponent of 5/2, the power-3/2-term is used in the following equation:

$$u(x) = \frac{K_C}{E'}\sqrt{\frac{8}{\pi}}x^{1/2} + kx^{3/2}. \qquad (7.26)$$

Using equation (7.26), very good agreement between the fit and the measured data is achieved for SiCN-800 sample (Figure 7.30). On the other hand, the same equation provided less satisfactory results for a little bit longer cracks, especially for higher loads applied to the polymer-derived amorphous SiCN ceramics pyrolysed at higher temperatures. This is demonstrated in Figure 7.31 for a SiCN-1100 sample. The best fitting quality could be obtained by including the third term with a power of 5/2, which results in the equation

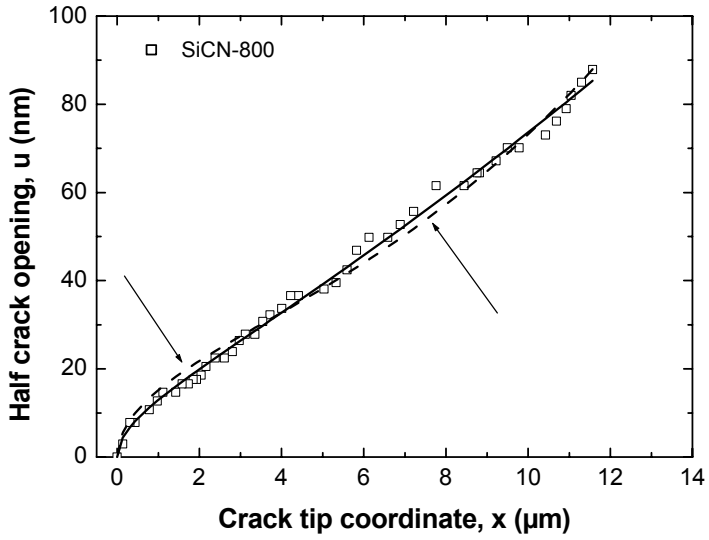

Figure 7.30. Crack opening displacement u(x) from the crack tip for Vickers indentations in polymer-derived SiCN-800 ceramic at applied load P=19.6 N. Data fits obtained with Equations (7.25) and (7.26) are shown as dashed and solid line, respectively. The arrows mark the two regions that show most pronounced differences between measured and fitted data.

$$u(x) = \frac{K_C}{E'}\sqrt{\frac{8}{\pi}}x^{1/2} + kx^{3/2} + k_1x^{5/2}. \qquad (7.27)$$

It is important to note that this equation allowed for proper fittings over almost the entire range of crack lengths, as can be seen in Table 7.6. In contrast, strong deviations are obtained upon using Equation (7.25) for short cracks (resulting from, *e.g.* a load of 19.6 N in SiCN-800), and even larger deviations are observed with Equation (7.26) for longer cracks (arising from, *e.g.* a load of 49.0 N applied to SiCN-1100).

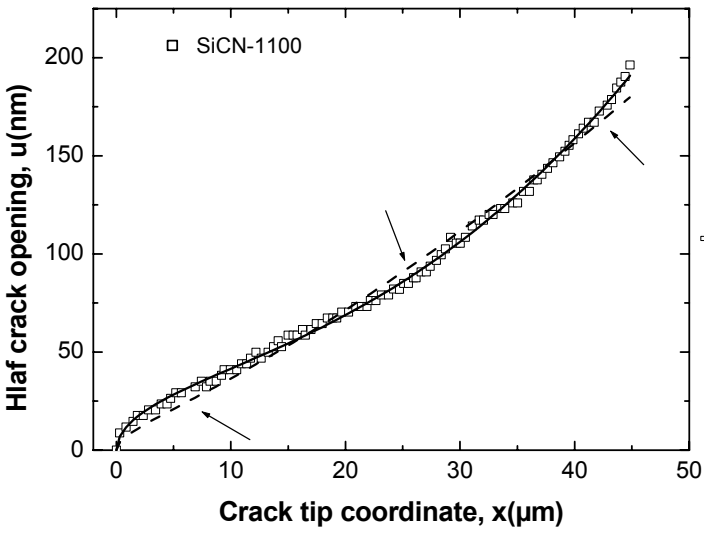

Figure 7.31. Crack opening displacement u(x) from the crack tip for Vickers indentations in polymer-derived SiCN-1100 ceramic at applied load P=49.0 N. Data fits obtained with Equations (7.26) and (7.27) are shown as dashed and solid line, respectively. The arrows mark the regions that show most pronounced differences between measured and fitted data.

Since Equation (7.27) gave the best agreement, it was used for fitting all COD data measured for the glasses and polymer-derived amorphous SiCN ceramic materials. The obtained values for the fracture toughness are summarised in Figure 7.32. They show the same trend as those calculated from the overall crack opening data (Figures 7.21 and 7.24).

Table 7.6. Fracture toughness values obtained by using different fitting equations applied to the crack opening profiles for two different SiCN ceramic samples.

	Short crack ~12 μm in length (SiCN-800)		Long crack ~40 μm in length (SiCN-1100)	
	K_C (MPa $m^{1/2}$)	Estimated variance	K_C (MPa $m^{1/2}$)	Estimated variance
Equation (7.25) *–[97Sei]*	0.82	6.3	1.05	4.4
Equation (7.26) *-present work*	0.61	2.5	0.59	27.6
	0.64	2.4	1.01	4.3

Explicitly, the following observations are made: (i) the K_C values for the polymer-derived amorphous SiCN ceramics are higher than those of the glasses; (ii) the values for the two glasses are almost identical; (iii) within the amorphous ceramic series, an increase in pyrolysis

temperature leads to an increase in fracture toughness, except for the fact that SiCN-1000 instead of SiCN-1100 shows the highest K_C value.

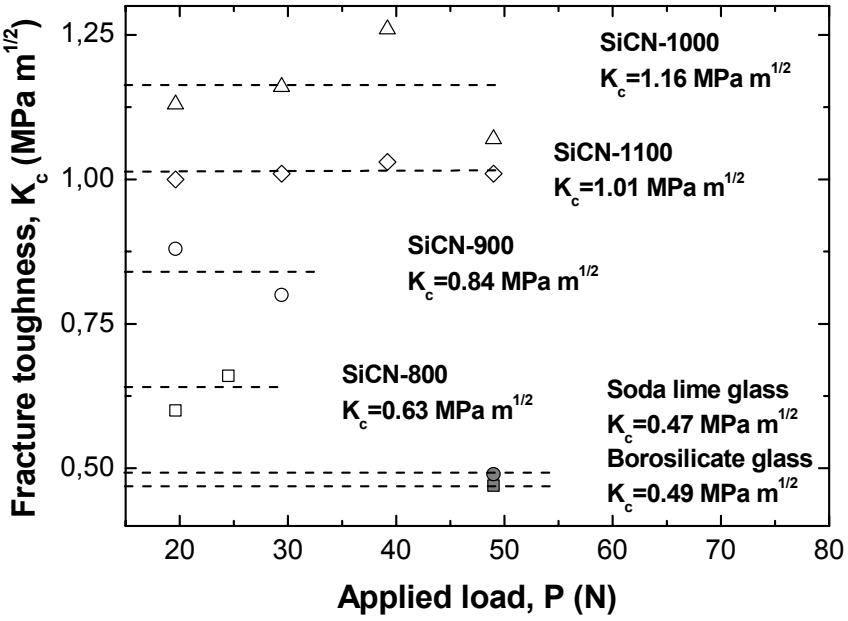

Figure 7.32. Fracture toughness for glasses and polymer-derived SiCN ceramics, calculated from fits performed with Equation (7.27).

Comparison between the two approaches (Table 7.7) reveals that fitting of the crack tip data yields slightly higher fracture toughness values for the four amorphous ceramic, whereas smaller values are obtained in case of the two glasses. However, in most cases the differences are relatively small (between 5 and 10%), which demonstrates the consistency between the two approaches. As an exception, the fracture toughness of borosilicate glass determined by the fitting method is smaller by 14% compared to that obtained from the overall COD data. Nevertheless, in view of the fact that the respective data were acquired from different AFM measurements using different cantilevers, the agreement is quite satisfactory. In total, for practical purposes, both methods give results in reasonable agreement with the literature values [74Wie] for the glasses.

Table 7.7. Comparison of the toughness values [MPa $m^{1/2}$]calculated from the overall and near crack tip COD data.

COD data	**Soda lime glass**	**Borosilicate glass**	**SiCN-800**	**SiCN-900**	**SiCN-1000**	**SICN-1100**
ovearll	0.51	0.56	0.61	0.78	1.07	0.96
near tip	0.47	0.49	0.63	0.84	1.16	1.01

7.5. The influence of subcritical crack growth on COD profiles

Indentations are usually produced in a laboratory ambient, which represents an active environment for subcritical crack growth in many ceramic materials due to the presence of humidity. Under such conditions, chemical processes can contribute to crack extension after the indenter is removed (see section 5.2.2), in addition to the mechanical forces resulting from residual stress in the material after indentation. Since the AFM measurements of the crack opening displacement took several hours under ambient conditions, it became necessary to determine the effect of subcritical crack growth that occurs during the measurements. In particular, it was examined to which extent subcritical crack growth influences the fracture toughness values and residual stress distribution derived from the overall COD data.

As a first step in this direction, the length of indentation cracks was measured as a function of time. In Figure 7.33, the corresponding plots are presented for soda lime and borosilicate glass. Obviously both glasses exhibit substantial crack growth during the first couple of hours. This initial fast growth is followed by a regime with a much smaller growth rate (between 50 and 300 h), and after ~600 h the crack length remains constant. This behaviour is in accordance with other studies of subcritical crack growth in oxidic glasses [85Law, 95Sgl]. It is generally accepted that subcritical crack growth in silicate glasses is primarily caused by hydroxyl ions originating from the presence of surface water. These ions react with the siloxane bonds in the silicate network, which are strained due to residual stress, thus affecting crack propagation (Figure 5.9).

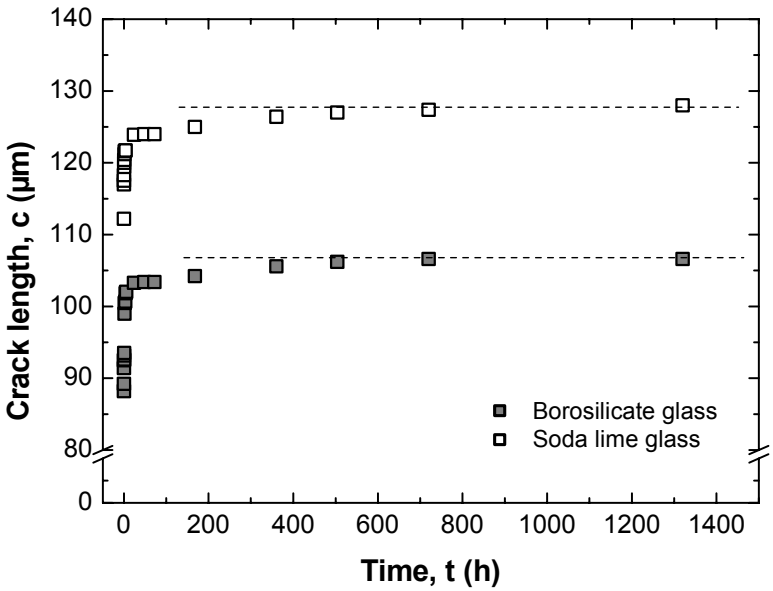

Figure 7.33. Length of radial cracks around 9.81 N Vickers indents in soda lime (open symbols) and borosilicate glass (full symbols) as a function of time after removal of indenter.

In contrast to the soda lime and borosilicate glass, the polymer-derived amorphous SiCN ceramics did not show significant crack growth. No crack growth could be detected in these

materials with the aid of optical microscope. The same conclusion was drawn from atomic force microscopy on SiCN-800, as illustrated by Figures 7.34 a and b, whereas minor increse in crack length (~100 – 200 nm within 3 days) was found in SiCN-1100 by the same technique (Figures 7.34 c and d).

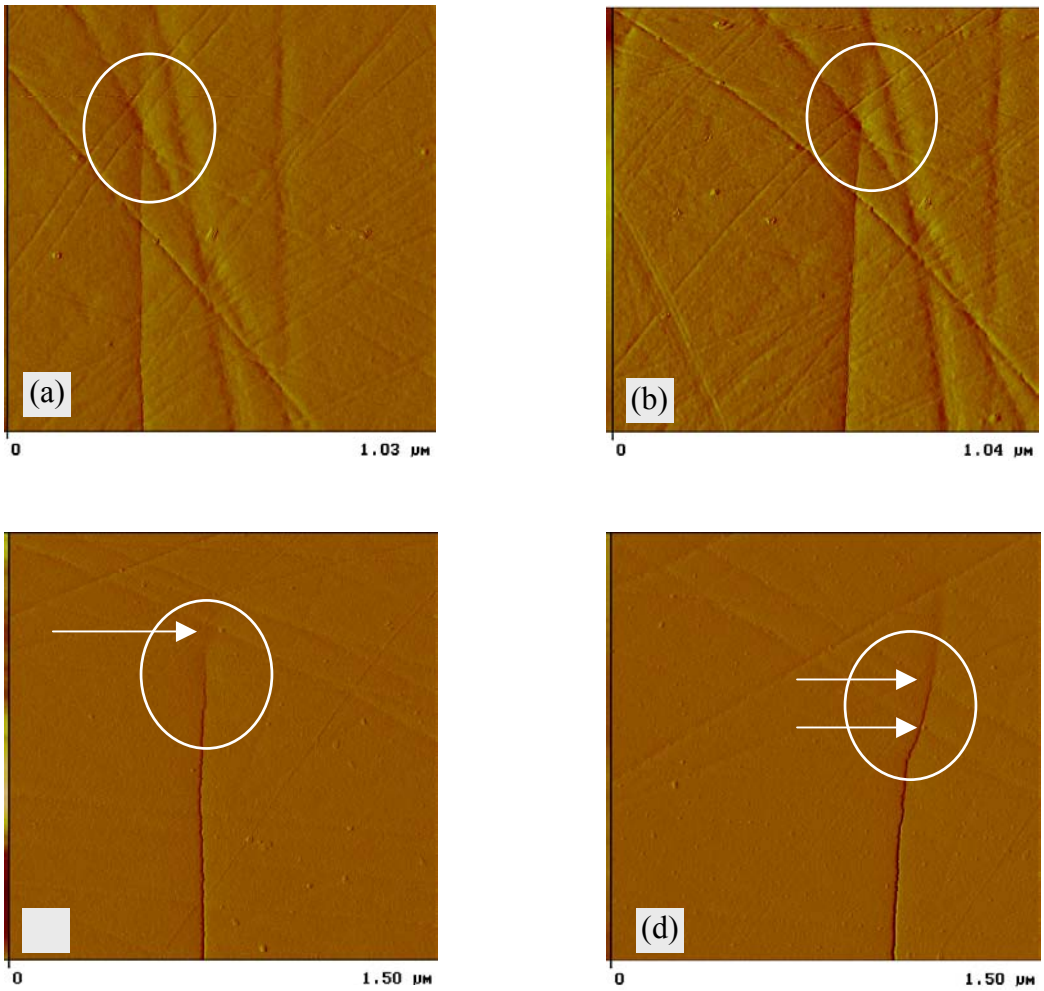

Figure 7.34. AFM images of crack tips (marked by circles and arrows) in polymer-derived amorphous SiCN-800 ceramic after indentation with an applied load of 19.6 N, measured (a) immediately (within one hour) and (b)after 3 days; and in polymer-derived amorphous SiCN-1100 ceramic after indentation with an applied load of 49.0 N observed (c) immediately (within one hour), and (d) after 3 days.

The absence of pronounced crack growth in the amorphous SiCN ceramics can be explained by the lack of oxygen in their structure [98Gre]. In addition, as an anomalous material, exhibits a low level of residual stress. An indication that this stress can in principle lead to subcritical crack growth is provided by the SiCN ceramic samples prepared at higher pyrolysis

temperature (Figure 7.34c/d), which show less anomalous behaviour (see section 7.3.2). However, this effect is negligible in comparison to the glasses.

Accordingly, the influence of subcritical crack growth on the crack opening profiles was investigated only in case of the reference glasses. For this purpose, measurements of the crack opening were performed after three different periods of time, specifically 30 min, 2 days, and 10 days after removal of the indenter. These time intervals were chosen according to the different regimes observed in Figure 7.33. The measurement after 30 min may be designated as "immediately", since this time period represents the minimum time required to prepare the sample for characterisation by electron microscopy (see section 6.6.2). The time evolution of crack opening profiles measured in soda lime and borosilicate glass after applying a load of 49.0 N is depicted in Figure 7.35. In the latter glass, measurement inside the indent was not possible due to the pronounced shear faults. For both glasses, an increase in crack length is clearly visible during the first two days after indentation, while after 10 days only small further changes can be observed. The major changes in crack opening occur near the crack tip in soda lime glass, while for borosilicate glass the crack opening is affected over a much wider range. One explanation for this difference is the more pronounced lateral crack system in borosilicate glass(Figure 7.2), whose growth with time has an influence on the radial crack

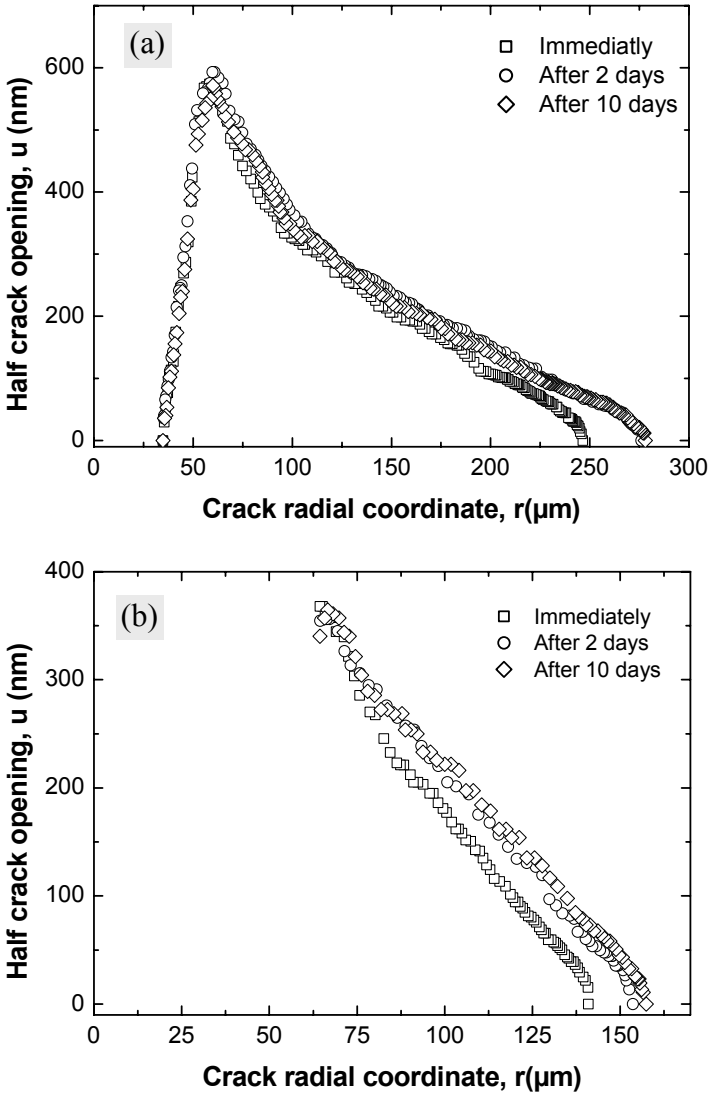

Figure 7.35. Time evolution of crack opening profiles of radial indentation cracks in soda lime (a) and borosilicate (b) glass, in both cases after application of a load of 49.0 N. The measurements were performed by HRSEM.

opening [86Coo]. A closer inspection of the new tip region formed in both glasses (after more than 2 days) has revealed that the corresponding near tip opening is smaller than immediately after indentation.

In order to determine the influence of subcritical crack growth on the values of fracture toughness and maximum residual stress, calculations were performed using the two different approaches described in the previous sections, i.e. evaluation of the overall COD data, and the fitting procedure applied to the near tip profile. The obtained values are compared in Table 7.8.

Table 7.8. Values of the fracture toughness, K_c, and the maximum residual stress, σ_R calculated from COD data measured by SEM after different time periods ("Imm" denotes "immediately", which in reality corresponds to 30min after removal of the indenter).

	Soda lime glass			Borosilicate glass		
	Imm	2days	10days	Imm	2days	10days
Kc form overall COD (MPa $m^{1/2}$)	0.63	0.54	0.50	0.75	0.57	0.54
Kc from near tip COD (MPa $m^{1/2}$)	0.66	0.55	0.49	0.77	0.64	0.53
σ_R form overall COD (GPa)	1.08	1.09	1.04	0.64	0.61	0.62

In agreement with the above observations, the fracture toughness values obtained by both approaches agree well for all three measurement times. The main conclusion that can be drawn from Table 7.8 is that subcritical crack growth has significant influence on the calculated values of fracture toughness, while the values of residual stress are almost unaffected. In particular, the toughness values obtained after 10 days are smaller by about 35% than the values derived from "immediate" measurements. This decrease of K_C with increasing crack length is already pronounced after 2 days, when values smaller by ~ 25% are calculated, consistent with the fact that the main crack growth occurs in this time interval.

The toughness values calculated from the COD data measured "immediately" are in good agreement with values reported in literature [81Gup, 85Law]. That the latter are slightly smaller can be understood in view of the rapid crack growth occurring in this time interval. Moreover, the almost constant maximum residual stress results from the fact that it is mainly determined by the maximum crack opening, which occurs near the indent corner. As can be seen from Figure 7.35, the maximal opening changes only little with time in both glasses. The

observed small deviation arises from the difficulty to precisely determine the crack edges, due to pronounced carbon deposition which takes place during SEM especially if the same position is examined several times.

The values obtained from SEM data measured after 10 days support the conclusion made in section 7.5 that the fracture toughness calculated from AFM-derived data is smaller than the values reported in literature, due to the effect of subcritical crack growth. Since measurements of the crack opening with AFM were carried out after keeping the samples for two days in laboratory environment, and since the complete measurement of one crack took several days, these values are compared with values obtained from the SEM data measured after ten days. The small deviations arising from the difficulties associated to the SEM measurements are apparent from comparison of the data presented in Table 7.9. These data indicate that the fracture toughness derived from fitting the near tip COD data measured by SEM after ten days is slightly higher compared to that obtained from data measured by atomic force microscopy.

Table 7.9. Fracture toughness, K_c, calculated from the near crack tip COD data measured after ten days using AFM and SEM as two different microscopy techniques.

	Fracture toughness K_C, MPa $m^{1/2}$			
	Soda lime glass		Borosilicate glass	
	Overall COD	Near crack tip COD	Overall COD	Near crack tip COD
AFM	0.51	0.47	0.56	0.49
HRSEM	0.50	0.49	0.54	0.53

It should be noted that the fracture toughness values calculated from AFM-derived data of polymer-derived amorphous ceramics are reliable since this type of material does not show an influence of subcritical crack growth.

It is concluded that in case of a material not susceptible to subcritical crack growth, both approaches (based upon the overall and crack-tip COD) can be used equally well for the calculation of fracture toughness. For cracks in materials that are sensitive to the environment, however, one should be aware that this effect leads to slightly lower fracture toughness values. For such materials, it appears more appropriate to use the near crack tip approach since it is less time consuming, or to perform the measurements in vacuum. By comparison, less care has to be taken for measuring the maximum residual stress, since it is much less affected by crack growth.

7.6. Indentation crack length versus crack opening displacement method

The determination of fracture toughness from COD data constitutes a rather novel approach, which has provided first promising results. In order to fully assess its applicability, it is important to compare these results with those obtained by the normally employed indentation crack length (ICL) method. In the following, such a comparison will be made for glasses, since for these materials fracture toughness values determined by the DCB technique are available in the literature, and will be used as a reference.

For this purpose, indentation crack length toughness evaluations were made using

$$K_C = \chi \frac{P}{c^{3/2}}, \tag{5.8}$$

in conjunction with a fixed coefficient of $\delta = 0.016$ in

$$\chi = \delta \left(\frac{E}{H} \right)^{1/2}, \tag{5.9}$$

which was calibrated by tests on normal materials [81Ans]. The fracture toughness values obtained are shown in Table 7.10, along with values from independent double-cantilever-beam (DCB) tests in vacuum [74Wie] and values derived via the COD approach.

Table 7.10. Comparison of the toughness values for soda lime and borosilicate glass determined from DCB technique in vacuum with values obtained from ICL (using optical microscope data) and COD (using AFM data) measurements in ambient atmosphere.

Toughness (MPa $m^{1/2}$)	Soda lime glass	Borosilicate glass
DCB [74Wie]	0.75	0.76
Indentation crack length (ICL)	0.55	1.2
Indentation COD overall	0.51	0.56
Indentation COD near tip	0.47	0.49

It is evident that the indentation values are generally lower than those from vacuum DCB tests, consistent with some reduction in effective toughness with post-indentation crack

extension in moist air, as discussed in the previous section. An exception is the ICL value for borosilicate glass, which is considerably larger.

Whereas independent long-crack (DCB) toughness tests indicate that both glasses have essentially similar K_C values, which is also found by the COD approach, the ICL toughness is considerably higher for the borosilicate relative to the soda-lime glass. This difference results from the value of 0.016 used for the coefficient δ in Equation (5.9), which was originally determined by calibration against "normal" materials with independently known toughnesses [81Ans]. In order to achieve for the borosilicate glass a toughness similar to soda-lime, a much smaller coefficient of $\delta \approx 0.006$ would have to be used. This discrepancy is attributable to the different levels of residual contact stresses that drive the radial cracks (see section 7.3.1). The radial crack lengths are consequently smaller in the anomalous material, leading to an overestimate of toughness from ICL measurements. The applicability of the ICL method is limited by the lack of literature values for the coefficient δ of materials with anomalous behaviour.

By comparison, the COD approach is a powerful tool for fracture toughness determination [04Bur], which is applicable to both normal and anomalous types materials, without requiring the knowledge of empirical parameters, albeit at some expense in experimental simplicity.

8. Conclusions

In the present work, Vickers indentation studies were performed, focusing on the crack opening displacement (COD) method as a novel approach for the determination of fracture toughness and residual stress distribution. Two different types of glasses as reference materials as well as fully dense, amorphous SiCN ceramics produced from precursor polymers through a casting route were investigated. Soda lime and borosilicate glass were selected, which are well documented to behave as "normal" and "anomalous" glasses under contact stress, respectively. A set of four different pyrolysis temperatures for polymer derived ceramics differing in pyrolysis temperature (800°C, 900°C, 1000°C, 1100°C), were chosen.

Examination of indentation fracture morphologies in polymer-derived amorphous SiCN ceramics has shown anomalous behaviour evidenced by the shorter crack length and smaller indent size, as well as the formation of well-developed cracks of cone geometry observed beneath the indentation on the fracture surface. It follows that in this material densification due to compaction of an "open" microstructure or free volume occurs under indentation. Taking the cone angle as a measure for anomalous behaviour, it is concluded that the amorphous ceramics behave more anomalous than borosilicate glass, but less than fused silica. Furthermore, when the pyrolysis temperature is increased, the indentation fracture behaviour of the amorphous ceramics is observed to approach that of borosilicate, as apparent from the increase in cone angle.

Measurements of indentation crack opening generally require recourse to high magnification, high accuracy observation techniques like atomic force microscopy (AFM) or high resolution scanning electron microscopy (HRSEM). In total, the AFM technique has proven to be more convenient.

The crack opening profiles also reveal the characteristic differences between normal and anomalous indentation behaviour. The latter goes along with smaller crack opening, as densification under indentation may reduce the contact stress created by indentation, whereby the opening force is reduced. A normalized plot of the crack opening profile was developed, which allows to distinguish amorphous materials with respect to normal vs. anomalous indentation behaviour. A comparison between the polymer derived amorphous SiCN ceramics and the two types of glasses showed that the latter have the smallest normalized opening as

well as the shortest crack length. A comparison among polymer-derived SiCN amorphous ceramics synthesised at different pyrolysis temperatures reveals an increase of the normalized crack opening and length. Hence a tendency towards normal indentation behaviour with rising pyrolysis temperature is deduced.
Measurements of the crack opening over the entire radial crack length enable to determine the nature and intensity of the underlying crack driving forces, i.e. the residual contact stresses. For this purpose, a numerical method based upon the weight function approach was developed, which allowed to derive the residual stress distribution around an indent and the stress intensity factor or fracture toughness. The values obtained for the glasses indicate significantly higher stress intensities in the normal glass relative to the anomalous glass consistent with previous evaluations using polarized light. The maximum residual stress values obtained for the amorphous ceramics are of the same order as those of borosilicate glass. In addition, the amorphous ceramics reveal an increase in maximum residual stress with rising pyrolysis temperature, in accordance with the simultaneous decrease in anomalous behaviour.

The values calculated for the stress intensity factor of soda lime and borosilicate glass, from overall COD data, are in good agreement with those reported in the literature. The stress intensity factors obtained for the ceramics are larger than for the glasses and increase with pyrolysis temperature, with the maximum value reached for SiC-1000.

In order to assess the reliability of the residual stress and stress intensity factor obtained through the numerical procedure developed, a new method has been devised that is based upon the geometrical parameter, which should be constant for different materials. Except for a small deviation from the real angle of the Vickers pyramid indenter, the similarity of the values obtained for the angle or the geometrical parameter demonstrate that the procedure for calculating the residual stress and fracture toughness from overall COD data provides reliable results. Considering the general difficulties in determining the residual stress intensity with high accuracy, the present approach allows an appropriate estimate for this important material parameter.

Moreover, the maximum residual stress and stress intensity factor derived from the overall COD data allows estimation of the residual stress parameter, χ. This parameter is very important for new materials, which often can be produced only with small sample size

insufficient for calibration of this parameter by conventional techniques. With the known χ parameter determined in this manner, it becomes possible to use the indentation crack length approach for estimating the fracture toughness of a wide range of materials.

Fracture toughness can be obtained by fitting a parabolic profile to the measured crack tip COD as a function of the distance from the crack tip. An appropriate universal fitting function, which is able to describe deviations from the ideal shape of the near-tip crack profile, as usually observed in anomalous materials, was derived. The toughness evaluations are similar for the two glasses, within the scatter in data, consistent with the DCB trend. The values for the polymer-derived amorphous SiCN ceramics are higher than those of the soda lime and borosilicate glass, and an increase in pyrolysis temperature leads to an increase in fracture toughness, except for the fact that SiCN-1000 instead of SiCN-1100 lead to the highest value. Consistency between the two approaches (overall COD and near tip COD approach) is observed.

The influence of subcritical crack growth on the crack opening profiles was investigated only in case of the glasses since the polymer derived amorphous SiCN ceramics did not show subcritical crack growth. Measurements of the crack opening over the entire length of radial cracks after different time intervals revealed that the major changes in crack opening occur near the crack tip within 2 days from the introduction of the cracks. Consequently, subcritical crack growth has significant influence on the calculated values of fracture toughness, while the values of residual stress are almost unaffected.

This study demonstrates the greater reliability of the COD technique as a means of intrinsic toughness determination as compared to ICL. On the other hand, the measurements are more onerous, generally requiring recourse to high magnification, high accuracy observation techniques.

The methodology presented in this study should prove useful as a means of characterizing the deformation response of glasses and other brittle materials under contact stress.

Appendix 1

Boussinesq elastic field

Solutions for the stress field in an isotropic, elastic half-space under normal point loading, were first derived in 1885 by J. Boussinesq.

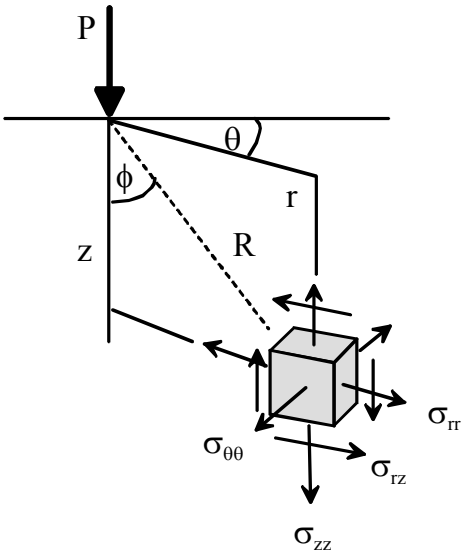

Figure A1. Coordinate system for axially symmetric point loading P

In terms of the cylindrical coordinates of Figure A1 we have the following components;

$$\sigma_{rr} = \frac{P}{\pi R^2}\left(\frac{1-2\nu}{4}\sec^2\left(\frac{\phi}{2}\right) - \frac{3}{2}\cos\phi\sin^2\phi\right) \quad \text{(A1)}$$

$$\sigma_{\theta\theta} = \frac{P}{\pi R^2}\left(\frac{1-2\nu}{2}\right)\left[\cos\phi - \frac{1}{2}\sec^2\left(\frac{\phi}{2}\right)\right] \quad \text{(A2)}$$

$$\sigma_{zz} = -\frac{3P\cos^3\phi}{2\pi R^2} \quad \text{(A3)}$$

$$\sigma_{rz} = -\frac{3P\cos^2\phi\sin\phi}{2\pi R^2} \quad \text{(A4)}$$

$$\sigma_{r\theta} = \sigma_{\theta z} = 0 \quad \text{(A5)}$$

Suitable tensor transformations provide the directions and magnitudes of the principal stress components. Two of the principal normal stresses, σ_{11} and σ_{33} , are contained in the symmetry plane θ = constant, their angles with the specimen surface given by

$$\tan 2\alpha = \frac{2\sigma_{rz}}{\sigma_{zz} - \sigma_{rr}}. \qquad \text{(A6)}$$

The third principal normal stress, σ_{22}, is everywhere perpendicular to the symmetry plane. The principal directions are labelled such that $\sigma_{11}>\sigma_{22}>\sigma_{33}$ generally. Where

$$\sigma_{11} = \sigma_{rr}\sin^2\alpha + \sigma_{zz}\cos^2\alpha - 2\sigma_{rz}\sin\alpha\cos\alpha \qquad \text{(A7)}$$

$$\sigma_{22} = \sigma_{\theta\theta} \qquad \text{(A8)}$$

$$\sigma_{33} = \sigma_{rr}\cos^2\alpha + \sigma_{zz}\sin^2\alpha + 2\sigma_{rz}\sin\alpha\cos\alpha. \qquad \text{(A9)}$$

The principal shear stresses are accordingly given by

$$\sigma_{13} = \frac{1}{2}(\sigma_{11} - \sigma_{33}) \qquad \text{(A10)}$$

$$\sigma_{12} = \frac{1}{2}(\sigma_{11} - \sigma_{22}) \qquad \text{(A11)}$$

$$\sigma_{23} = \frac{1}{2}(\sigma_{22} - \sigma_{33}), \qquad \text{(A12)}$$

inclined at $\pi/4$ to the principal directions. Finally, the magnitude of the component of hydrostatic compression is

$$p = -\frac{1}{3}(\sigma_{11} + \sigma_{22} + \sigma_{33}). \qquad \text{(A13)}$$

Appendix 2

Program for calculation of the residual stress distribution and stress intensity factor from the overall COD data - Mathematica 4.1

```
data = ReadList["cer9003p.txt", {Number, Number}];

          [    ]
ymax = Max[data]
xmin = Infinity
Do[xmin = Min[xmin, data[[i]][[1]]], {i, 1, nindata}]
xmax = -Infinity
Do[xmax = Max[xmax, data[[i]][[1]]], {i, 1, nindata}]

<< NumericalMath`SplineFit`

curvedata = SplineFit[data, Bezier]

n = nindata - 1

res = 1

raw = Table[curvedata[i], {i, 0, n, res}];
Show[ListPlot[data, PlotStyle→ {RGBColor[1, 0, 0],
    PointSize[.015]}], Graphics[{RGBColor[0, 0.25, 0],
   Line[raw]}], PlotRange→ {{xmin, xmax}, {ymin, ymax}}]
```

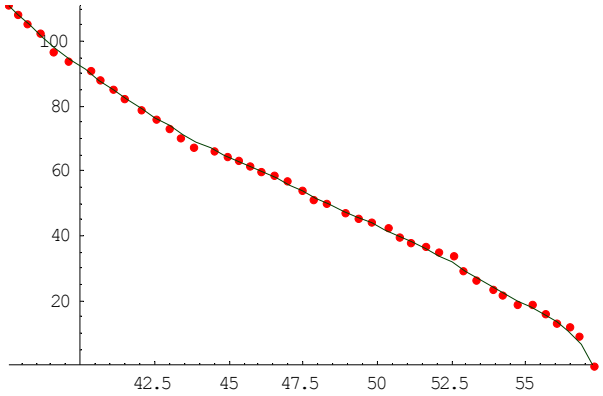


```
ndata = Dimensions[raw][[1]]

nstripes = 25

delta = (xmax - xmin) / nstripes

rip = Table[xmin + i * delta, {i, 0, nstripes}]
```

```
ri = rip / 10^6;

e = 112500

                                                                    }]
```

$$\text{Do}\Big[\text{Print}[i];\ \text{Do}\Big[dm = \text{Max}[\text{meas}[i,1], ri[[j]]];$$

$$g[i,j] = 1/e\ \text{NIntegrate}\Big[\frac{2\,\text{meas}[i,1]\left(\frac{\sqrt{cs^2 - ri[[j]]^2}}{0.5\sqrt{cs\,\pi}} - \frac{\sqrt{cs^2 - \text{Min}[cs, ri[[j+1]]]^2}}{0.5\sqrt{cs\,\pi}}\right)}{\sqrt{\pi\,cs}\ \sqrt{cs^2 - \text{meas}[i,1]^2}},$$

$$\{cs, 1.00000001\,dm, \text{meas}[ndata,1]\}, \text{PrecisionGoal} \to 8\Big];$$

$$\text{Print}[g[i,j]], \{j,1,nstripes\}\Big], \{i,1,ndata-1\}\Big]$$

$$\text{matrix} = \text{Table}\Big[10^{17}\sum_{i=1}^{ndata-1} g[i,j]\,g[i,k], \{j,nstripes\}, \{k,nstripes\}\Big];$$

$$\text{vector} = \text{Table}\Big[10^{17}\sum_{i=1}^{ndata-1} \text{meas}[i,2]\,g[i,j], \{j,nstripes\}\Big]$$

```
sigma = LinearSolve[matrix, vector]
```

$$\text{Do}\Big[p = N\Big[\frac{10\text{^}6}{2*xmin}\ (ri[[i]] + ri[[i+1]])\Big] >>> \text{"nradcord.txt"};$$

```
 sigma[[i]] >>> "resstres.txt", {i, nstripes}]
```

$$\text{Solve}\Big[kic == \frac{2}{\sqrt{3.14 * \text{meas}[ndata,1]}}$$

$$\sum_{i=1}^{nstripes} \text{sigma}[[i]] * \Big(\sqrt{(\text{meas}[ndata,1]*1.01)\text{^}2 - (\text{ri}[[i]])\text{^}2} -$$

$$\sqrt{(\text{meas}[ndata,1]*1.01)\text{^}2 - (\text{ri}[[i+1]])\text{^}2}\Big), kic\Big]$$

```
{{kic → 0.740223}}
```

$$\text{stressdis} = \text{Table}\Big[\Big\{N\Big[\frac{10\text{^}6}{2*xmin}\ (ri[[i]] + ri[[i+1]])\Big], \text{sigma}[[i]]\Big\},$$

$$\{i,1,nstripes\}\Big];\ \text{Print}[\text{ Residual stress }];$$

```
ListPlot[stressdis, PlotStyle → {RGBColor[0, 0.2, 0],
   PointSize[.025]}, PlotRange → All]
```

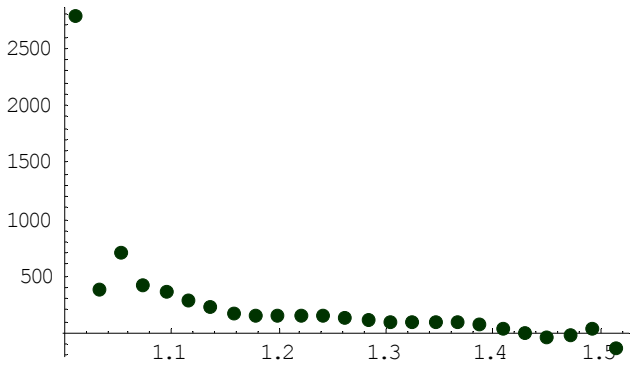

- Graphics -

```
<< Statistics`NonlinearFit`
stressdata = stressdis
nindatastress = Dimensions[stressdata][[1]]
yminstress = Min[stressdata]
ymaxstress = Max[stressdata]
xminstress = Infinity
Do[xminstress = Min[xminstress, stressdata[[i]][[1]]], {i, 1, nindatastress}]
xmaxstress = -Infinity
Do[xmaxstress = Max[xmaxstress, stressdata[[i]][[1]]], {i, 1, nindatastress}]

resstressfit = NonlinearFit[stressdata, u1 * (1 / x)^3, {x}, {u1}];
BestFitParameters /. NonlinearRegress[stressdata, theta1 * (1 / x)^3, {x},
  {theta1}, RegressionReport → BestFitParameters]
{theta1 → 644.26}
Show[ ListPlot[stressdata, PlotStyle → {RGBColor[1, 0, 0], PointSize[.025]}],
  Plot[resstressfit, {x, xminstress, xmaxstress}], PlotRange → All];
```

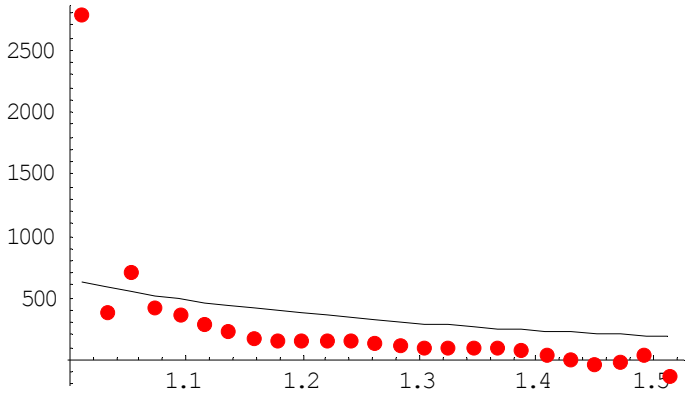

Appendix 3

Program for fracture toughness estimation from the near tip COD data - Mathematica 4.1

```
ktipdata = ReadList["cer11004Ptip.txt", {Number, Number}];
nindataktip = Dimensions[ktipdata][[1]]
yminktip = Min[ktipdata]
ymaxktip = Max[ktipdata]
xminktip = Infinity
Do[xminktip = Min[xminktip, ktipdata[[i]][[1]]],
 {i, 1, nindataktip}]
xmaxktip = -Infinity
Do[xmaxktip = Max[xmaxktip, ktipdata[[i]][[1]]],
 {i, 1, nindataktip}]
<< Statistics`NonlinearFit`
zak = theta1 * Sqrt[8/π] x^0.5 + theta2 x^(3/2);
zakcomb = theta1 * Sqrt[8/π] x^0.5 + theta2 x^(3/2) + theta3 x^(5/2);
rodsei = theta1 * Sqrt[8/π] * x^0.5 + theta2 x^(5/2);
zakfit = NonlinearFit[ktipdata, zak, {x}, {theta1, theta2}]
Print[Zakfit]
Show[ ListPlot[ktipdata,
   PlotStyle→ {RGBColor[1, 0, 0], PointSize[.015]}],
  Plot[zakfit, {x, xminktip, xmaxktip}],
  PlotRange→ {{xminktip, xmaxktip},
    {yminktip, ymaxktip}}];
```

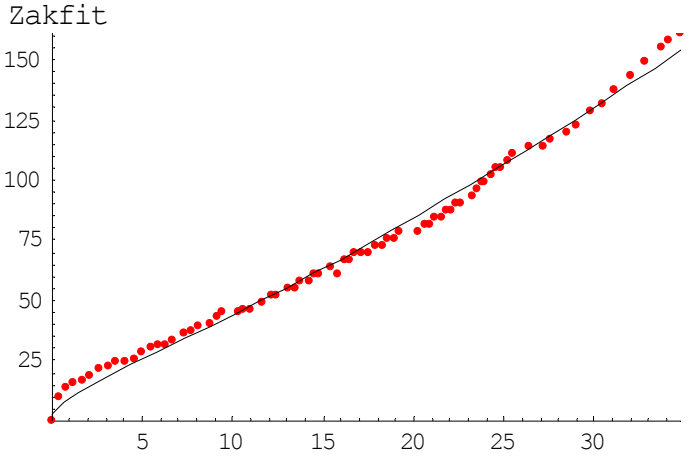

```
zakcombfit = NonlinearFit[ktipdata, zakcomb, {x},
  {theta1, theta2, theta3}]
Print[ Zakcombfit ]
Show[ ListPlot[ktipdata,
   PlotStyle→ {RGBColor[1, 0, 0], PointSize[.015]}],
  Plot[zakcombfit, {x, xminktip, xmaxktip}],
  PlotRange→ {{xminktip, xmaxktip},
    {yminktip, ymaxktip}}];
```

Zakcombfit

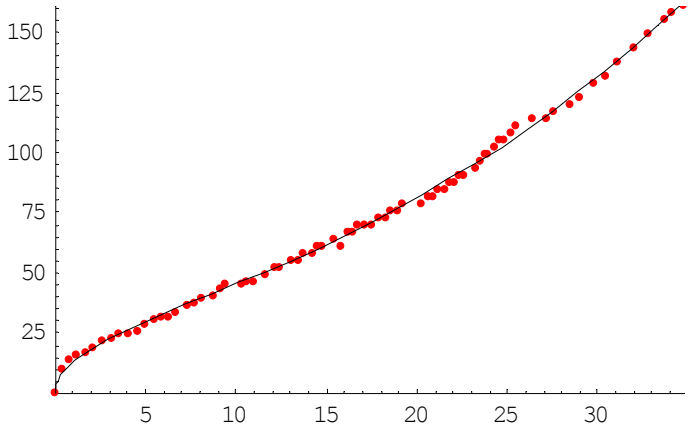


```
rodseifit = NonlinearFit[ktipdata, rodsei, {x},
  {theta1, theta2}]
Print[ Rodseifit ]
Show[ ListPlot[ktipdata,
   PlotStyle→ {RGBColor[1, 0, 0], PointSize[.015]}],
  Plot[rodseifit, {x, xminktip, xmaxktip}],
  PlotRange→ {{xminktip, xmaxktip},
    {yminktip, ymaxktip}}];
```

Rodseifit

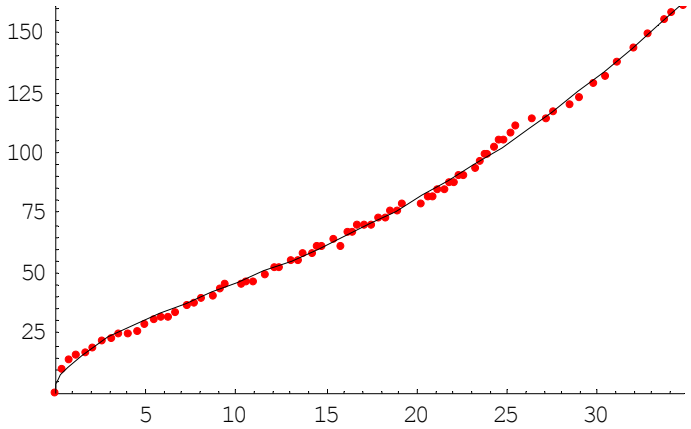

```
BestFitParameters /.
 NonlinearRegress[ktipdata, zak, {x}, {theta1, theta2},
  RegressionReport → BestFitParameters]
NonlinearRegress[ktipdata, zak, {x}, {theta1, theta2},
 RegressionReport → ParameterCITable]
NonlinearRegress[ktipdata, zak, {x}, {theta1, theta2},
 RegressionReport → EstimatedVariance]
```

```
                                Estimate      Asymptotic SE      CI
{ParameterCITable → theta1      5.60332       0.183595           {5.23758, 5.96907}   }
                    theta2      0.493784      0.0125795          {0.468724, 0.518843}
{EstimatedVariance → 12.3177}
```

```
BestFitParameters /.
 NonlinearRegress[ktipdata, zakcomb, {x},
  {theta1, theta2, theta3},
  RegressionReport → BestFitParameters]
NonlinearRegress[ktipdata, zakcomb, {x},
 {theta1, theta2, theta3},
 RegressionReport → ParameterCITable]
NonlinearRegress[ktipdata, zakcomb, {x},
 {theta1, theta2, theta3},
 RegressionReport → EstimatedVariance]
```

```
                                Estimate      Asymptotic SE      CI
{ParameterCITable → theta1      7.99356       0.172015           {7.65081, 8.33631}      }
                    theta2      0.0591884     0.0276265          {0.00414142, 0.114235}
                    theta3      0.010542      0.000654331        {0.00923823, 0.0118458}
{EstimatedVariance → 2.76952}
```

```
BestFitParameters /.
 NonlinearRegress[ktipdata, rodsei, {x},
  {theta1, theta2},
  RegressionReport → BestFitParameters]
NonlinearRegress[ktipdata, rodsei, {x}, {theta1, theta2},
 RegressionReport → ParameterCITable]
NonlinearRegress[ktipdata, rodsei, {x}, {theta1, theta2},
 RegressionReport → EstimatedVariance]
```

```
                                Estimate      Asymptotic SE      CI
{ParameterCITable → theta1      8.34184       0.057569           {8.22716, 8.45652}     }
                    theta2      0.0119108     0.00014462         {0.0116227, 0.0121989}
{EstimatedVariance → 2.90209}
```

References

[51Tab] D. Tabor, *The hardness of metals* (Clarendon, Oxford, 1951)

[57Pal] S. Palmqvist, *Jenkontorets Ann.* **141**, 300-307 (1957)

[64Mar] D. M. Marsh, *Proceedings of the Royal Society of London Series a-Mathematical and Physical Sciences* **282**, 33-& (1964)

[67Wie] S. M. Wiederhorn, *American Ceramic Society Bulletin* **46**, 393-& (1967)

[70Tim] S. P. Timoshenko, J. N. Goodier, *Theory of elasticity* (McGraw-Hill, New York, 1970)

[72Wie] S. M. Wiederhorn, *J. Am. Ceram. Soc.* **55**, 81-& (1972)

[75Law] B. R. Lawn, M. V. Swain, *J. Mater. Sci.* **10**, 113-122 (1975)

[75Lawa] B. R. Lawn, D. B. Marshall, P. Chantikul, *J. Mat. Sci.* **16**, 1769-1775 (1981).

[75Lawb] B. R. Lawn, E. R. Fuller, *J. Mater. Sci.* **10**, 2016-2024 (1975)

[75Lawc] B. R. Lawn, M. V. Swain, K. Phillips, *J. Mater. Sci. Lett.* **10**, 1236-1239 (1975)

[76Law] B. R. Lawn, T. Jensen, A. Arora, *J. Mater. Sci.* **11**, 573-575 (1976)

[76Swaa] M. V. Swain, J. T. Hagan, *J. of Physics D-Applied Physics* **9**, 2201-& (1976)

[76Evaa] A. G. Evans, T. R. Wilshaw, *Acta Mat.* **24**, 939-956 (1976)

[76Swa] M. V. Swain, *J. Mater. Sci.* **11**, 2345-2348 (1976)

[76Phi] K. Phillips, *J. Mater. Sci.* **11**, 2354-2356 (1976)

[77Swa] M. V. Swain, J. T. Hagan, J. E. Field, *J. Mater. Sci.* **12**, 1914-1917 (1977)

[77Wie] S. M. Wiederhorn, B. R. Lawn, *J. Am. Ceram. Soc.* **60**, 451-458 (1977)

[77Eva] A. G. Evans, T. R. Wilshaw, *J. Mater. Sci.* **12**, 97-116 (1977)

[77Law] B. R. Lawn, A. G. Evans, *J. Mater. Sci.* **12**, 2195-2199 (1977)

[78Hag] J. T. Hagan, M. V. Swain, *J. of Physics D-Applied Physics* **11**, 2091-& (1978)

[79Haga] J. T. Hagan, *J. Mater. Sci.* **14**, 2975-2980 (1979)

[79Swa] M. V. Swain, *J. Am. Ceram. Soc.* **62**, 318-319

[79Mar] D. B. Marshall, B. R. Lawn, *J. Mater. Sci.* **14**, 2001-2012 (1979)

[79Mara] D. M. Marsh, *Proc. of the Royal Society of London Series A- Mathematical and Physical Sciences* **279**, 420-& (1964) (1979)

[79Lan] J. Lankford, D. L. Davidson, *J. Mater. Sci.* **14**, 1669-1675 (1979)

[79Lana] J. Lankford, D. L. Davidson, *J. Mater. Sci.* **14**, 1662-1668 (1979)

[79Aro] A. Arora, D. B. Marshall, B. R. Lawn, *J. of Non-Cryst. Sol.* **31**, 415-428 (1979)

[80Hag] J. T. Hagan, *J. Mater. Sci.* **15**, 1417-1424 (1980)

[80Law] B. R. Lawn, A. G. Evans, D. B. Marshall, *J. Am. Ceram. Soc.* **63**, 574-581 1980)

[81Ans] G. R. Anstis, P. Chantikul, B. R. Lawn, D. B. Marshall, *J. Am. Ceram. Soc.* **64**, 533-538 (1981)

[81Lan] J. Lankford, *J. Mater. Sci.* **16**, 1177-1182 (1981)

[81Lawa] B. R. Lawn, D. B. Marshall, P. Chantikul, *J. Mater. Sci.* **16**, 1769-1775 (1981)

[81Lawb] B. R. Lawn, D. B. Marshall, G. R. Anstis, T. P. Dabbs, *J. Mater. Sci.* **16**, 2846-2854 (1981)

[81Gup] P. K. Gupta, N. J. Jubb, *J. Am. Ceram. Soc.* **64**, C112-C114 (1981)

[81Cha] P. Chantikul, G. R. Anstis, B. R. Lawn, D. B. Marshall, *J. Am. Ceram. Soc.* **64**, 539-543 (1981)

[81Wie] S. M. Wiederhorn, *American Ceramic Society Bulletin* **60**, 851-851 (1981)

[82Mic] T. A. Michalske , S. W. Freiman, *Nature*, 511-512 (1982)

[82Mar] D. B. Marshall, B. R. Lawn, A. G. Evans, *J. Am. Ceram. Soc.* **65**, 561-566 (1982)

[82Ish] H. Ishikawa, N. Shinkai, *J. Am. Ceram. Soc.* **65**, C124-C127 (1982)

[82Chi] S. S. Chiang, D. B. Marshall, A. G. Evans, *J. of Appl. Phys.* **53**, 298-311 (1982)

[82Chia] S. S. Chiang, D. B. Marshall, A. G. Evans, *J. of Appl. Phys.* **53**, 312-317 (1982)

[82Nii] K. Niihara, R. Morena, D. P. H. Hasselman, *J. Mater. Sci. Lett.* **1**, 13-16 (1982)

[82Lan] J. Lankford, *J. Mater. Sci. Lett.* **1**, 493-495 (1982)

[83Nii] K. Niihara, *J. Mater. Sci. Lett.* **2**, 221-223 (1983)

[83Mar] D. B. Marshall, *J. Am. Ceram. Soc.* **66**, 127-131 (1983)

[83Coo] R. F. Cook, B. R. Lawn, *J. Am. Ceram. Soc.* c200-c201 (1983)

[85She] D. K. Shetty, A. R. Rosenfield, W. H. Duckworth, *J. Am. Ceram. Soc.* **68**, C282-C284 (1985)

[85Law] B. R. Lawn, K. Jakus, A. C. Gonzalez, *J. Am. Ceram. Soc.* **68**, 25-34 (1985)

[85She] D. K. Shetty, A. R. Rosenfield, W. H. Duckworth, *J. Am. Ceram. Soc.* **68**, C282-C284 (1985)

[85Lau] M. T. Laugier, *J. Mat. Sci. Lett.* **4**, 1539-1541 (1985)

[86Cha] M. M. Chaudhri, C. R. Kurkjian, *J. Am. Ceram. Soc.* **69**, 404-410 (1986)

[87Tan] K. Tanaka, *J. Mater. Sci.* **22**, 1501-1508 (1987)

[87Law] B. R. Lawn, D. H. Roach, R. M. Thomson, *J. Mater. Sci.* **22**, 4036 (1987)

[87Ost] P. Ostojic, R. McPherson, *Int. Journal of Fracture* **33**, 297-312 (1987)

[87Jon] S. L. Jones, C. J. Norman, R. Shahani, *J. Mater. Sci. Lett.* **6**, 721-723 (1987)

[89Pon] C. B. Ponton, R. D. Rawlings, *Mat. Sci. and Tech.* **5**, 865-961 (1989)

[89Han] W. T. Han, P. Hrma, A. R. Cooper, *Physics and Chemistry of Glasses* **30**, 30-33 (1989)

[89Li] Z. Li, A. Ghosh, A. S. Kabayashi, R. C. Bradt, *J. Am. Ceram. Soc.* **72**, 904-911 (1989)

[90Röd]] J. Rödel, J. F. Kelly, B. R. Lawn, *J. Am. Ceram. Soc.* **73**, 3313-3318 (1990)

[90Coo] R. F. Cook, G. M. Pharr, *J. Am. Ceram. Soc.* **73**, 787-817 (1990)

[90Geh] E. Gehrke, C. Ullner, M. Hahnert, *Glastechnische Berichte-Glass Science and Technology* **63**, 255-265 (1990)

[90Lia] K. M. Liang, G. Orange, G. Fantozzi, *J. Mater. Sci.* **25**, 207-214 (1990)

[91Lat] S. Lathabai, J. Rodel, T. Dabbs, B. R. Lawn, *J. Mater. Sci.* **26**, 2157-2168 (1991)

[91Lata] S. Lathabai, J. Rodel, T. Dabbs, B. R. Lawn, *J. Mater. Sci.* **26**, 2313-2321 (1991)

[91Röd] J. Rödel, E. R. Fuller, B. R. Lawn, *J. Am. Ceram. Soc.* **74**, 3154-3157 (1991)

[91Fet] T. Fett, K. Germerdonk, A. Grossmuller, K. Keller, D. Munz, *J. Mater. Sci.* **26**, 253-257 (1991)

[92Smi] S. M. Smith, R. O. Scattergood, *J. Am. Ceram. Soc.* **75**, 305-315 (1992)

[92Smia] S. M. Smith, R. O. Scattergood, *J. Am. Ceram. Soc.* **75**, 2593-2596 (1992)

[92Bra] L. M. Braun, S. J. Bennison, B. R. Lawn, *J. Am. Ceram. Soc.* **75**, 3049-3057 (1992)

[93Coo] R. F. Cook, E. G. Liniger, *J. Am. Ceram. Soc.* **76**, 1096-1105 (1993)

[93Sak] M. Sakai, R. C. Bradt, *International Materials Reviews* **38**, 53-78 (1993)

[93Law] B. R. Lawn, *Fracture of Brittle Solids* (Cambridge University Press, Cambridge, ed. Second Edition, 1993

[94zen] K. Y. Zeng, D. Rowcliffe, *J. Am. Ceram. Soc.* **77**, 524-530 (1994)

[95Zen] K. Zeng, D. J. Rowcliffe, *Acta Metallurgica Et Materialia* **43**, 1935-1943 (1995)

[95Sgl] V. M. Sglavo, D. J. Green, *J. Am. Ceram. Soc.* **78**, 650-656 (1995)

[95Sgla] V. M. Sglavo, D. J. Green, *Acta Met. Mat.* **43**, 965-972 (1995)

[95Kur] C. R. Kurkjian, G. W. Kammlott, M. M. Chaudhri, *J. Am. Ceram. Soc.* **78**, 737-744 (1995)

[96Sgl] V. M. Sglavo, D. J. Green, *Engineering Fracture Mechanics* **55**, 35-46 (1996)

[97Bar] M.W.Barsoum, *Fundamental of ceramics* (McGraw-Hill,Singapore,1997)

[97Qui] J. B. Quinn, G. D. Quinn, *J. Mater. Sci.* **32**, 4331-4346 (1997)

[97Sei] J. Seidel, J. Rödel, *J. Am. Ceram. Soc.* **80**, 433-438 (1997)

[98Hil] R. Hill, *The Mathematical Theory of Plasticity* (Clarendon Press, Oxford, 1998)

[98Gre] D. J. Green, *An introduction to the mechanical properties of ceramics* (Cambridge University Press, Cambridge, 1998)

[98Cra] D. C. Cranmer, D. W. Richerson, *Mechanical testing for ceramic design and reliability* (Marcell Dekker, New York, 1998)

[98Nis] T. Nishimura, R.Haug, J.Bill,G.Thurn, F.Aldinger, *J. Mater. Sci.***33**, 5237-5247 (1998)

[99Ray] K. K. Ray, A. K. Dutta, *British Ceramic Transactions* **98**, 165-171 (1999)

[99Gona] J. D. Gong, *Journal of the European Ceramic Society* **19**, 1585-1592 (1999)

[99Gre] D. J. Green, P. J. Dwivedi, V. M. Sglavo, *British Ceramic Transactions* **98**, 291-295 (1999)

[99Sgl] V. M. Sglavo, D. J. Green, *J. Am. Ceram. Soc.* **82**, 1269-1274 (1999)

[99Sglb] V. M. Sglavo, D. J. Green, *J. Mater. Sci.* **34**, 579-585 (1999)

[00Zie] E. C. Ziemath, P. S. P. Herrmann, *J. of Non-Cryst. Sol.* **273**, 19-24 (2000)

[01Bau] A. Bauer, M. Christ, A. Zimmermann, F. Aldinger, *J. Am. Ceram. Soc.* **84**, 2203-2207 (2001)

[01Sgl] V. M. Sglavo, D. J. Green, *J.of the European Ceramic Society* **21**, 561-567 (2001)

[01Whi] B. R. Whittle, R. J. Hand, *J. Am. Ceram. Soc.* **84**, 2361-2365 (2001)

[01Koc] C. Kocer, R. E. Collins, *J. Am. Ceram. Soc.* **84**, 2585-2593 (2001)

[01Gon] J. H. Gong, W. J. Si, Z. D. Guan, *J. of Non-Cryst. Sol.* **282**, 325-328 (2001)

[02Ber] M. Bertoldi, V. M. Sglavo, *J. Am. Ceram. Soc.* **85**, 2499-2506 (2002)

[02Bau] A. Bauer, PhD thesis, Stuttgart (2002)

[03Tan] F. Tancret, F. Osterstock, *Philosophical Magazine* **83**, 125-136 (2003)

[03Zhe] X. J. Zheng, Z. Y. Yang, Y. C. Zhou, *Scripta Materialia* **49**, 71-76 (2003)

[03Res] N. Resta, PhD thesis, in preparation

[03Jan] N.Janakiraman, PhD thesis, in preparation

[04Bur] Z. Burghard, A. Zimmermann, F. Aldinger, J.Rödel, B.R.Lawn, Acta Mat. (in press)

Curriculum vitae

Personal information:

Name: Zaklina Burghard born Gnjidic

Date of birth:3. September 1968

Place of birth: Vrsac, Yugoslavia

Nationality: Serbian

Material status: Married, one child

Education:

1975-1983 Primary School, Alibunar, Yugoslavia

1983-1987 High School, Belgrade, Yugoslavia

1987-1995 Graduate study at the Department of Chemical and Biochemical Engineering, Faculty of Technology and Metallurgy, University of Belgrade, Yugoslavia

Graduate engineer of technology degree obtained in January 1995.

1995-1999 Postgraduate study at the Department of Materials Science, Faculty of Technology and Metallurgy, University of Belgrade, Yugoslavia

Master of Science degree obtained in October 1999.

Master thesis: The influence of SiC particles on the microstructure and mechanical properties of metal matrix composites

2001- Ph.D. work at the Max-Planck Institute for Metals Research and University of Stuttgart (Germany), with support from the Deutsche Forschungsgemeinschaft (DFG) scholarship under Graduiertenkolleg 285.

Ph. D thesis: Behavior of glasses and polymer derived amorphous ceramics under contact stress

Work experience:

1996-2000 Research assistant - Vinca Institute of Nuclear Sciences, Material Science Laboratory, Group Powder Metallurgy, Belgrade, Yugoslavia

Synthesis and investigation of the mechanical and physical properties of composite materials made of an aluminium alloy matrix reinforced with SiC particles by powder metallurgy techniques. Work under a research project of the Ministry for Science and Technology of Serbia with the title “Researches in the field of high strength and composite materials obtained by powder metallurgy techniques”